12-2010

The Interaction of rock and water during shock decompression: A hybrid model for fluidized ejecta formation

Audrey Hughes Rager
University of Nevada, Las Vegas

THE INTERACTION OF ROCK AND WATER DURING SHOCK DECOMPRESSION: A HYBRID MODEL FOR FLUIDIZED EJECTA FORMATION

by

Audrey Hughes Rager

Bachelor of Arts
University of Colorado
1989

Master of Science
Emporia State University
2003

A dissertation submitted in partial fulfillment of
the requirements for the

Doctor of Philosophy Degree in Geoscience
Department of Geoscience
College of Science

Graduate College
University of Nevada, Las Vegas
December 2010

THE GRADUATE COLLEGE

We recommend the dissertation prepared under our supervision by

Audrey Hughes Rager

entitled

The Interaction of Rock and Water during Shock Decompression: A Hybrid Model for Fluidized Ejecta Formation

be accepted in partial fulfillment of the requirements for the degree of

Doctor of Philosophy in Geoscience

Eugene Smith, Committee Chair

Elisabeth Hausrath, Committee Member

Rosaly Lopes, Committee Member

Adam Simon, Committee Member

Stephen Lepp, Graduate Faculty Representative

Ronald Smith, Ph. D., Vice President for Research and Graduate Studies
and Dean of the Graduate College

December 2010

ABSTRACT

**The Interaction of Rock and Water during Shock Decompression:
A Hybrid Model for Fluidized Ejecta Formation**

by

Audrey Hughes Rager

Dr. Eugene Smith, Examination Committee Chair
Professor of Geology
University of Nevada Las Vegas

Crater and ejecta morphology provide insight into the composition and structure of the target material. Martian rampart craters, with their unusual single-layered (SLE), double-layered (DLE), and multi-layered ejecta (MLE), are the subject of particular interest among planetary geologists because these morphologies are thought to result from the presence of water in the target. Also of interest are radial lines extending from the crater rim to the distal rampart of DLE craters. Exactly how these layered ejecta morphologies and radial lines form is not known, but they are generally thought to result from interaction of the ejecta with the atmosphere, subsurface volatiles, or some combination of both.

Using the shock tube at the University of Munich, this dissertation tests the hypothesis that the decompression of a rock-water mixture across the vaporization curve for water during the excavation stage of impact cratering results in an increased proportion of fines in the ejecta. This increase in fine material causes the ejecta to flow with little or no liquid water. Also tested are the effects of water on rock fragmentation during shock decompression when the vaporization curve for water is not crossed.

Using results from these experiments, a hybrid model is proposed for the formation of fluidized ejecta and suggests that the existing atmospheric and subsurface

volatile models are end members of a mechanism resulting in ejecta fluidization. Fluidized ejecta can be emplaced through interaction with an atmosphere (atmospheric model) or through addition of liquid water into the ejecta through shock melting of subsurface ice (subsurface volatile model). This dissertation proposes that these models are end members that explain the formation of fluidized ejecta on Mars.

When the vaporization curve for water is crossed, the expanding water vapor increases the fragmentation of the ejecta as measured by a significant reduction in the median grain size of ejecta. Reducing the average particle size in the ejecta curtain reduces the height above the ground at which the advancing curtain becomes permeable to the atmosphere it is compressing. This allows a vortex ring to form behind the curtain and deposit fine ejecta in a fluidized fashion. When the vaporization curve for water is not crossed, water within open pore space increases the fragmentation threshold of rocks, shifting the median grain size to larger sizes. If the amount of water within open pore space is sufficiently large and the vaporization curve is not crossed, the ejecta may contain very large blocks. In the model proposed in this dissertation, the inner layer of DLE forms when there are very large blocks at the base of the ejecta curtain and much finer particles toward the top. In this situation, the larger blocks fall out first and produce the inner ejecta layer. A ring vortex is still formed where the ejecta curtain becomes permeable to the atmosphere. This vortex deposits finer grained material behind the advancing ballistic ejecta and deposits the outer layer. At discrete locations within the ejecta curtain, some of the larger blocks extend outside the average curtain width. At these points Raleigh-Taylor or Kelvin-Helmholtz instabilities (Chandrasekhar, 1981;

Boyce et al., 2010) form, punching holes in the curtain and forming scouring jets below the ring vortex. These jets carve out the radial lines in the inner and outer ejecta blanket.

ACKNOWLEDGEMENTS

Completing a Ph.D. in Geology is an enormous undertaking for anyone. It's especially hard to do while working and raising a young child. I could not possibly have done it without the support I've received from so many wonderful people.

I'd like to thank all of my committee members for their support and input. Most of all I'd like to thank my advisor, Dr. Eugene Smith. Thank you for your enthusiasm for geology and scientific inquiry; for your dedication to all of your students, for your financial and emotional support, for sticking up for me, for encouraging me to work on a topic I was passionate about, for your sense of humor, and for peanut butter cookies.

Thank you to Dr. Adam Simon. When I was close to quitting, your enthusiasm for my project kept me going. Thank you, Dr. Simon, for bringing Dr. Don Dingwell to speak in our department. If I'd never met Dr. Dingwell, this research never would have been completed.

Thank you to Dr. Rosaly Lopes (Jet Propulsion Laboratory) for taking time out of her very busy schedule to be on my committee and for being such a fantastic role model. Thank you to Dr. Elisabeth Hausrath for her expertise and for joining my committee when I needed her most. Thanks to Dr. Stephen Lepp for his time and for bringing an astronomer's perspective to my work.

This dissertation never would have been written if it weren't for Dr. Don Dingwell and Dr. Bettina Scheu from the University of Munich (LMU). Thank you for your interest in my ideas and your willingness to open your lab to me. I hope our experiments will be the start of a new method of research into impact cratering. I'd also like to thank Dr. Uli Küppers (LMU) for assisting me with analysis of fine particles and

for letting me use his desk while he was in the field. Thanks to all the staff and faculty at LMU who made me feel very welcome during my stays in Munich.

Thank you to the NASA Nevada Space Grant Consortium for awarding me the Nevada Space Grant Fellowship for six semesters. Thank you to the UNLV Graduate and Professional Student Association for awarding me research grants. Thank you to the Bernarda E. French, Barton Family, and Desert Space Grant for providing me with scholarships. The research would not have been possible without your funding.

Thank you to Dr. Nadine Barlow (Northern Arizona University) and Dr. Sarah Stewart (Harvard University) for their input and reviews of portions of this dissertation.

I'd like to thank fellow graduate students Racheal Johnsen, Dr. Colin Robins, and Amanda Williams for listening to me and giving me encouragement when I really needed it. You are more than just good scientists; you are all really good people.

Thanks to the amazing undergraduate students at UNLV who made teaching so much fun. You are too numerous to name here, but I'll do it anyway: Lora Griffin, Valerie Tu, Rhonda Roe Wicker, Erin Orozco, Tiesa Dunlop, Lindsey Clark, Thomas Andolfsson, Eli Dreschel, Jason Norgan, Hunter Campbell, Aaron Acena, Thomas Adams, Andrew Miller, Brita Purvis, Christina Urmanski, Katie Zollars, Stephen Paplinski, Chris Kopietz, Jaclyn Carrington, Judy Costa, Eden Espino, Pasquale DelVecchio, Jonathan Carter, Carl Swenberg, Seth Page, Brittany Ruiter, Shereena Dyer, Craig McNeil, Tyler Birthisel, Heather Proa, Brittany Ruiter, and Jackie Blair. Congratulations to those of you who have graduated and gone on to jobs and Graduate School. I know you'll do well.

Thank you to the hard-working office staff (Maria Figueroa, Liz Smith, and Kathryn Birgy) and student workers (Rainne Tiske and Joy Valdivia) for all your help with administrative matters. Thank you Nicolle Booker (Graduate Coordinator, College of Sciences) for helping me navigate the labyrinth of paper work to graduate.

Thank you to Dr. Sean Mulcahy for assisting me with SEM analysis of my samples. Even though the SEM results were not fruitful, I learned a lot and I appreciate you taking time to help me. Thank you to Rebecca Huntoon for helping me with computer, printer, and GIS problems. Thank you to Dr. Helen Neill (UNLV), for being understanding and supportive and letting me take time off to finish my dissertation.

Thank you to my Master's advisor, Dr. James Aber (Emporia State University) for believing in me and teaching me the independence and discipline I needed to complete my Ph.D.

Thank you to Tibor Balint (Jet Propulsion Laboratory) for being such an inspirational mentor at the 2005 NASA/JPL Planetary Sciences Summer School (PSSS). And thanks to my fellow PSSS participants: Jennifer Anderson, Christina Calvin, Timothy Cassidy, Daniel Chavez-Clemente, Brook Corbett, , Heidi Hammerstein, Thomas Hanley, Alice Letcher, Eileen McGowan, Dianna McMenamin, Nathaniel Murphy, Michael Obland, Jeff Parker, Taylor Perron, Noah Petro, Marc Pulupa, Delia Santiago , Robyn Schofield, and Hanna Sizemore. Our week together changed my life and inspired me to pursue a career in planetary geology.

Thank you to Dr. Elizabeth Steininger Wolf for being a true friend. Thank you to my cousin, Cathy Patton, and my aunt, Helene Shay, for emotional support and advice on

you-know-what. Thank you to my cousin, Robert Cook, for his interest in my research and for long conversations and e-mails about phase equilibria.

It takes a village to raise a child. Thank you to all my son's day care providers, teachers, Sunday school teachers, sports instructors, physicians, and support specialists: Edith Brooks, Mike Speck, Christy Wheeler Buckingham, Jeani Crist-Vidal, Eve Jeanos, Kiyo Frazier, James Cunningham, Angel Amboy, Jessica Campbell, Connie Dula, Dr. Julie Beasley, Dr. Johanna Fricke, Dr. Paul Smith, Dr. Ralph Conti, Dr. Mary Grant, Sue Huff, Chris Holcomb, Mona Agamez, Danielle Bell, Danette Barber, Gerri Horka, Ariel Sublett, Derick Egan, Nicki Allison, Raul Baugh, Steven Baugh, and Sydney Baugh.

Thank you to my parents, Tom and Ellen Hughes, for all your love and support throughout the years. I love you very much.

Thank you to my wonderful son, Ian. Ever since you were born you've been an amazing person. You are the one who inspired me to follow my dreams and start the Ph.D. program at UNLV. You are the most wonderful person I have ever met. I hope you will always follow your dreams. Be happy.

Above all, I'd like to thank the one person who stood by me day after day, who shared in my triumphs, propped me up during hard times, kicked me in the butt when I needed it, and always believed in me: my husband, Hal Rager. You are my source of strength. I love you. Now, let's move on to our next adventure.

TABLE OF CONTENTS

LIST OF FIGURES

CHAPTER TWO

CHAPTER THREE

LIST OF TABLES

CHAPTER TWO

CHAPTER THREE

CHAPTER ONE

DISSERTATION OVERVIEW

Fundamental Dissertation Objectives

Layered fluidized ejecta blankets on Mars are unique among terrestrial bodies of the Solar System. Models for the formation of fluidized ejecta on Mars fall into two categories: the subsurface volatile model and the atmospheric model. The relative role of subsurface volatiles versus the atmosphere in the formation of layered ejecta blankets is one of the major questions remaining concerning the geology of Mars.

Rapid decompression during the excavation state of impact cratering may result in water or ice crossing the vaporization curve explosively. This dissertation tests the hypothesis that this explosive vaporization of water increases the degree of fragmentation of ejecta and adds finer materials to the ejecta curtain. These smaller particles interact with the atmosphere to produce a vortex ring behind the advancing ejecta curtain, resulting in the fluidized emplacement of the ejecta. For background information on the impact cratering process, the reader is referred to Appendix 1. Appendix 2 describes Martian rampart crater morphologies, a summary of current models of fluidized ejecta formation, and descriptions of previous studies relevant to the research presented in this dissertation.

The Application of Novel Experimental Techniques

To Established Problems

Most studies on impact cratering and fluidized ejecta emplacement rely on hypervelocity impact experiments and numerical modeling of material response to

hypervelocity impacts. This research takes a unique approach of measuring the effects of water vaporization on rock fragmentation during decompression associated with the excavation stage of impact cratering. This hypothesis was tested using the shock tube apparatus at the University of Munich typically used for research on volcanic rocks and processes (Alidibirov and Dingwell, 1996a, 1996b; Küppers et al., 2006). This is the first study to look at the effects of water vaporization through rapid decompression on rock fragmentation.

Summary of Salient Results

Results of studies undertaken for this dissertation using a volcaniclastic sandstone from the Eldorado Mountains, Nevada indicate that the vaporization of water during rapid decompression alters the grain size distribution of ejecta. For a volcaniclastic sandstone with ~28% open porosity, the average grain size is significantly reduced. When the open pore space is filled to capacity with water, grain shape and grain size distribution are altered. The grain size distribution becomes more bimodal (increased amounts of fines and larger particles).

When the vaporization curve for water is not crossed during rapid decompression, water within pore spaces can increase the fragmentation threshold of rocks by decreasing the amount of open pore space. Ejection angle is inversely proportional to target strength. Therefore, this increased strength may result in lower initial ejection angle and affect the structure of the ejecta curtain.

These results are used to propose a hybrid model for fluidized ejecta formation that accounts for the single-, double-, and multi-layered ejecta found on Mars. The model

also suggests an explanation for the similarities and differences between double-layered ejecta on Mars and Ganymede.

Submission of Individual Chapters as Manuscripts for Publication

Chapters two and three of this document were written as manuscripts intended for publication in scientific journals. Brief summaries and descriptions of the original manuscripts serving as chapters are detailed in following sections along with the co-authors and the submission dates.

Chapter Two Synopsis

This chapter tests the hypothesis that, during shock decompression associated with the excavation stage of impact cratering, water that crosses the vaporization curve expands explosively, increasing the degree of ejecta fragmentation and producing an overall shift toward smaller average ejecta particle diameter. To test this hypothesis, fragmentation experiments were conducted using a shock-tube apparatus at the University of Munich, Germany. Results of these experiments show that rock samples with water in about 15 – 50% open pore space produced much smaller grain sizes. Samples with >80% water in open pore space had an increase in fines and larger particles and a decreased number of intermediate particles. Fragments from experiments with >80% water in open pore space displayed a more compact grain shape, indicating that decompression of water caused fracturing perpendicular to the release wave front. These results provide insight into the morphology of Martian rampart craters and indicate that it may take less water than previously thought to produce fluidized ejecta because a

relatively small amount of vaporized water can reduce the average ejecta particle diameter so that it is small enough to interact with the thin Martian atmosphere to produce fluidized ejecta. The experiments are used to develop a hybrid model of single- and multi-layered ejecta formation on Mars.

Audrey Rager is the primary author on this article. Eugene Smith (University of Nevada Las Vegas), Bettina Scheu (University of Munich), and Don Dingwell (University of Munich) are coauthors. Eugene Smith provided input on experimental design and assisted with the interpretation of the data. Bettina Scheu ran the laboratory experiments and assisted with the interpretation of the data. Donald Dingwell provided expertise on fragmentation. This article was submitted for publication to the Geologic Society of America (GSA) Bulletin in December 2010.

Chapter Three Synopsis

This study looks at the effects of water within open pore space on rock fragmentation when the vaporization curve for water is not crossed. Results from these experiments indicate that, when the vaporization curve for water is not crossed, water within open pore space increases the fragmentation threshold of rocks, shifting the median grain size to larger sizes. This information is used to add a mechanism for the formation of double-layered ejecta to the hybrid model presented in chapter two. In the expanded model, the inner layer of double-layered ejecta is formed when there are very large ejecta blocks at the base of the curtain and much finer particles toward the top. In this situation, the larger blocks fall out first and produce the inner ejecta layer. A ring vortex is still formed where the ejecta curtain becomes permeable to the atmosphere. This

vortex deposits finer grained material behind the advancing ballistic ejecta and deposits the outer layer. At discrete locations within the ejecta curtain, some of the larger blocks extend outside the average curtain width. At these points Raleigh-Taylor or Kelvin-Helmholtz instabilities (Chandrasekhar, 1981; Boyce et al., 2010) form, punching holes in the curtain and forming scouring jets below the ring vortex. These jets carve out the radial lines in the inner and outer ejecta blanket.

Audrey Rager is the primary author on this article. Eugene Smith (University of Nevada Las Vegas), Bettina Scheu (University of Munich), and Don Dingwell (University of Munich) are coauthors. Eugene Smith provided input on experimental design and assisted with the interpretation of the data. Bettina Scheu ran the laboratory experiments and assisted with the interpretation of the data. Donald Dingwell provided expertise on fragmentation. This article was submitted for publication to the Journal of Geophysical Research (JGR) Planets in December 2010.

Chapter Four Synopsis

Chapter four summarizes the results of the two studies and a summary of the hybrid model of fluidized ejecta emplacement. Future research topics are also discussed.

CHAPTER TWO

THE EFFECTS OF WATER VAPORIZATION ON ROCK FRAGMENTATION DURING RAPID DECOMPRESSION: IMPLICATIONS FOR THE FORMATION OF FLUIDIZED EJECTA ON MARS

Abstract

Crater and ejecta morphology provide insight into the composition and structure of the target material. Fluidized ejecta surrounding Martian rampart craters is thought to result from the addition of water to the ejecta during impact into a water-rich (ice or liquid) regolith. In this study, an alternate hypothesis that the decompression of a rock-water mixture across the vaporization curve for water during the excavation stage of impact cratering results in an increased proportion of fines in the ejecta is tested. This increase in fine material causes the ejecta to flow with little or no liquid water. To test this hypothesis, fragmentation experiments were conducted on sandstone (28% open pore space) from the northern Eldorado Mountains, Nevada, using a shock-tube apparatus at the University of Munich, Germany. Rock samples containing 0 – 92% of their open pore space filled with water were subjected to 15 MPa at 177 ºC and 300 ºC and rapidly decompressed. When the vaporization curve for water is crossed, water content within open pore space has a significant effect on the grain size distribution and grain shape of the decompressed rock samples. When compared to control samples, samples with water in about 15 – 50% open pore space had much smaller grain sizes. Samples with >80% water in open pore space had an increase in fines and larger particles and a decreased number of intermediate particles. Fragments from experiments with >80% water in open pore space displayed a more equant grain shape, indicating that decompression of water

caused fracturing perpendicular to the release wave front. These results provide insight into the morphology of Martian rampart craters and indicate that it may take less water than previously though to produce fluidized ejecta.

Introduction

Impact crater and ejecta morphology reveal information about the structure and composition of the target. This is a topic of special interest on Mars where the presence of fluidized ejecta may provide clues to the history of water on the Martian surface. This study tests the hypothesis that the vaporization of water during the excavation stage of impact cratering increases the amount of rock fragmentation as measured by an overall decrease in the average grain size. Because smaller particles flow more easily than larger blocks, less water is required to produce fluidized ejecta than is currently thought. To test this hypothesis, rock fragmentation experiments were conducted using the shock tube apparatus in the Earth and Environmental Science Department of the University of Munich (Alidibirov and Dingwell, 1996a and 1996b). This section includes a discussion of Martian rampart craters morphology and distribution and current models for their formation.

Background

Martian Rampart Craters

Imagery from the Viking Orbiter cameras, Mars Global Surveyor (MGS), Mars Orbital Camera (MOC), Mars Odyssey Thermal Emission Imaging System (THEMIS), and Mars Reconnaissance Orbiter (MRO) revealed that Martian impact craters are very different from the radial ejecta on the Moon and Mercury (Carr et al, 1977; Barlow,

2005). Most Martian impact craters have fluidized ejecta (89% of 10, 651 cataloged craters ≥5 km diameter; Barlow, 2005) that hug topography and terminate in a distal rampart about 1.5 to 2 crater radii from the crater rim (Barlow, 2005; Garvin et al., 2000, 2003; Melosh, 1989). Barlow (2005) classified three types of fluidized ejecta (Figure 1): (1) single layer ejecta (SLE), (2) double layer ejecta (DLE), and (3) multiple layer ejecta (MLE).

Secondary craters are rare within the fluidized ejecta (Barlow, 2003b, 2005) blanket. Beyond the rampart, secondary craters extend many crater radii beyond the edge of the blanket (Barlow, 2005). For example McEwen et al. (2003) identified a 10-km-diameter crater in the Cerberus region of Mars that has strings of secondary craters extending more than 800 km from the rim but no secondary craters within the fluidized ejecta. These extensive secondary crater strings outside of the fluidized ejecta provide important constraints on the cohesiveness of the target material (Head et al., 2002) and any model of rampart crater formation must account for this distinctive feature.

Fluidized ejecta morphologies do not appear to correlate with elevation or terrain age and there is only a weak correlation with terrain type (Mouginis-Mark, 1979; Costard, 1989; Barlow and Bradley, 1990, Barlow, 2005). However, layered ejecta morphologies do exhibit a strong relationship with crater diameter and geographic location (Figure 2; Barlow, 2005). In the Martian equatorial region (±30º latitude), SLE craters are generally ~5 to 20 km in diameter. However, at higher latitudes, SLE craters are <1-65 km in diameter (Mouginis-Mark, 1979; Kuzmin et al., 1988; Costard, 1989; Barlow and Bradley, 1990; Barlow, 2005). DLE craters are concentrated at higher latitudes, particularly in the northern plains. DLE are typically 5-25 km in diameter.

MLE craters are usually in the 20-45 km diameter range. MLE tend to be concentrated in lower latitudes.

Models for Fluidized Ejecta Formation

There are two models for the formation of fluidized ejecta on Mars (Barlow, 2005): the atmospheric model and the subsurface volatile model. In this section, both models are described with special attention to previous studies that are incorporated into our proposed model for fluidized ejecta formation.

The Atmospheric Model

The atmospheric model for fluidized ejecta formation states that the thin Martian atmosphere is the medium in which ejecta are entrained (Schultz and Gault, 1979a and 1979b; Schultz, 1992a and1992b; Barnouin-Jha and Schultz, 1998; Barnouin-Jha et al., 1999a and 1999b; Barlow, 2005). Laboratory and experimental studies (Schultz and Gault, 1979; Schultz, 1992a and1992b; Barnouin-Jha and Schultz, 1998; Barnouin-Jha et al., 1999a, 1999b) show that atmospheric turbulence produces a vortex ring that entrains, transports, and deposits fine-grained ejecta in a layered pattern (Barlow, 2005). In this model, larger material is ballistically emplaced ahead of the vortex ring. As the vortex ring passes, it may remobilize these larger clasts and pile them up in the distal rampart. Ejecta composed of fine grain material can flow without an accompanying gas or liquid phase (Schultz, 1992a). However, for the ejecta to flow in this manner it is necessary that the target material be composed of fine grain material or that the impact itself produces an enormous amount of fine grained material during impact excavation (Schultz, 1992a; Boyce and Mouginis-Mark, 2006).

Schultz (1992a) conducted laboratory experiments using the vertical gun at the NASA Ames Research Center to investigate the complex interactions between impact ejecta and the atmosphere. Schultz (1992a) found that, under vacuum conditions, ballistic ejecta form the classic cone-shaped profile. However, as atmospheric density increases, the ejecta form at a higher angle (from horizontal), bulging at the base and pinching above (Figure 3). This change in the ejecta curtain results from the combined effects of deceleration of ejecta smaller than a critical size and entrainment of these ejecta within atmospheric vortices created as the ejecta curtain moves outward displacing the atmosphere. The degree of ejecta entrainment depends on the ratio of drag to gravity forces acting on individual ejecta and the intensity of the winds created by the advancing ejecta curtain (Schultz, 1992a). The degree of ejecta entrainment is positively correlated with atmospheric density and ejection velocity, but negatively correlated with ejecta density and size. He found that a wide variety of nonballistic ejecta styles were produced by varying ejecta sizes even without water in the target and that ejecta run-out distances scaled to crater size on Mars should increase as $R^{1/2}$ (where R is crater radius). Therefore, long run-out ejecta flows dependent on crater diameter do not necessarily reflect the depth to a reservoir of water.

According to Schultz (1992a), nonballistic ejecta emplacement results from a two-stage process. First, the ejecta are aerodynamically decelerated to near-terminal velocity. Next, the ejecta are entrained in atmospheric turbulence created by the outward expanding wall of ballistic ejecta. Conditions leading to nonballistic ejecta emplacement depend on a critical ejecta size which depends on (1) crater size (i.e., ejection velocity), (2) ejecta size, and (3) atmospheric pressure (i.e., density).

Schultz (1992a) found that ejecta morphology becomes increasingly complex with increasing atmospheric pressure, but is relatively independent of atmospheric density for a given pressure. For given impact conditions, aerodynamic drag force relative to gravity increases if either particle size or particle density is decreased (Schultz, 1992a). At high atmospheric densities, the coarser size fraction retains the undistorted funnel-shaped ejecta curtain (Schultz, 1992a). However, the fine size component creates a separate curtain characteristic of an impact into a target consisting of fine-size particles alone under vacuum conditions. Schultz's (1992a) experiments showed that the two curtains merge at the base. According to Schultz (1992a), this indicates aerodynamic sorting during ballistic ejection and flight may not result in aerodynamic sorting during deposition, except for very late stage fallout.

Both particle size and atmospheric density affect the shape and evolution of the ejecta curtain after crater formation (Schultz, 1992a), indicating aerodynamic drag plays a role in the formation of nonballistic ejecta. Schultz (1992a) also found that, under high atmospheric densities, a basal ejecta surge develops and advances outward at velocities that exceed the ballistic ejecta curtain under vacuum conditions.

Entrainment of fine ejecta plays an important role in the formation of nonballistic ejecta (Schultz, 1992a). Increasing levels of entrainment results in the onset of more complex ejecta morphologies; less entrainment suppresses the complex ejecta morphologies even at high atmospheric pressures. Schultz (1992a) concluded that rampart formation is a late-stage process and requires finer fractions and that ejecta exhibited fluid-like behavior even in the absence of water due to an increase in fine materials.

Barnouin-Jha et al. (1999a) conducted wind-tunnel experiments on the interaction of an atmosphere with an ejecta curtain. According to Barnouin-Jha et al. (1999a), ejecta curtain width and velocity, particle concentration, size distribution and motion parallel to the curtain, and the density, viscosity, and compressibility of the surrounding atmosphere all influence the vortex circulation strength. The circulation generated by the ejecta curtain (Figure 4) is a function of the length (L) and outward curtain velocity (U) of the curtain where it transitions from impermeable to permeable (Barnouin-Jha and Schultz, 1996).

Permeability of the ejecta curtain to the surrounding atmosphere is the primary factor controlling the circulation generated by the advancing ejecta curtain. Curtain porosity (ϕ), curtain width (w), most common curtain ejecta particle diameter (d), the velocity of the surrounding atmosphere impinging on the curtain (U), and the surrounding atmospheric density (ρ) and viscosity (μ) are shown in Figure 4.

Barnouin-Jha and Schultz (1998) also showed that flow instabilities (Chandrasekhar, 1981) in the vortex result in the sinuosity or lobateness of distal ejecta facies observed in laboratory studies. Laboratory results (Schultz and Gault, 1979a, 1979b, and 1982; Schultz, 1992a and1992b) also indicate that the vortex winds can mobilize and saltate target and larger ejecta that were deposited ballistically ahead of the vortex. Wind circulation (or flow strength) generated by an advancing ejecta curtain controls most aspects of the atmospheric ejecta deposition process. Wind circulation behind the ejecta curtain is a function of the velocity and length of the curtain (Figure 4) where it transitions from an impermeable to a permeable barrier to the atmosphere (Barnouin-Jha and Schultz, 1996).

Windtunnel experiments (Barnouin-Jha et al., 1999a) indicate that hydraulic resistance (a measure of energy losses for one-dimensional porous flow) determines where along an ejecta-like porous plate becomes effectively permeable. Barnouin-Jha et al., (1999b) point out that published data linking hydraulic resistance to the thickness, porosity, and dominant particle size comprising a porous boundary, and atmospheric properties such as viscosity and density (Idelchik, 1994) can be combined with atmosphere and cratering models (Maxwell, 1977a,1977b, and 1977c; Schultz and Gault, 1979a and 1979b; Orphal et al., 1980; Housen et al., 1983) to determine the length of the impermeable portion of the curtain and the time when it transitions from impermeable to permeable.

Wind tunnel (Barnouin-Jha et al., 1999a) and numerical (Barnouin-Jha, 1999b) results show that first order circulation (Γ, m/s) is determined by flow separation. Barnouin-Jha and Schultz (1996) showed that circulation controls the velocity and the entrainment capacity of the vortex winds developed behind the advancing ejecta curtain. The entrainment capacity, in turn controls the ejecta deposition by the vortex. The impermeable curtain length (L) can be estimated using the hydraulic resistance criteria ζ_{cr} =10 given ϕ, w, d, ρ, and μ along the length of the ejecta curtain based on ejecta scaling rules (Schultz and Gault, 1979a and 1979b; Housen et al., 1983), atmospheric conditions, and assumptions on the ejecta size distribution, atmospheric conditions, and assumptions on the ejecta size distribution (Barnouin-Jha et al., 1999a).

Circulation of the curtain-derived vortex is what ultimately controls nonballistic ejecta deposition (Barnouin-Jha et al., 1999a). The circulation of the curtain-derived vortex is controlled by the permeability of the ejecta curtain. To estimate the initial

circulation of the vortex, the time when the curtain becomes fully permeable must be known. Experiments conducted by Barnouin-Jha et al. (1999a), show that this transition depends upon the dominant grain size of the target present in the ejecta. For experimental impacts in coarse sand (Schultz, 1992a; Barnouin-Jha and Schultz, 1996 and 1999a) this transition occurs slowly. However, the transition occurs quickly for fine-grained pumice.

The Subsurface Volatile Model

In the subsurface volatile model, impact into a volatile-bearing target results in a vapor cloud that deposits the entrained ejecta as a flow surrounding the crater (Baratoux et al, 2002a and 2002b; Barlow, 2005; Carr et al., 1977; Greeley et al., 1980;Greeley et al., 1982; Mouginis-Mark, 1987; Stewart et al., 2001; Wohletz and Sheridan, 1983). In this model, ejecta interact primarily with this vapor cloud rather than the atmosphere. Support for this model comes from (1) correlation of rampart craters with other geomorphic features associated with subsurface water (Costard and Kargel, 1995; Carr, 1996), (2) relationships between rampart crater diameter and morphology with latitude (Costard, 1989, Barlow and Bradley, 1990), (3) hydrocode simulations of impacts into mixtures of water and rock (Stewart et al., 2001; O'Keefe et al., 2001; Stewart and Ahrens, 2003; Stewart et al., 2003; Senft and Stewart, 2007, 2008, and 2009), and (4) experiments into ice-rich targets (Stewart and Ahrens, 2005).

Stewart et al. (2001) conducted experiments and modeling of impacts onto ice-rock mixtures to quantify the effects of subsurface H_2O on ejecta distribution, rampart and pedestal formation, and crater floor morphologies. They propose that various ejecta morphologies (SLE, DLE, and MLE) are produced by increasing amounts of ice. They

found that the high volatility of H_2O modifies the crater formation process producing more vapor, higher ejection angles, fluidized ejecta blankets, and larger crater rim uplift.

Ice is much more compressible than rock. Therefore, about 4 times more energy is deposited in ice than rock during typical shock pressures (Stewart et al., 2001; Stewart and Ahrens, 2003). Ejection angle increases as strength decreases (Melosh, 1984). Through their experiments, Stewart et al, (2001) found that ice will melt completely upon release from shock pressures ≥2-3 GPa. These pressures correspond to about 7 projectile radii (R_p) for asteroidal impacts on Mars (Stewart et al., 2001).

Stewart et al., (2001) modeled impacts into rock-ice mixture using the Eulerian finite difference code, CTH (McGlaun and Thomson, 1990), and found that ejection angles at the point of impact are high (70˚) and nearly constant in the zone of melted ice and brecciated rock ($7R_p$) for a rock-ice mixture with 20% volume subsurface ice. In contrast, pure rock targets had a peak ejection angle of about 60˚. In all experiments, the ejection angles decrease to about 45˚ near the crater rim. Models with peak ejection angles of 70˚ (consistent with 10-20%vol ice) produced ejecta layers of consistent thickness that were high in water content. Models with initial ejection angles of about 80˚ corresponding to increased amounts of water produced an ejecta blanket that was more pronounced with a large step in ejecta thickness about 0.6 crater radii (*Rc*) from the rim.

O'Keefe et al. (2001) calculated geologic strength models using shock wave physics code CTH (McGlaun and Thomson, 1990). They found that since ice is more compressible than rock, more work was done on the ice. Consequently, a larger volume of ice was subjected to shock-induced phase transformations compared to the rocks. In their numerical model, a small zone of rock (~ 1 impactor radius, *a*) was melted and very

little was vaporized (<1*a*). Rock that was excavated did not undergo any major phase transitions. However, ice was vaporized to about 1*a* and ice was melted within about 7*a*. From 1 to 7*a*, the excavated material is a mixture of rock and water. Ejection angles are also high (70°) within this region and decrease away from the impact point until they reach a 45° angle near the crater rim. O'Keefe et al., (2001) note that there is a clear separation in ejecta trajectories in their model at about 7*a*. They attribute this separation to differences in strength between rock and water in the excavation cavity. They conclude that the ejecta will contain a significant amount of water allowing for fluidized flow.

To understand the amount of liquid water that was present in Martian ejecta blankets, Stewart et al. (2003) conducted simulations of impact cratering onto ice-rock mixtures using the shock physics code CTH (McGlaun and Thomson, 1990). They used the results of these simulations to calculate the volume of ground ice subject to shock-induced melting and the amount of excavated liquid water. They assumed the ground ice was distributed within pore spaces and cracks in the Martian regolith at average Martian surface temperatures (200 K). The atmosphere was approximated at the present day mean of 7 millibar. The surface porosity was varied from 0-20%. Regolith pore space volume (ϕ_0) was modeled assuming a decrease in depth, *z*, as $= \phi_0 e^{(-z/K_z)}$, where ϕ_0 is the surface porosity and K_z is the decay constant (3 km). The dynamic strength of the Martian surface was constrained to ~10 Mpa. Projectile diameter was varied from 100 to 2000 m.

At temperatures between 150 and 273 K, ice in the Martian crust will begin to melt after experiencing shock pressures between 2.0 and 0.6 GPa, respectively (Stewart et al., 2003). The ice will melt completely after being released from shock pressures

above 5.5 and 3.7 GPa. Stewart et al. (2003) concluded that, in the present climate, about half the excavated ice is melted by impact shock. About 60% of ground ice will completely melt in equatorial zones while at the poles more that 20% will be melted. Their results indicate that ejecta fluidization does not require pre-existing water near the surface because shock-melting of ground ice will introduce large quantities of liquid water into the ejecta blanket.

Summary

According to Barlow (2010), the relative role of subsurface volatiles versus the atmosphere in the formation of layered ejecta blankets is one of the major questions remaining concerning the geology of Mars. Barlow (2005) suggests that fluidized ejecta are produced by some combination of the atmospheric and subsurface volatiles models. Building upon Schultz's (1992a) idea that ejecta can flow without water if the particles are small enough, the goal of this study is to test the hypothesis that the vaporization of water during the excavation stage of impact cratering is the mechanism that decreases the size of ejecta and facilitates its fluidized emplacement. The interaction between water and rock during decompression may be the bridge between the atmospheric and subsurface volatile models.

Methods

Fragmentation Methods

The shock tube apparatus, described in detailed in Alidibirov and Dingwell (1996a), was used to conduct decompression experiments on rock-water mixtures. This instrument consists of a lower chamber which can be pressurized up to 40 MPa with Ar

gas (Figure 5). This lower chamber is separated from the upper chamber (room temperature and pressure) by a series of metal diaphragms. These diaphragms are of various thicknesses and are inscribed with a ring and cross pattern that cut into the diaphragm at various depths. The combinations of diaphragm material (Cu or Al) and thickness and imprint depth determine the pressure at which the diaphragm will open. When the diaphragm breaks cleanly, a shock wave propagates through the lower chamber as the Ar gas is instantaneously released into the low-pressure, upper chamber. This shock wave travels through the sample from the top to the bottom in the lower chamber. As the release wave travels down through the sample, the sample is unloaded and fractures occur parallel to the release wave front. The fragmented rock particles are accelerated and eject into the upper chamber.

Rock samples were tested at two temperatures (177 ºC and 300 ºC) and one fragmentation pressure (15 MPa). In order to keep the water in a liquid state, the samples were initially pressurized to about 10 MPa (Figure 6). The autoclave was then heated to the desired temperature using a cylindrical furnace fitted snuggly to the outside of the autoclave (Figures 5 and 6). Pressure was increased incrementally approaching 15 MPa to keep the system from crossing the vaporization curve before failure of the diaphragms. Whenever possible, the furnace was held at the experimental temperature for 15 minutes to allow the entire autoclave to reach the experimental temperature. At the end of this waiting period, additional Ar gas was added to the lower chamber to initiate failure of the diaphragms. Occasionally, the diaphragms failed before this waiting period was completed. But in all experiments, the system decompressed at about 15 MPa, creating a

release wave that propagated downward and ejected the rock fragments into the upper chamber.

Sample Preparation

Our purpose is the investigation of the behavior of water-bearing Martian regolith when the rock-water mixture crosses the vaporization curve during the rapid decompression associated with crater excavation. Carrying out these experiments requires a rock that is as close as reasonably possible to a generic regolith composition and structure for Mars. The Martian surface is covered by sedimentary deposits derived from basalt and andesite (Bandfield et al. 2000; Malin and Edgett, 2000a and 200b; Barlow, 2008). A volcaniclastic rock from the northern Eldorado Mountains of southern Nevada, U.S.A. (Anderson, 1971) was used for these experiments. This is a thinly bedded (1 – 3 mm) volcaniclastic sandstone composed of olivine, quartz, and occasional small (<3 mm) rock and pumice fragments derived from mid-Miocene Patsy Mine basalt, dacite, and rhyolite. This rock was chosen for two reasons. First, it is composed of eroded volcanic rocks similar to Martian regolith. Second, the rock's uniform structure and composition make it ideal for use in these experiments where the physical property of the rock must be consistent for each trial. The rock samples used in this investigation are not meant to be an accurate representation of the Martian regolith. Indeed the regolith is made up of varying rock types. It would be impossible to find one rock that would fit all target conditions on Mars. The rock used is similar to many rocks on Mars, in particular those found at Meridiana Planum (Squyres et al., 2006), in that it is a sedimentary rock derived from volcanic rocks. It contains basalt, which is common on Mars, but it also contains rhyolite, which is not. Because no study of this kind has ever been conducted, it

is more important to test a homogeneous material that allows testing the effects of vaporization of varying amounts of water.

The rock was cut into 2.5-cm-diameter, 4-cm-long cylindrical samples. The samples were placed in a 190°C oven overnight to drive off water from the open pore space. After cooling in a desiccator, each sample was weighed in grams on an electronic balance. Two diameter measurements were made using digital calipers, one at each end of the cylinder (about 0.5 to 1 cm from the end). The average of these two diameters was used to calculate the sample volume (V_{calc}). Each sample was placed in a helium pycnometer to determine the sample volume minus open pore space (V_{hc}). The percent of open porosity ($[[V_{calc} - V_{hc}]/ V_{calc}] \times 100\%$) was then calculated. The sandstone has an average calculated density of 1.8958 g/cm^2 and average measured density of 2.1627 g/cm^2, with standard deviations of 0.005 and 0.0053, respectively. The average open porosity of the samples is 27.4450%, with a standard deviation of 3.3277. Samples were stored in air-tight containers until experimental preparation.

Prior to the experiment, each rock sample was placed in a steel crucible cylinder open on one end with an interior diameter slightly smaller than the rock sample. This tight fit facilitates fracture of the sample during decompression by preventing the entire rock cylinder from ejecting into the upper chamber upon decompression. This was accomplished by placing the rock sample on the open end of the cylinder and heating the steel cylinder with a hot air gun causing it to expand slightly while pressing the rock into the cylinder using a hydraulic press. Each sample in its crucible was stored in an air tight container until the experiment was conducted (no more than 24 hours).

Methods for adding water to the sample

To test the effects of water content on rock fragmentation, varying amounts of water were added to each sample. The goal was to cover the range of possible percent open pore space (%OPS) water contents from 0 – 100 at approximately 15%-intervals (0%, 15%, 30%, 45%, 70%, and 100%). To determine the amount of water to add to each sample, the volume (ml) of open pore space for was calculated for each sample, determined the volume of the desired %OPS water, and added that amount of distilled water to the top of the rock sample in the crucible. The sample was placed in a vacuum to draw the water as evenly as possible through the sample. After a few hours, the sample was inspected to determine whether the top of the rock sample and the bottom (visible through a small hole) appeared to have about the same degree of wetness. The sample was weighed to determine if it still had the correct amount of water. More water was added if necessary. The sample was iteratively inspected and weighed, adding water as necessary, until the target %OPS water closely approximated. The sample was weighed immediately prior to placement in the lower chamber of the shock tube apparatus and the actual %OPS water was recorded (Table 1).

Sieving methods and grain shape analysis

After each experiment, a high-pressure water hose was used to flush the upper tank. The rock fragments were collected, dried, and sieved between sieve sizes -4 and 4 phi at 0.5-phi intervals. The contents of each sieve were weighed on an electronic balance and the weight percent of each sieve interval was calculated. A grain size distribution curve was plotted on an arithmetic probability grid for each sample using GRANPLOT, a Microsoft Excel Spreadsheet developed by Balsillie et al. (2002). Inman (1952)

parameters were calculated, including (1) median diameter ($Md_\phi = \phi_{50}$), the phi-size where the cumulative distribution curve crosses the 50% mark; (2) graphical standard deviation ($\sigma_\phi = [\phi_{84} - \phi_{16}]/2$), which is a measure of sorting; and (3) first order skewness ($\alpha_\phi = [((\phi_{84} + \phi_{16}) - Md_\phi]/\sigma_\phi$), which is a measure of asymmetry of the distribution. Also calculated was kurtosis, a measure of the peakedness of the distribution, and the short (S), intermediate (I), and long (L) axes of each fragment from phi sizes -1.5 and -2 for each experiment. Using the S/L index and form index ([L-I]/[L-S]) developed by Sneed and Folk (1958), the grain shape for each sample was determined. The average S/L and form index as well as standard deviation were calculated and plotted for each experiment.

Results

Grain-size Distribution

Although the control experiments (samples 102 and 422; 0% OPS H_2O; 177 and 300 ˚C, respectively) were run at different temperatures, both have an overall similar grain size distribution as evidenced by their similar median diameter (Md_ϕ), graphic standard deviation (σ_ϕ), and shape for their frequency distribution and cumulative frequency (Figures 7A, 7B, and 8). For sample 102 (0% OPS H_2O, 177 ˚C) Md_ϕ = -1.4265 ϕ and σ_ϕ = 1.45 ϕ. Sample 422 (0% OPS H_2O, 300 ˚C) has Md_ϕ = -1.3078 ϕ and σ_ϕ = 1.45 ϕ (Figures 7A, 7B, and 8; and Table 2). In addition, they have similar values of skewness (sample 102: 1.2575; sample 422: 1.0919) and kurtosis (sample 102: 4,2256; sample 422: 4.0003) (Table 2). The similarities in grain size distribution indicate that temperature did not play a significant role in the fragmentation behavior of the control samples. As water is added to the open pore space of the sample, there is a shift toward

smaller grain sizes in the grain size distribution of the fragments produced by shock decompression. Sample 110 (16.02% OPS H_2O, 177 ˚C) (Figures 7C and 8) has smaller median diameter (Md_ϕ = -0.5099) but similar graphical standard deviation (σ_ϕ = 1.76) when compared to the control samples. The frequency distribution is less positively skewed (0.9312) and less peaked (2.9877) than the control samples (Figures 7A-C, and 8; Table 2).

Increasing the %OPS H_2O to about 30% results in a greater shift toward smaller grain sizes. Samples 108 (31.44% OPS H_2O, 300 ˚C) and 426 (30.02% OPS H_2O, 177 ˚C) have median diameters of -0.0744 and -0.0203 ϕ, respectively (Figures 7D, 7E, and 8, Table 2). The graphical standard deviations, 1.77 for sample 108 and 1.88 for sample 426 (Figure 8, Table 2), are similar to the control (0%) and 16.02% OPS water experiments. These two experiments produced distributions less peaked than the control experiments, with kurtosis values (Table 2; sample 108: 2.880; sample 426: 2.8728) similar to each other and sample 110 (16.02 OPS H_2O). The grain-size distributions are also less skewed than the control samples (Table 2; sample 108: 0.8417; sample 426: 0.0523). The grain-size distributions for samples 108 and 426 do differ from each other in one way. There is a spike at -3.5ϕ in the frequency distribution for sample 426 (Figure 7D) that is shown as a plateau on the left side of the cumulative frequency curves (Figures 7D and 8). This spike is the result of a single fragment in the 3.5ϕ sieve size. With the exception of that spike, the experiments with approximately 30% OPS water (samples 108 and 426) have grain-size distributions that are very similar to each other even thought they were conducted at different temperatures. This also may indicate that temperature was not an important factor in the fragmentation behavior of these samples.

The experiment for sample 109 (53.26% OPS H_2O) was run at 177 ˚C (Figures 7F and 8). This sample had a median diameter of -0.2490 and standard deviation of 1.72 (Figure 8, Table 2). The grain size distribution for this experiment is shifted toward much smaller grain sizes when compared to the control samples. However, the median grain size is only slightly smaller than the 16.02% OPS water sample (110). And, it is slightly larger than the samples with approximately 30% OPS water (108 and 426). This sample is slightly less positively skewed (0.9993) and peaked (3.0966) than the control sample (Figures 7F and 8; Table 2).

With a median diameter of -1.0947 ϕ and graphical standard deviation of 1.48 ϕ, sample 114 (61.57% OPS H_2O, 177 ˚C) (Figures 7C and 8; Table 2) has a grain size distribution very similar to the control samples (Figures 7A and B, Table 2). Even the skewness (1.1631) and kurtosis (4.0186) values are similar to the 0% OPS water samples (Table 2).

For samples 112 and 113, the goal was to fill all the open pore space with water. However, the interconnectedness of the pore space (i.e., permeability) resulted in some of the water leaking out of the sample and out through the bottom of the crucible so that not all of the open pore space was filled with water. Therefore, samples 112 (300 ºC) and 113 (177 ºC) contained 90.18% and 87.74% OPS water, respectively. Unlike the other paired experiments conducted at 177 and 300 ºC, these water-saturated samples produced grain size distributions that were different from each other. Sample 112 has a median diameter of -1.1701 ϕ and graphical standard deviation of 2.38 ϕ (Figure 8; Table 2). Sample 113 has a median diameter of -2.3419 ϕ and graphical standard deviation of 1.62 ϕ (Figure 8; Table 2). The median diameter for sample 113 is much lower than the control samples,

however it has a similar graphical standard deviation skewness (1.3483) and kurtosis (4.5217) (Figures 7H and 8; Table 2). Conversely, sample 112 has a median diameter similar to the control samples; however its graphical standard deviation, skewness (0.5375), and kurtosis (2.5868) differ from the control samples (Figures 7A, B, and I; Table 2). In fact, all experiments have a similar graphical standard deviation (ranging from 1.46 to 1.88 ϕ) except for sample 112. The larger standard deviation can be seen in the more uniform spread of the frequency distribution (Figure 7I) and the lower slope of the cumulative frequency distribution (Figure 8).

A plot of median diameter against graphical standard deviation (Figure 9) is a measure of sorting. The control samples (0% OPS H_2O) have similar median diameters (around -1.3 to -1.45 phi) and sorting coefficients (~1.45). Adding 16.02% OPS water increases the median phi size (decreases the median diameter) to around -0.5. Adding around 30% water shifts the median diameter to even smaller sizes (around 0 phi). But, as additional water is added, the phi size decreases until it reaches sizes near the control sample. In the case of sample 113, filling the open pore space with 87.74% produced a median diameter larger than the control sample after shock decompression across the vaporization curve for water.

It appears that the maximum shift toward smaller median diameters in the grain size distribution is achieved with about 30% OPS water. This is best shown in Figure 10 which plots %OPS water against median diameter. Median grain size as measured in phi increases from the control sample to sample 110 containing 16.02% OPS water. The median diameter peaks at samples 108 (31.44% OPS H_2O) and 426 (30.02% OPS H_2O).

Increasing the amount of %OPS water above about 30% increases the median diameter until it reaches a value approaching or lower than the control samples.

Another way to assess fragmentation behavior is the proportion of fines produced by each experiment. Weight percent fines (>4ϕ) are plotted as a function of %OPS water for each sample in Figure 11. There is a general trend to increase the weight proportion of fines between 16 and 56% OPS water with a dip around 30% OPS water. Although the proportion of fines drops off with increased amounts of water (>62% OPS H_2O), the proportion of fines for these experiments is still increased 73% for sample 112 (90.18% OPS H_2O) and 95% for sample 114 (61.57% OPS H_2O). As with the grain-size distribution, the proportion of fines for sample 113 (87.74% OPS H_2O) is about the same as for the control samples (about 2% increase).

Qualitative Observations and Grain-shape Analysis

For the water-saturated experiments, the grain shape of the fragments seemed to be more equant than the fragments from other experiments. To quantify the variations in shape, the short (S), intermediate (I), and long (L) axes of particles in phi sizes -1.5 and -2 for all experiments were measured. These phi sizes were the only ones measured because they were large enough to be measured with calipers and all samples had particles in these two combined sieve sizes (only sample 426 had no particles in sieve size -2ϕ). Results of the shape analysis are shown in Figure 12. The mean values of S/L and the form index (L-I/L-S) were plotted for each experiment (Sneed and Folk, 1958). Ellipses around each measurement represent one standard deviation. The water-saturated samples (sample 112 and 113) plot in the compact bladed field near the boundary it shares with the bladed category. First standard deviation ellipses overlap. All other

samples plot within the bladed field and have overlapping first standard deviation ellipses. The first standard deviation ellipses of the water-saturated samples do not overlap with the other samples.

Discussion

Increased water in the open pore space does not result in an overall decrease in grain size, but water vaporization does affect the grains size distribution of the ejecta. The degree of fragmentation appears to peak around 30% OPS water (sample 108: 31.44% OPS water, 300 ˚C; sample 426: 30.02 % OPS water, 177 ˚C) (Figures 7D, 7E, and 8, Table 2). Sample 426 (30.02% OPS H_2O, 300 ˚C) had one fragment in -4 ϕ, which produced a flattening in the curve up to -2 ϕ. Slightly larger median diameter sizes were produced by the 53.26% OPS and 16.02% OPS water experiments which have median diameters of -0.2490 ϕ and -0.5099 ϕ, respectively. Experiments using 0%, 61.57%, and 90.18% OPS water produced a sample with an even larger median diameter of about -1.25 ϕ. The experiment that resulted in the largest median diameter contained 87.74% OPS water and was run at 177 ºC. All samples have similar sorting coefficients as represented by the similar slope to each curve.

Control samples have the lowest proportion of fines. The weight percent of fines increases drastically at 16% OPS water, decreases somewhat at around 30% OPS water, increases again around 50% OPS water, then drops again as the sample approaches water saturation (samples 112 and 113). Experiments for 0%, ~30%, and water-saturated samples were conducted during the same week. Two qualitative observations suggest another fracture mechanism contributes to the difference in grain shape. First, the water

saturated experiments were much louder than the other experiments. Second, fine particles were found clinging to the lid and rim of the upper tank after the water-saturated experiments. This was not the case for any of the other experiments.

The shape of the water saturated samples is blockier, indicating that the vaporization of water in this case may cause fracturing perpendicular to the release wave front (Figure 13). The water saturated samples were much louder than the other samples. They also caused ejecta to be expelled to the top of the chamber. These two qualitative observations indicate that the water saturated samples may have caused the rock to be expelled into the upper chamber with more force and at a higher speed. Future studies may involve high speed photography and/or use of a pressure transducer to measure the speed of the ejection. One of the characteristics of rampart craters is that they generally lack secondary craters within the ejecta blanket. If high water content results in a higher ejection velocity and force, this could cause larger blocks to be transported farther than is typical for ballistically emplaced ejecta.

Not all samples were held heated at peak furnace temperature for 15 minutes before fragmentation, so it is not absolutely certain that the crucible and sample equilibrated and reached the target temperature. The timing of the diaphragm failure is often beyond experimental control. Diaphragms may fail due to variations in the thickness of the imprint depth. For future investigations, the temperature of the sample chamber will be measured at various times during heating so that if early diaphragm failure occurs, an accurate estimate of the temperature of the sample during fragmentation can be obtained. This will provide confirmation that water added to the sample crossed the vaporization curve.

It is possible that not all of the water contained in the open pore space of each sample was driven off. Therefore the actual %OPS water probably varies from that listed in Table 1. However, all samples were treated consistently, so the relative effects of adding water can still be measured.

The distribution of open pore space in the sample may be another factor affecting grain size distribution of the fragmented samples. If a sample's open porosity varies too much within a sample, it may cause part of a sample to fracture more than another and that may account for some differences in grain size distribution curve shape. Future studies will account for this problem by measuring permeability and mapping the open pore space with tomography.

Proposed Model for the Formation of SLE and MLE ejecta

Fluidized ejecta are present on Venus (Figure 14), a planet with a very thick atmosphere but without subsurface volatiles; and, on Ganymede (Figure 15), a body with an icy surface but no atmosphere. These situations represent end-members of the fluidized ejecta mechanism. Venus represents the atmospheric end-member, and Ganymede represents the subsurface volatile end member. With its relatively thin atmosphere and ice-bearing regolith, Mars is somewhere in between.

In laboratory experiments, Schultz (1992a) produced fluidized ejecta in two ways. First, in a vacuum, fluidized ejecta could be produced by impact into targets with fine grain particles. Second, impact into coarser grained materials produced fluidized ejecta when the atmospheric pressure was increased. Venus is an example of the latter case. Schultz contends that fluidized ejecta are produced at lower pressures if the ejecta particles are small enough. The goal of these experiments was to test the idea that

explosive vaporization of water during rapid decompression associated with impact cratering is the mechanism that introduces these fine particles into the ejecta. Our results indicate that water vaporization can affect the grain size distribution of ejecta particles.

Our results indicate that with ~28% open porosity, the grain size distribution is significantly reduced by water vaporization when the rock has about 30% of the open pore space filled with water. This begs the question of whether or not water crosses the vaporization curve during impact cratering. Experiments and modeling conducted by Stewart et al. (2003) indicate that a substantial amount of water ice is melted and vaporized during impact cratering. The proportion of subsurface ice that is melted or vaporized varies with impactor size (and consequently crater size), water content, and surface temperature (latitude). Stewart et al., (2003) found that for a 500-m diameter impactor, about half the amount of water within the excavation zone will melt and a quarter will vaporize. This amount of water is sufficient to drastically reduce the median diameter of the ejecta particles.

According to Barnouin-Jha et al. (1999a, b), during hypervelocity planetary impacts, ejecta are excavated along ballistic trajectories in an inverted cone shape that displaces the atmosphere as it advances and creates a vortex ring (Figures 4). This vortex ring can entrain, transport, and deposit ejecta and fine-grained surface materials. They concluded that ejecta curtain width and velocity, particle concentration, ejecta size distribution, motion of ejecta particles parallel to the curtain, and the density, viscosity, and compressibility of the surrounding atmosphere all influence the vortex circulation strength. The circulation generated by the ejecta curtain is largely a function of the length (L) and outward curtain velocity (U) of the curtain where it transitions from impermeable

to permeable (Barnouin-Jha and Schultz, 1996, 1999a, and1999b). Permeability of the ejecta curtain to the surrounding atmosphere is the primary factor controlling the circulation generated by the advancing ejecta curtain (Barnouin-Jha et al., 1999a; 1999b). The most common diameter size is a major factor affecting the length at which the curtain becomes permeable. Smaller ejecta diameter will result in a shorter length at which the curtain transitions from impermeable to permeable.

This study proposes that the decompression of water increases the degree of fragmentation of the ejecta and decreases the average ejecta size. Consequently, this decrease in average ejecta size lowers the length at which the ejecta curtain becomes permeable. This allows a vortex ring to form behind the ejecta curtain in a manner described by Schultz (1992a), Barnouin-Jha and Schultz (1996 and 1998), and Barnouin-Jha et al. (1999a, 1999b). The vortex ring winnows finer grained materials from the ejecta blanket, remobilizes material on the surface, and deposits the material in a fluidized ejecta blanket with a terminal rampart (Figures 1 and 4).

In addition to facilitating ejecta fluidization by creating smaller ejecta particles that interact with the atmosphere, the vaporization of water may also play a part in the dearth of secondary craters within the ejecta blanket. Results suggest it takes relatively small amounts of water (in a rock with ~28% open porosity, 30% of that open pore space is filled with water) to add a tremendous amount of fines to the ejecta.

Fluidized ejecta on Venus can be thought of as a purely atmospheric end-member of a hybrid atmospheric/sub-surface volatile model. The Venutian regolith contains no water; but, in this case, no sub-surface volatiles are required because the ejecta interact with Venus' thick atmosphere to produce lobate ejecta with large runout distances

indicating high ejecta mobility (Schultz, 1992a; Barnouin-Jha and Schultz, 1996 and 1998; Barnouin-Jha et al., 1999a and 1999b).

In the atmospheric model, fluidized ejecta are produced by interaction of ejecta with the atmosphere. Fluidized ejecta are produced when ejecta diameter is decreased or atmospheric pressure is increased (Schultz, 1992a). Under these conditions, the ejecta can flow and produce fluidized ejecta without any liquid water (Schultz, 1992a).

According to the sub-surface volatile model, fluidized ejecta are produced by the interaction of ejecta with subsurface volatiles. There are two subsets to this model. In one, the ejecta interact with the vapor cloud produced by release of volatiles during the impact (Wohletz and Sheridan, 1983). In the other subset of this model, the ejecta are fluidized by release of liquid water added to the ejecta during shock melting of ice (Stewart et al., 2003).

Conclusions

According to Barlow (2010), the relative role of subsurface volatiles versus the atmosphere in the formation of layered ejecta blankets is one of the major questions remaining concerning the geology of Mars. A hybrid of the subsurface volatile and atmospheric models is proposed for the formation of fluidized ejecta. In this model, rapid decompression of a rock-water mixture causes a portion of the water to vaporize (subsurface volatile model). This explosive vaporization is the mechanism that adds fine material to the ejecta and allows the material to be emplaced by the vortex ring behind the larger blocks in the advancing ejecta curtain (atmospheric model). This reduction in the grain size of the ejecta may reduce the length at which the ejecta curtain becomes

permeable to the atmosphere (Schultz, 1992a; Barnouin-Jha and Schultz, 1996 and 1998; Barnouin-Jha et al., 1999a and 1999b) and allow the formation of a vortex ring behind the advancing curtain. This ring is responsible for the fluidization of the ejecta. When a rock's pore space is nearly filled with water, larger blocks may be propelled further than expected, creating smaller secondary craters outside the fluidized ejecta blanket. This may explain why they are rarely found within fluidized ejecta blankets. More experiments are needed to better constrain the effects of water vaporization on rock fragmentation. Additional experiments to test other variables including rock type, porosity, and permeability are planned with the goal of providing information that can be included in numerical models of impact cratering so these models can be used to test the proposed hybrid model.

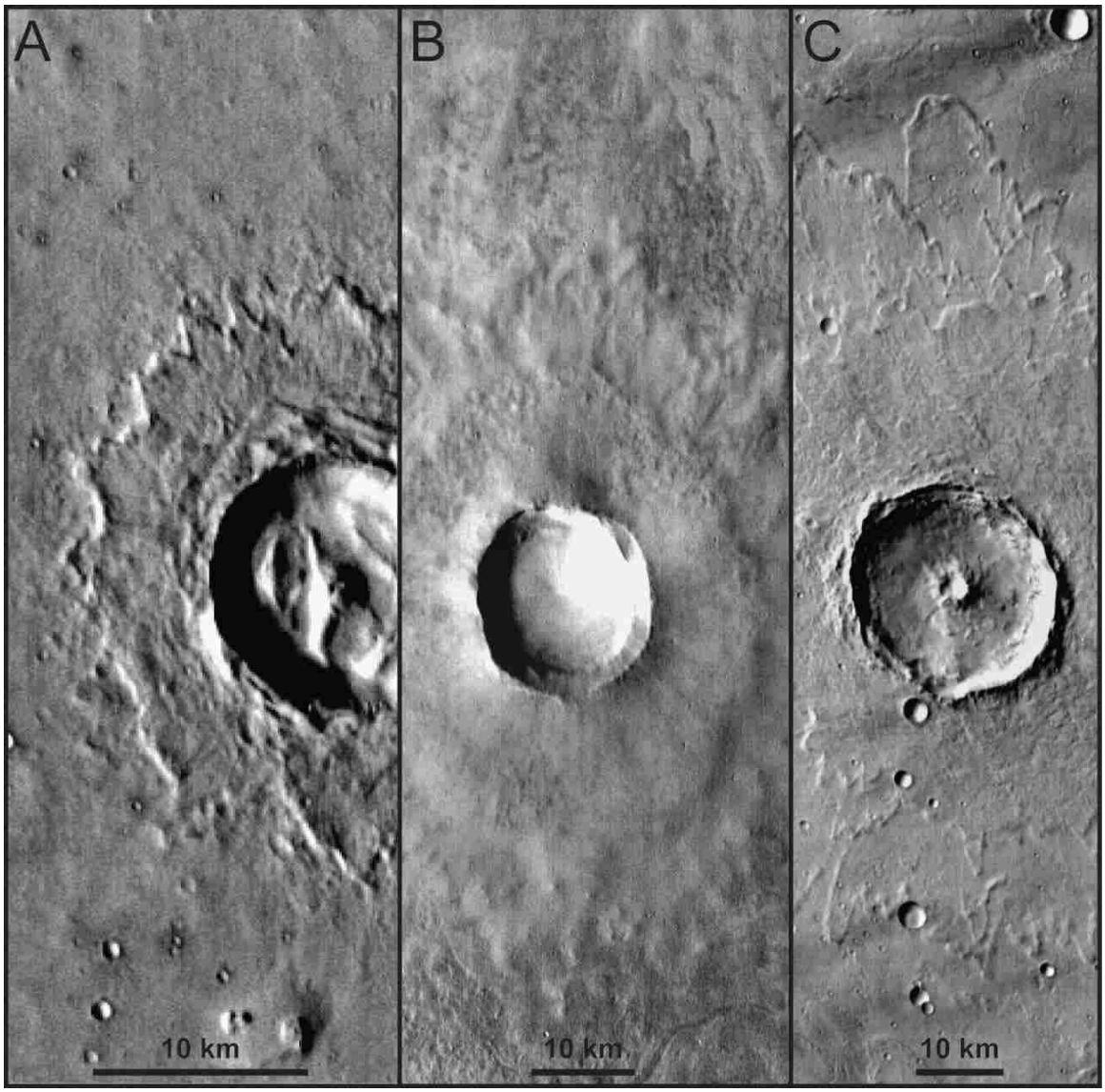

Figure 1. Martian rampart crater morphologies. (A) Single layer ejecta (SLE) crater (THEMIS image I02493005 located near 24ºN 101ºE); (B) Double layer ejecta (DLE) crater (THEMIS image I03350005 located near 49ºN 230.5ºE); and (C) Multiple layer ejecta (MLE) crater (THEMIS image I03218002 located near 6ºN 304ºE). All scale bars are approximate. Adapted from Barlow, 2005.

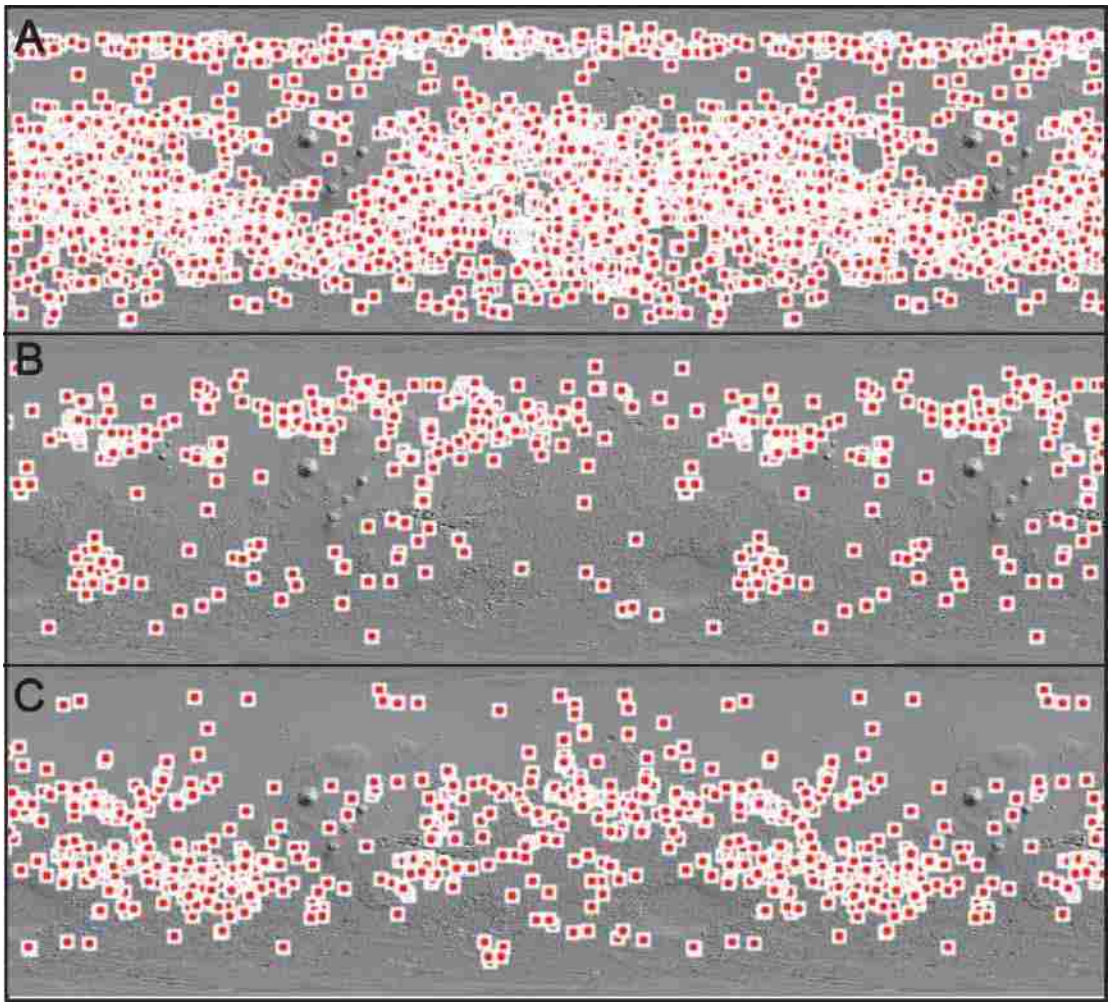

Figure 2. Geographic distribution of layered ejecta morphology for Martian rampart craters. (A) Distribution of single layer ejecta (SLE) craters, (B) Distribution of double layer ejecta (DLE) craters, (C) Distribution of multiple layer ejecta (MLE) craters. Base map is Mars Orbital Laser Altimeter (MOLA) shaded relief map. Each map is centered on 0º longitude and covers the region ±65º latitude. Crater data from Barlow Crater Database version 1 downloaded from USGS Planetary GIS Web Server (PIGWAD). Maps created using jMARS after Barlow (2005).

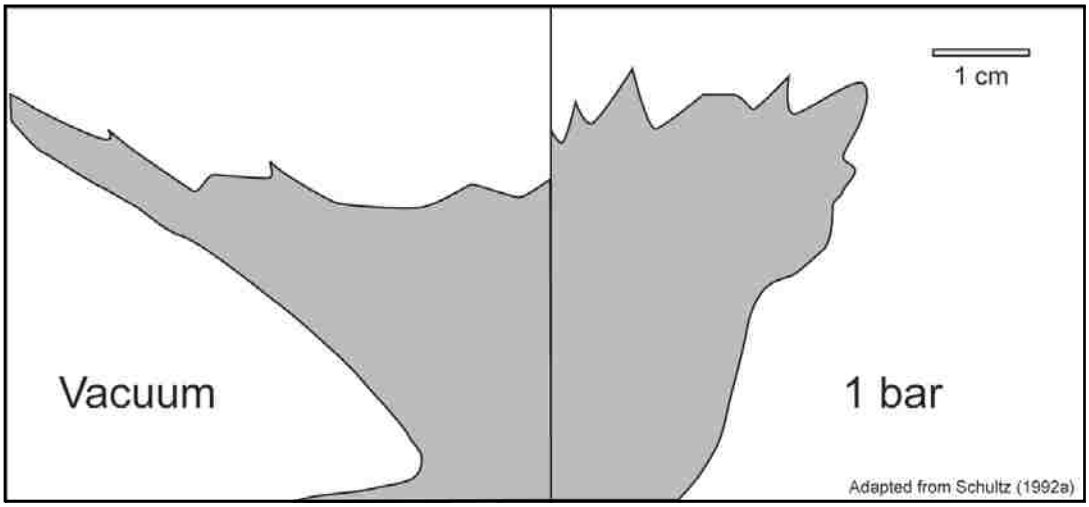

Figure 3. Ejecta curtain profiles under vacuum conditions (left) and 1 bar pressure (right) (Schultz, 1992a). Schultz (1992a) found that fluidized ejecta and a bulging ejecta curtain profile could be produced by increasing the atmospheric pressure or decreasing ejecta particle size.

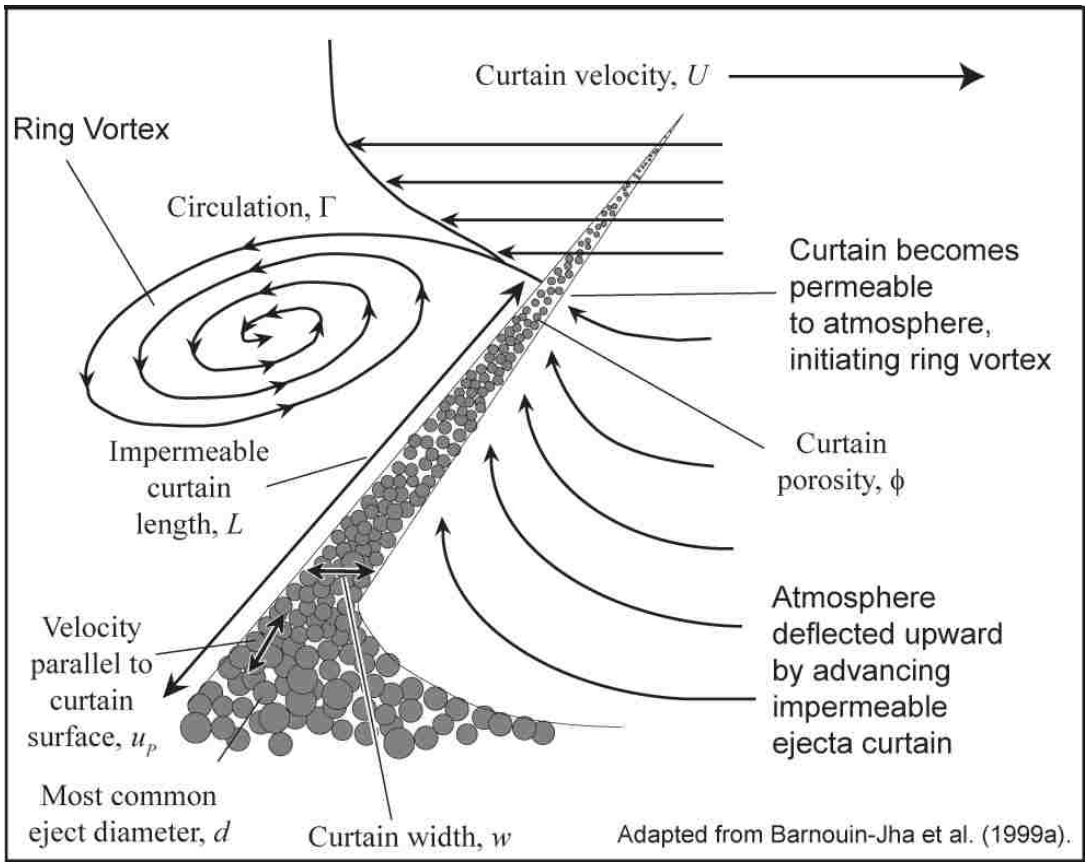

Figure 4. Model of an ejecta curtain advancing through an atmosphere. The model is based on observations at the NASA Ames vertical gun range (Barnouin-Jha et al., 1999a). The lower thicker portion is impermeable to the surrounding atmosphere and redirects the atmosphere around it. The upper more permeable portions allow atmospheric flow through the ejecta curtain, allowing flow separation to generate a vortex ring. Fine-grained ejecta are decelerated out of the semipermeable portions of the ejecta curtain and enter the vortex ring. Adapted from Barnouin-Jha et al., 1999a.

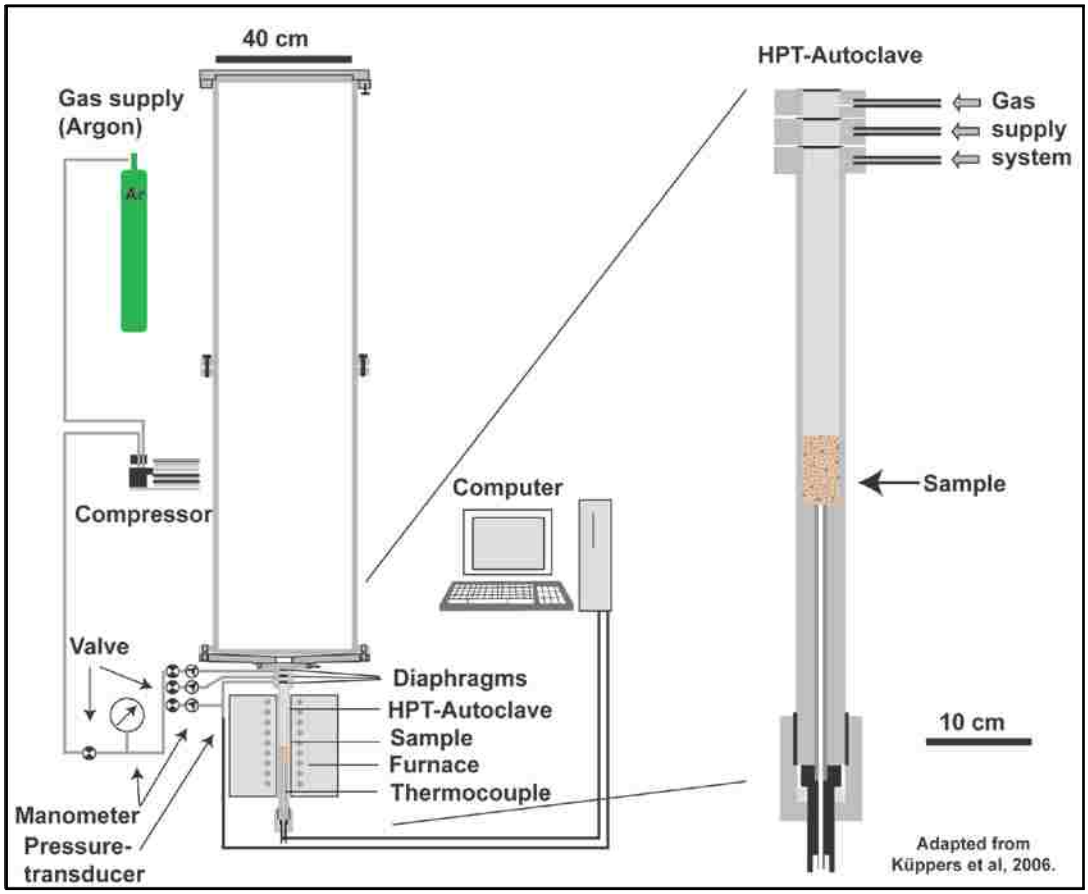

Figure 5. Shock-tube apparatus at the University of Munich Department of Earth and Environmental Science (adapted from Küppers et al., 2006). High pressure and temperature (HPT) autoclave is pressurized with Ar gas and heated by an external furnace. When diaphragms break under high pressure, a release wave propagates down through the sample, fracturing the rock sample parallel to the release wave front and accelerating fragments into the upper chamber.

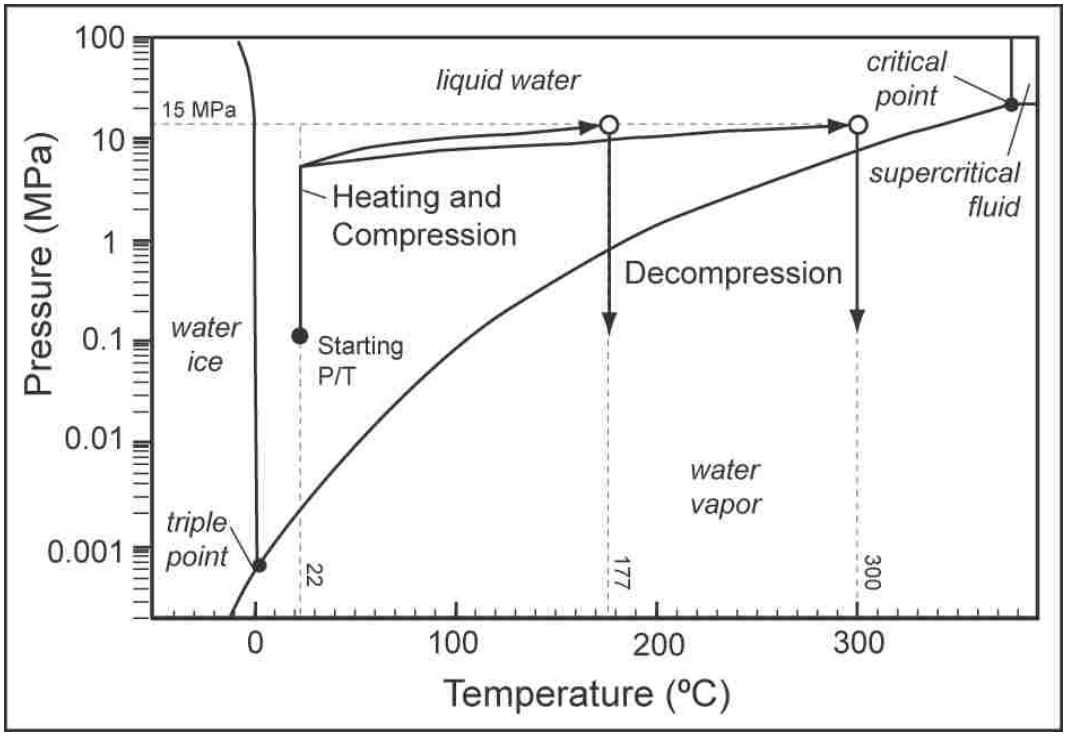

Figure 6. Experimental pressure and temperature conditions. Samples were compressed to about 10 MPa, then compressed and heated to 15 MPa and 177 or 300 ˚C to keep the samples above the vaporization curve for water until instantaneously decompressed.

Table 1. Sample description and experimental conditions.

Sample	Length (mm)	Diameter (mm)	Mass (g)	Calculated Volume (ml)	Measured Volume (ml)	Calculated Density (g/ml)	Measured Density (g/ml)	Open Porosity (ml)	%Open Porosity	Actual Water Added (ml)	%Open Porosity Water	Experimental Temperature (ºC)
102	37.94	24.79	34.7696	18.3196	13.3798	1.8979	2.5987	4.9398	26.96	0	0	177
108	37.32	24.89	32.7240	18.1513	12.5222	1.8028	2.6133	5.6291	31.01	1.7700	31.44	300
109	37.88	24.84	33.4438	18.3571	12.8382	1.8218	2.6050	5.5189	30.06	2.9394	53.26	177
110	37.24	24.82	32.8670	18.0179	12.6004	1.8241	2.6084	5.4175	30.07	0.8679	16.02	177
112	39.20	24.93	34.2736	19.1270	13.1509	1.7919	2.6062	5.9761	31.24	5.3892	90.18	300
113	37.83	24.85	33.5596	18.3550	12.9640	1.8284	2.5887	5.3910	29.37	4.7300	87.74	177
114	38.28	24.85	33.4023	18.5658	12.8223	1.7991	2.6050	5.7435	30.94	3.5365	61.57	177
422	38.11	24.93	36.3973	18.3973	13.8830	1.9574	2.6217	4.7121	25.34	0	0	300
426	37.55	24.88	33.3930	18.3930	12.8442	1.8292	2.5999	5.2567	29.04	1.5780	30.02	177

Table 2. Grain-size distribution results.

Sample	%OPS Water	Temp. (°C)	Median Diameter (ϕ) ($Md\phi$)	Median Diameter (mm) (Md_{mm})	Mean Diameter (ϕ)	Mean Diameter (mm)	Standard Deviation (ϕ)	ϕ_{16}	ϕ_{84}	Graphical Standard Deviation (σ_ϕ)	Skewness	Kurtosis
102	0	177	-1.4265	2.6879	-0.7643	1.6986	1.6519	-2.47	0.44	1.46	1.2575	4.2256
108	31.44	300	-0.0744	1.0529	0.6861	0.6215	1.6245	-1.04	2.50	1.77	0.8417	2.8800
109	53.26	177	-0.2490	1.1884	0.4653	0.7243	1.7046	-1.49	1.95	1.72	0.9993	3.0966
110	16.02	177	-0.5099	1.4239	0.1553	0.8980	1.8705	-1.80	1.72	1.76	0.9312	2.9877
112	90.18	300	-1.1701	2.502	-0.6132	1.5297	2.1373	-3.30	1.46	2.38	0.5375	2.5868
113	87.74	177	-2.3419	5.0696	-1.6358	3.1075	1.9222	-3.60	-0.36	1.62	1.3483	4.5217
114	61.57	177	-1.0947	2.1357	-0.5187	1.4327	1.7145	-2.58	0.39	1.48	1.1631	4.0186
422	0	300	-1.3078	2.4756	-0.6858	1.6086	1.5578	-2.34	0.57	1.46	1.0919	4.0003
426	30.02	177	-0.0203	1.0142	0.7786	0.5829	1.8723	-0.93	2.84	1.88	0.0523	2.8728

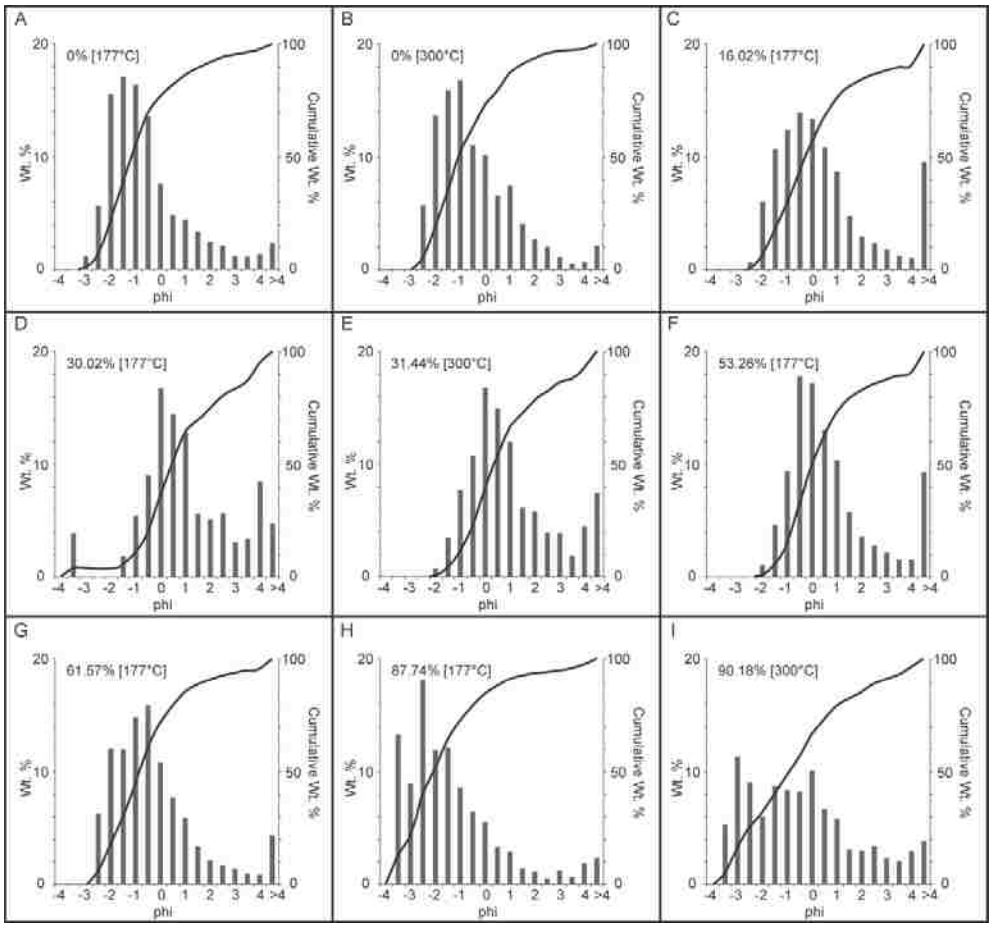

Figure 7. Frequency distributions and cumulative frequency curves for the nine experiments. Percent open pore space (%OPS) water is shown for each sample. Experimental temperature in brackets. All samples were compressed to 15 MPa. Additional information on each sample and experiment can be found in Tables 1 and 2. A=102, B=422, C=110, D=426, E=108, F=109, G=114, H=113, and I=112.

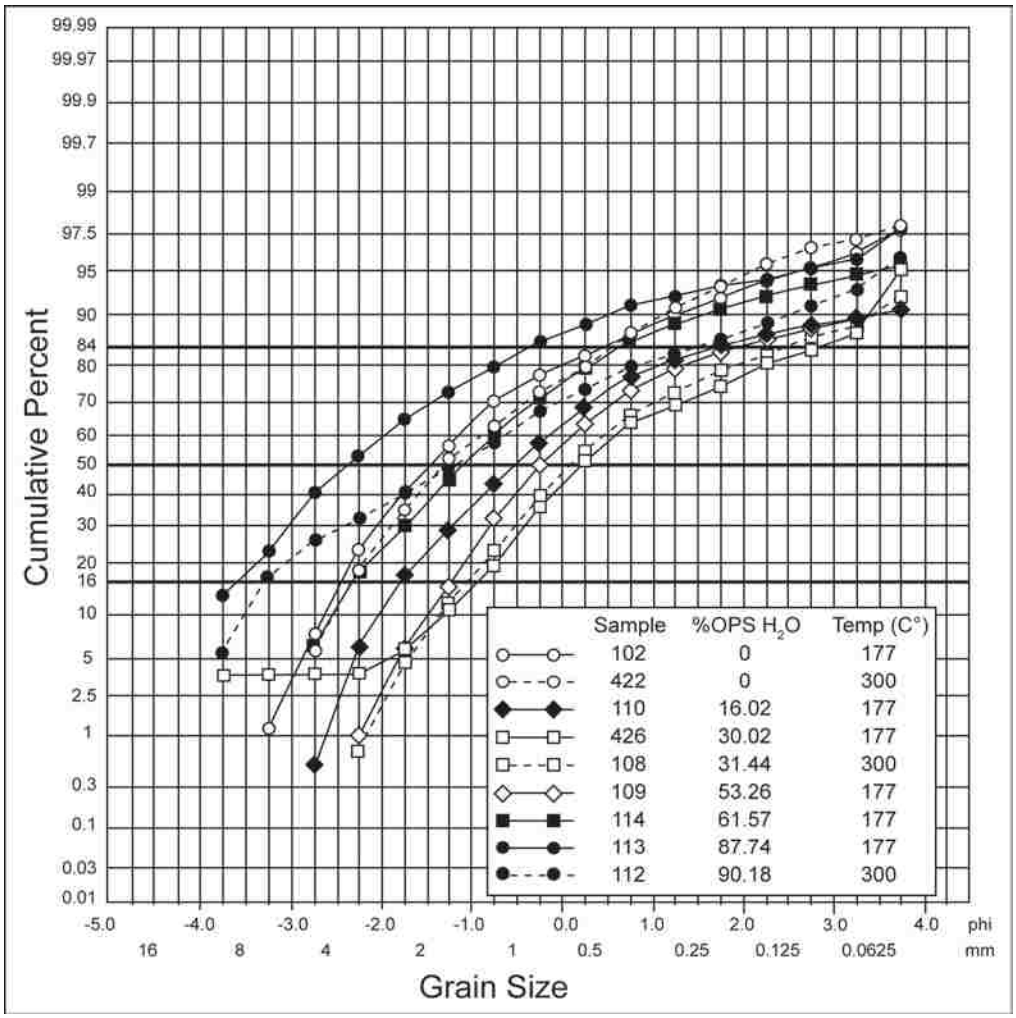

Figure 8. Cumulative frequency distribution for each sample plotted on arithmetic probability paper. Median diameter (Md_ϕ) is the phi-size at which the sample's curve crosses the 50% mark. Graphical standard deviation ($\sigma_\phi = [\phi_{84} - \phi_{16}]/2$) is calculated using the phi values at 16% (ϕ_{16}) and 84% (ϕ_{84}) cumulative percent values.

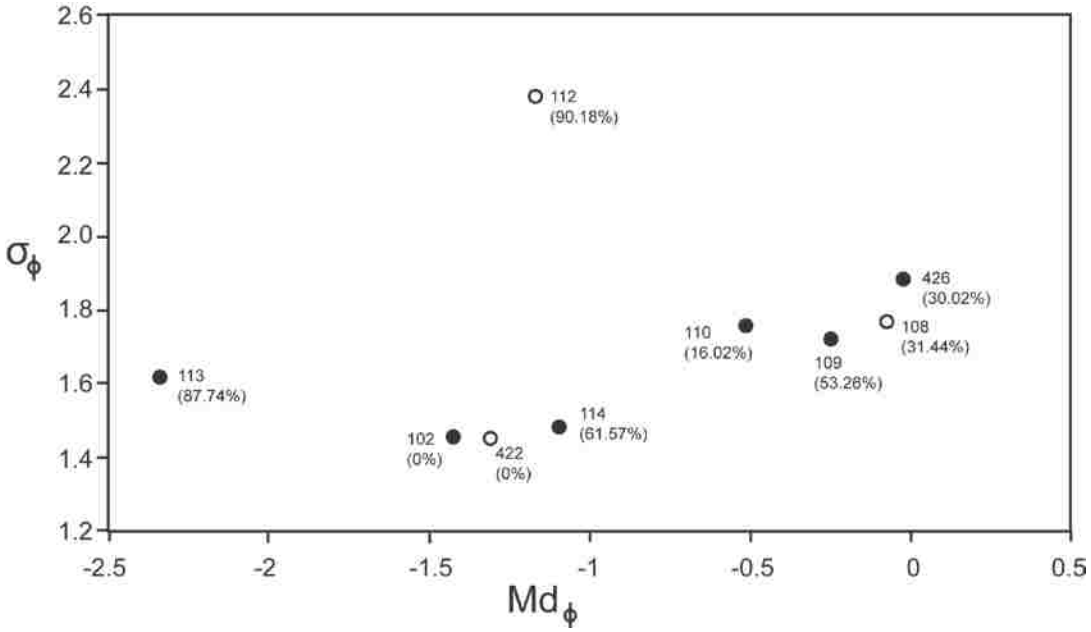

Figure 9. Median diameter (Md_ϕ) vs. graphical standard deviation (σ_ϕ) for the nine experiments. All samples were compressed to 15 MPa. Filled circles = 177 ºC; open circles = 300 ºC. Percent open pore space (%OPS) water shown in parentheses.

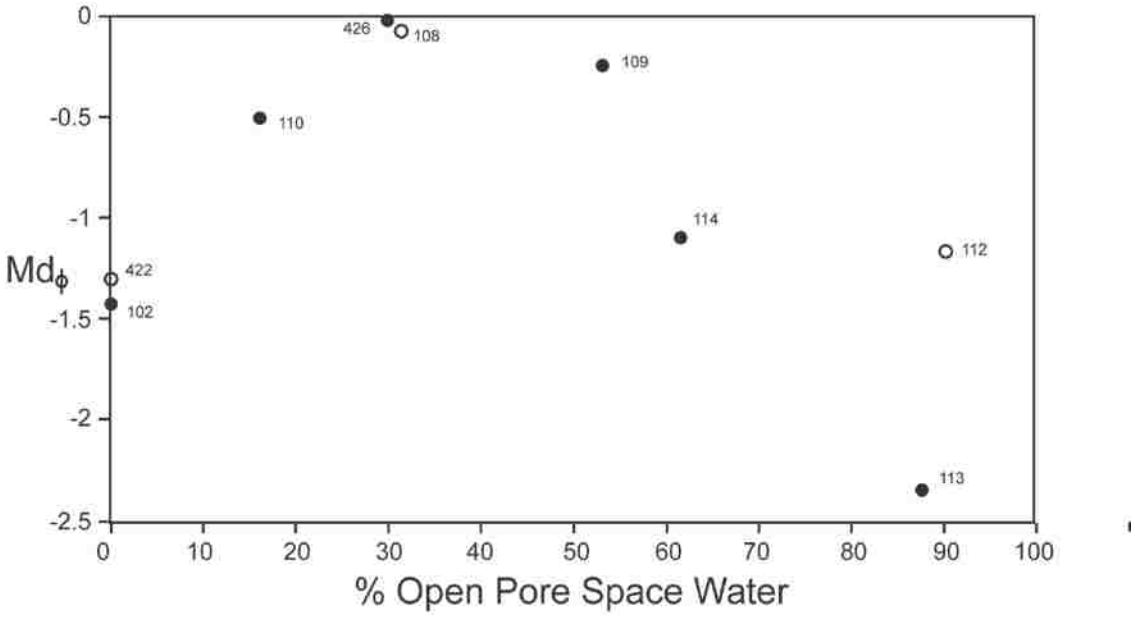

Figure 10. Percent open pore space (%OPS) water vs. median diameter (Mdϕ) for the nine experiments. Filled circles = 177 ºC; open circles = 300 ºC. All samples were compressed to 15 MPa.

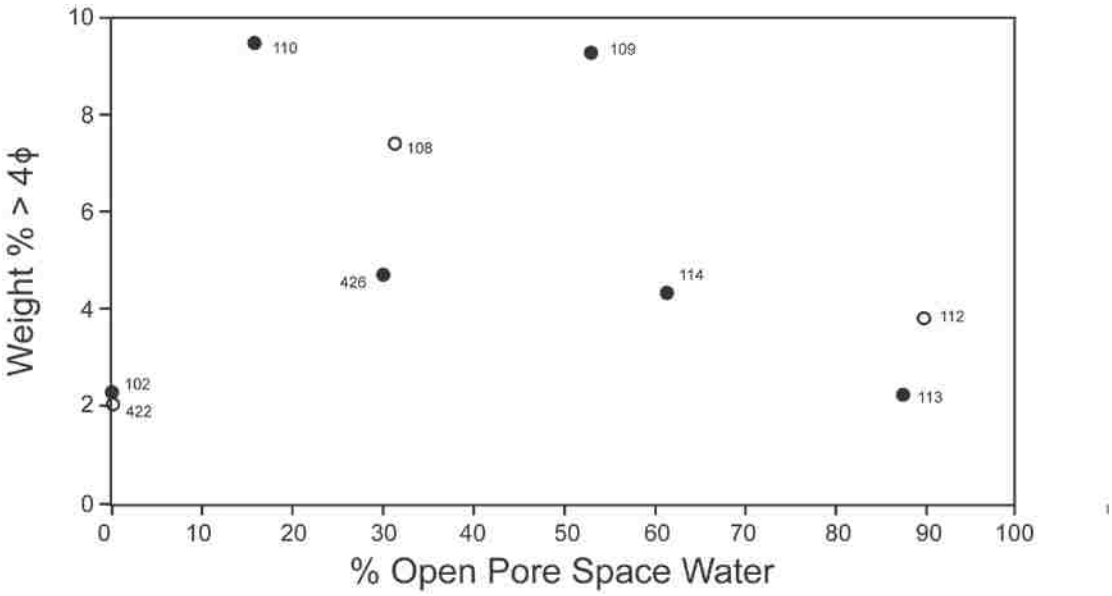

Figure 11. Percent open pore space (%OPS) water vs. weight % fines (>4ϕ) for the nine experiments. Filled circles = 177 ºC; open circles = 300 ºC. All samples were compressed to 15 MPa

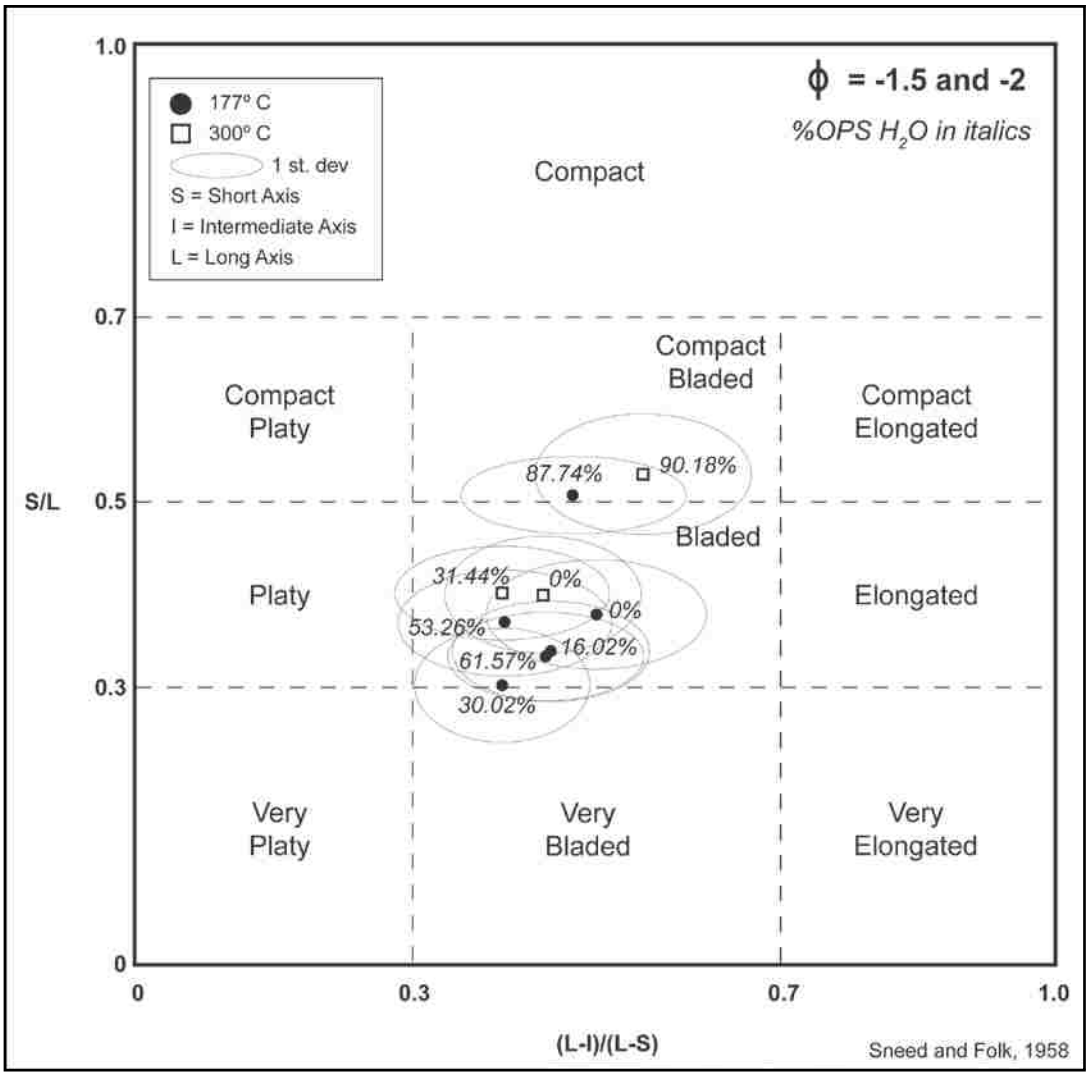

Figure 12. Grain shape for phi sizes -1.5 and -2. plotted against the grain shape fields developed by Sneed and Folk (1958).

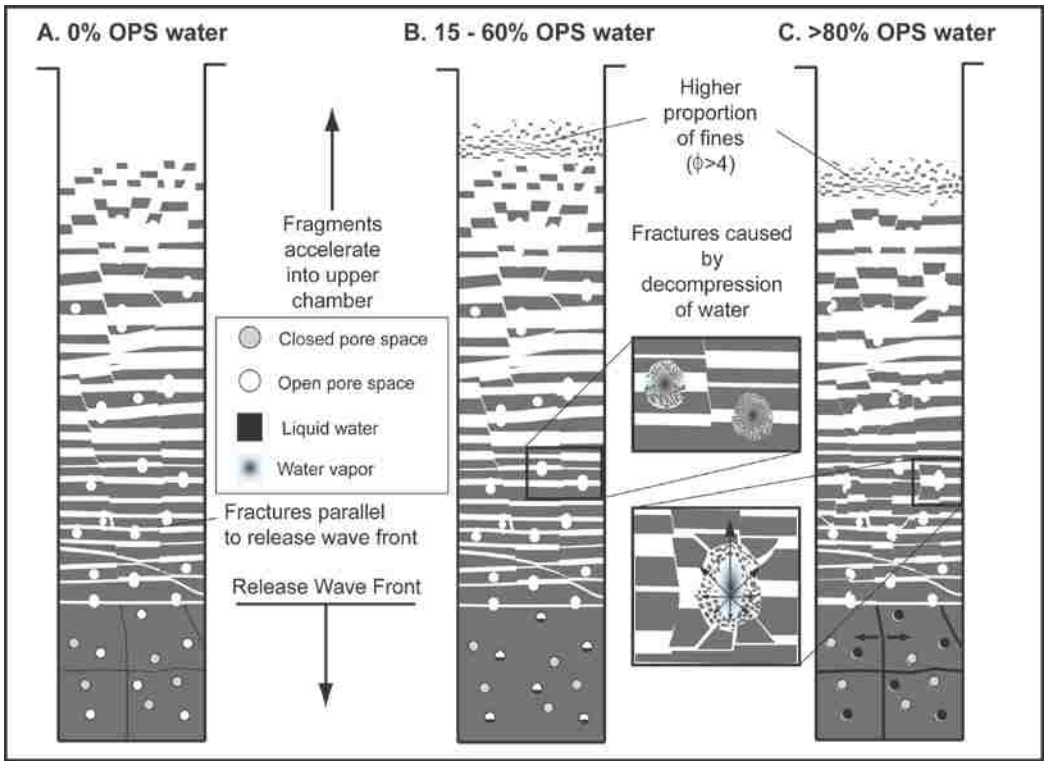

Figure 13. Fragmentation models for (A) 0% open pore space (OPS) water, (B) ~15 - 65% OPS water, and (C) > 80% OPS water.

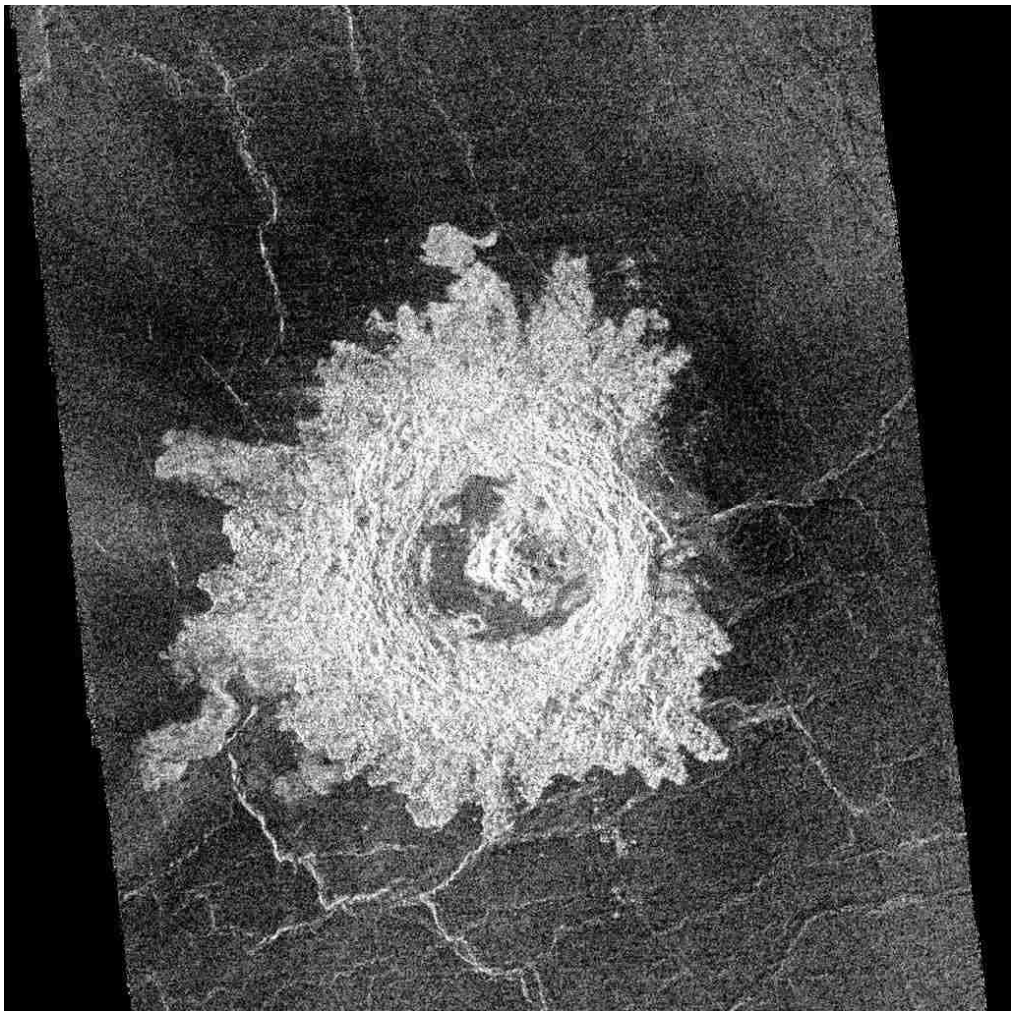

Figure 14. Fluidized ejecta on Venus. Magellan radar image (PIA00470) of Dickison crater in the northeastern Atalanta Region of Venus. The image is ~185 km wide and is centered on 74.6º N, 177.3ºE.

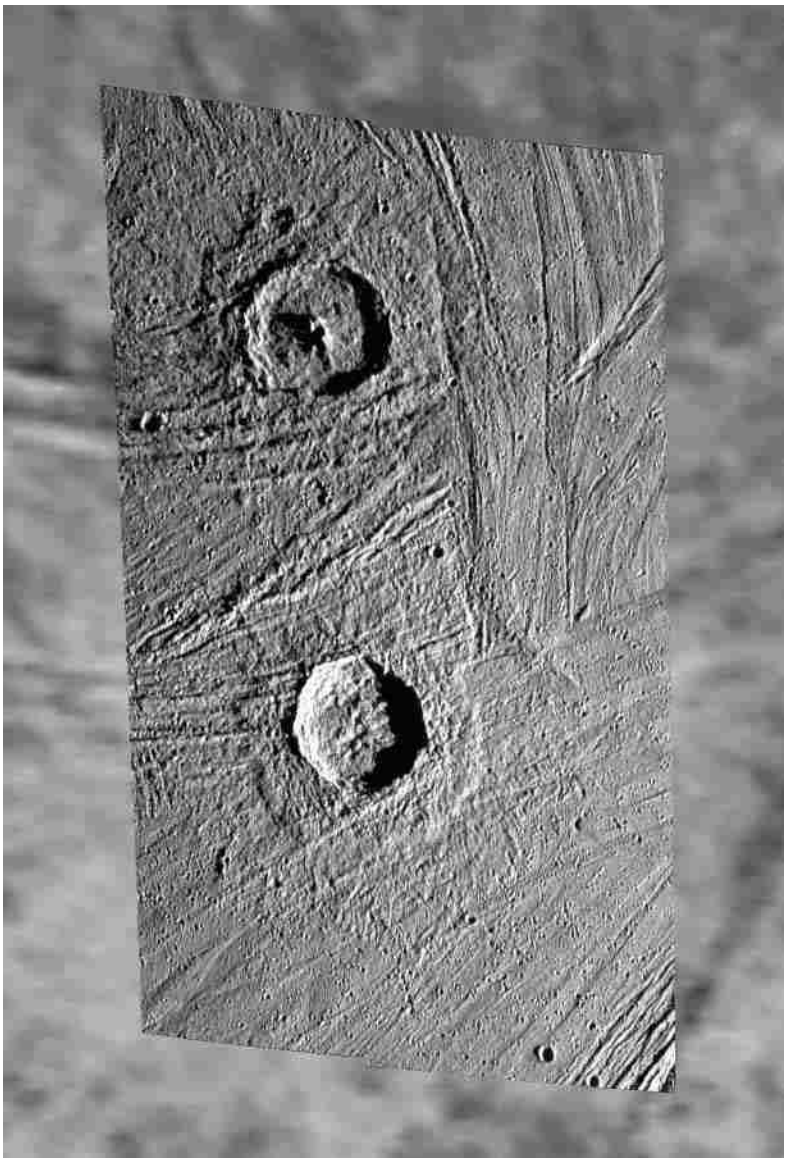

Figure 15. Fluidized ejecta on Ganymede. Galileo Orbiter image (PIA01660) of Gula (top, ~40 km in diameter) and Achelous (bottom, ~35 km in diameter) craters. The image is centered at ~60ºN, 12.5ºW.

CHAPTER THREE

HOW WATER IN OPEN PORE SPACE AFFECTSTHE FRAGMENTATION THRESHOLD OF ROCKS: IMPLICATIONS FOR DOUBLE LAYER EJECTA FORMATION

Abstract

In chapter two, the effects of water vaporization during rapid decompression on rock fragmentation were tested. Those experiments showed that expanding water vapor increases the fragmentation and significantly reduces the median grain size of the target rock. In this chapter, rock fragmentation is measured when water does not cross the vaporization curve. Under these conditions, water within open pore space increases the fragmentation threshold of rocks, shifting the median grain size to larger sizes. This study complements the hybrid model presented in chapter two by suggesting a mechanism for the formation of double-layered ejecta (DLE), a common crater ejecta type on Mars. In this model, the inner layer of DLE is formed when the ejecta curtain contains large blocks at the base and much finer particles toward the top. This size partitioning is caused by relatively high (>75% of open pore space filled with water for a sandstone with 28% open porosity) amounts of water ice in the target that melt during impact cratering. In this situation, the larger blocks fall out of the ejecta curtain first and produce the inner layer. A ring vortex is formed where the ejecta curtain becomes permeable to the atmosphere. This vortex deposits finer grained material behind the advancing ballistic ejecta, generating the outer ejecta layer. At discrete locations near the base of the ejecta curtain, some of the larger blocks extend outside the average curtain width. At these points

Raleigh-Taylor or Kelvin-Helmholtz instabilities (Chandrasekhar, 1981; Boyce et al., 2010) form, punching holes in the curtain and forming scouring jets below the ring vortex. These jets carve out the radial lines in the inner and outer ejecta blanket

Introduction

This section provides a brief summary of Martian rampart craters, fluidized ejecta morphology, and current models for fluidized ejecta formation. A more detailed discussion can be found in chapter one, appendix one, and appendix two.

Martian Rampart Craters

Most Martian impact craters are surrounded by fluidized ejecta (89% of 10,651 cataloged craters ≥5 km diameter; Barlow, 2005) that differ from radial ejecta on the Moon and Mercury (Carr et al, 1977; Barlow, 2005). Barlow (2005) classified three types of fluidized ejecta (Figure 1): (1) single layer ejecta (SLE), (2) double layer ejecta (DLE), and (3) multiple layer ejecta (MLE). Fluidized ejecta hug topography and terminate in a distal rampart about 1.5 to 2 crater radii from the crater rim (Figure 1; Barlow, 2005; Garvin et al., 2000, 2003; Melosh, 1989). Secondary craters are rare within the fluidized ejecta (Barlow, 2003a, 2003b, and 2005) blanket for SLE, DLE, and MLE. Beyond the rampart, secondary craters extend many crater radii beyond the edge of the blanket (Barlow, 2005).

DLE craters have several features which distinguish them from SLE and MLE and may indicate a slightly different emplacement mechanism (Boyce and Mouginis-Mark, 2006; Boyce et al., 2010). DLE craters have two layers with an outer ejecta layer that looks very much like an SLE layer (Boyce and Mouginis-Mark, 2006; Boyce et al.,

2010). The inner layer however, has a more rounded, less sinuous rampart and a convex topographic profile. THEMIS and HiRISE images show that the rampart of the inner DLE layer is made of larger blocks than the outer layer (Boyce and Mouginis-Mark, 2006; Boyce et al., 2010). Another distinctive feature of DLE craters is the presence of radial grooves that extend from the crater rim to the distal rampart of the outer ejecta layer (Barlow, 2005; Boyce and Mouginis-Mark, 2006; Barlow, 2010; Boyce et al., 2010).

Fluidized Ejecta Formation

Barlow (2005) suggested that fluidized ejecta are produced by some combination of the atmospheric model and subsurface volatile model. This dissertation presents a hybrid model in which that atmospheric (Schultz and Gault, 1979; Schultz, 1992a and 1992b; Barnouin-Jha and Schultz, 1998; Barnouin-Jha et al., 1999a, 1999b) and subsurface volatile (Baratoux et al, 2002a and 2002b; Barlow, 2005; Carr et al., 1977; Greeley et al., 1980; Greeley et al., 1982, Mouginis-Mark, 1987; Stewart et al., 2001; Wohletz and Sheridan, 1983) models are two end-members of fluidized ejecta emplacement. Fluidized ejecta on Venus are an example of the purely atmospheric end-member; Ganymede represents the subsurface volatile end-member. The previous chapter proposed that the vaporization of water during the excavation stage of impact cratering increases ejecta fragmentation which results in decreased ejecta sizes. The result is smaller ejecta particles which are able to interact with the thin Martian atmosphere in a manner described by Schultz (1992a and 1992b), Barnouin-Jha and Schultz (1998), and Barnouin-Jha et al. (1999a and 1999b) to produce fluidized ejecta. These results were used to develop a model for the formation of SLE and MLE.

This study looks at the effects of water content on rock fragmentation when the vaporization curve for water is not crossed. Results show that when the vaporization curve is not crossed during decompression (15 MPa, 50 ºC) the fragmentation threshold is increased due to a decrease in open porosity. This is probably true only in situations where the water is confined in open pore space in a rock that has relatively low permeability preventing the liquid water from moving through the rock easily. Because ejection angle is inversely proportional to material strength, this increase in strength may result in larger blocks of ejecta being ejected at lower angles in regions where the vaporization curve is not crossed.

Summary

Boyce and Mouginis-Mark (2006) and Boyce et al., (2010), point to the distinctive morphology of Martian DLE craters as an indication that the process that forms these craters is distinctive from SLE and MLE craters.

According to Boyce et al., (2010) the existence of fluidized ejecta craters on Ganymede suggests that an atmosphere is not required to produce fluidized ejecta. However, the existence of fluidized ejecta on Venus, a planet with a very thick atmosphere and no subsurface volatiles, can be pointed to as evidence that subsurface volatiles are not required to produce fluidized ejecta. It should also be noted that other icy satellites lack fluidized ejecta. This suggests that fluidized ejecta emplacement is a complex process that may not be easily explained by a single mechanism.

Experiments reported in this chapter show that DLE craters form in situations where the target contains a relatively large amount of water and most of the water does not cross the vaporization curve. This situation results in ejecta consisting of more larger

blocks and more fine-grained particles. The increase in larger blocks at the base of the ejecta curtain results in places in the curtain where some larger blocks extend outside the average ejecta curtain width Raleigh-Taylor or Kelvin-Helmholtz instabilities (Chandrasekhar, 1981; Boyce et al., 2010) may form at these locations, creating jets beneath the ring vortex. These jets do not form a vortex ring. They are closer to the ground than the vortex ring and travel behind it, and scour the surface. When the larger blocks fall out of the ejecta curtain, these jets persist behind the ring vortex and continue producing the scouring pattern to the end of the outer DLE layer.

When the vaporization curve is crossed during decompression (15 MPa, 177 ºC or 300 ºC) the grain-size distribution shifts to smaller size with increased water. For the northern Eldorado Mountains sandstone samples, the degree of fragmentation peaked at around 30% OPS H_2O. With increased amounts of water (>~75%) the grain size distribution is similar to control samples where no water is present in the open pore space but is more uniform with a higher proportion of fines and larger blocks and grain shape is blockier. This indicates that the expansion of water during vaporization may be creating fractures perpendicular to the release wave front.

Methods

Using the shock tube apparatus at the University of Munich fragmentation experiments were run on rock-water mixtures. In these experiments, the system does not cross the vaporization curve for water. This section describes the fragmentation methods, sample preparation, sample recovery and sieving, and data analysis.

Fragmentation Methods

The shock tube apparatus at the University of Munich is described in detailed in Alidibirov and Dingwell (1996a). It consists of a lower chamber that can be pressurized up to 40 MPa with Ar gas (Figure 5). This lower chamber, which is at room temperature and pressure, is separated from the upper chamber by a series of metal diaphragms. These diaphragms, made of copper or aluminum, vary in thickness and are inscribed with a ring and cross pattern that cut into the diaphragm at various depths. The lower chamber can be pressurized up to 50 MPa. The combinations of diaphragm material (Cu or Al), thickness, and imprint depth determine the pressure at which the diaphragm will open. When the diaphragm breaks cleanly, a shock wave propagates through the lower chamber as the Ar gas is instantaneously released into the low-pressure, upper chamber. As the release wave travels down through the sample from top to bottom, the sample is unloaded. Fractures are created parallel to the release wave front as it passes through the sample. The fragmented rock particles are accelerated and eject into the upper chamber.

The original goal of these experiments was to heat the rock samples to 177 ºC and achieve a fragmentation pressure of 15 MPa to ensure the rock sample crossed the vaporization curve for water (Figure 16). In order to keep the water in a liquid state, the samples were initially pressurized to about 10 MPa (Figure 16). The furnace surrounding the autoclave was then set to 177 ºC and the autoclave was heated for 15 minutes (Figures 5 and 16). Pressure was increased incrementally approaching 15 MPa to keep the system from crossing the vaporization curve before failure of the diaphragms. After 15 minutes of heating, additional Ar gas was added to the lower chamber to initiate failure of the diaphragms. Occasionally, the diaphragms failed before this waiting period

was completed. But in all experiments, the system decompressed at about 15 MPa. As will be discussed in the results section of this chapter, it was later discovered that the crucible and rock sample did not reach 177 ºC. They only reached 50 ºC. Consequently, the rock samples did not cross the vaporization curve for water during shock decompression.

Sample Preparation

The purpose of this investigation is to measure the fragmentation behavior of water-bearing rocks during the rapid decompression associated with crater excavation. Carrying out these experiments requires a rock that is as close as reasonably possible to a generic regolith composition and structure for Mars. The Martian surface is covered by sedimentary deposits derived from basalt and andesite (Bandfield et al. 2000; Barlow, 2008; Malin and Edgett, 2000a and 2000b). A volcaniclastic rock from the northern Eldorado Mountains of southern Nevada, U.S.A. (Anderson, 1971) was used in these experiments. This is a thinly bedded (1 – 3 mm) volcaniclastic sandstone composed of olivine, quartz, and occasional small (<3 mm) rock and pumice fragments derived from mid-Miocene Patsy Mine basalt, dacite, and rhyolite. This rock was chosen for two reasons. First, it is composed of eroded volcanic rocks similar to Martian regolith. Second, the rock's uniform structure and composition make it ideal for use in these experiments where the physical property of the rock must be consistent for each trial.

The rock was cut into 2.5-cm-diameter, 4-cm-long cylindrical samples. The samples were placed in a 190 °C oven overnight to drive off water from the open pore space. After cooling in a desiccator, each sample was weighed on an electronic balance. Masses were recorded in grams. Digital calipers were used to measure length along the

axis of the cylinder. Two diameter measurements were made, one at each end of the cylinder (about 0.5 to 1 cm from the end). The average of these two diameters was used to calculate the sample volume (V_{calc}). Each sample was placed in a helium pycnometer to determine the volume the sample occupied minus open pore space (V_{hc}). The percent of open porosity ([[V_{calc} - V_{hc}]/ V_{calc}] x 100%) was calculated. The sandstone has an average calculated density of 1.8958 g/cm^2 and average measured density of 2.1627 g/cm^2, with standard deviations of 0.005 and 0.0053 respectively. The average open porosity of the samples is 27.4450%, with a standard deviation of 3.3277.

Prior to the experiment, each rock sample was placed in a brass crucible cylinder open on one end with an interior diameter slightly smaller than the rock sample. This tight fit facilitates fracture of the sample during decompression by preventing the entire rock cylinder from ejecting into the upper chamber upon decompression. This was accomplished by placing the rock sample on the open end of the cylinder and heating the brass cylinder with a hot air gun causing it to expand slightly while pressing the rock into the cylinder using a hydraulic press. Each sample in its crucible was stored in an airtight container until the experiment was conducted (no more than 24 hours). Table 3 contains descriptions of the physical properties measured for each sample.

Methods for Adding Water to the Sample

To test the effects of water content on rock fragmentation, varying amounts of water were added to each sample. In the previous chapter, percent open pore space (%OPS) water contents of approximately 0%, 15%, 30%, 50%, 70%, and 100% OPS water were tested. In order to fill in gaps between previously run %OPS values, %OPS

values of 15.30, 45.84, 59.41, 74.61, and 92.32 were tested in these experiments (Table 3).

To determine the amount of water to add to each sample, (1) the volume (ml) of open pore space for each sample was calculated and (2) the volume (ml) of the target %OPS water was calculated. The calculated volume of distilled water was added to the top of the rock sample in the crucible. The sample was placed in a vacuum to draw the water as evenly as possible through the sample. After a few hours the sample was inspected to determine whether the top of the rock sample and the bottom (visible through a small hole) appeared to have about the same degree of wetness. The sample was weighed to determine if it still had the correct amount of water. More water was added if necessary. The sample was iteratively inspected and weighed, adding water as necessary, until the target %OPS water closely approximated. The sample was weighed immediately prior to placement in the lower chamber of the shock tube apparatus and the actual %OPS water was recorded (Table 3).

Sieving Methods

After each experiment, a high-pressure water hose was used to flush the upper tank. The rock fragments were collected, dried, and sieved between sieve sizes -4 and 4 phi at 0.5-phi intervals. The contents of each sieve were weighed on an electronic balance and the weight percent of each sieve interval was calculated.

A grain size distribution curve was plotted on an arithmetic probability grid for each sample using GRANPLOT, a Microsoft Excel Spreadsheet developed by Balsillie et al. (2002). Inman (1952) parameters including (1) median diameter ($Md_\phi = \phi_{50}$), the phi-size where the cumulative distribution curve crosses the 50% mark; (2) graphical standard

deviation ($\sigma_\phi = [\phi_{84} - \phi_{16}]/2$), which is a measure of sorting; (3) first order skewness ($\alpha_\phi = [((\phi_{84} + \phi_{16}) - Md_\phi]/\sigma_\phi$), which is a measure of asymmetry of the distribution; and (4) kurtosis, a measure of the peakedness of the distribution, was also calculated.

Results

Grain size distribution results are summarized in Table 4 and Figures 17 and 18. Looking at the samples from lowest to highest %OPS H_2O, no clear trend in median diameter is immediately apparent (Table 4, Figures 17 and 18). Sample 416 (15.30% OPS H_2O) has a median diameter of -0.47ϕ and graphical standard deviation of 1.41ϕ. Sample 417 (45.85% OPS H_2O) has a median diameter of -1.32ϕ and graphical standard deviation of 1.43ϕ. Sample 104 (59.41% OPS H_2O) has a median diameter of -1.33ϕ and graphical standard deviation of 1.27ϕ. Sample 103 (74.61% OPS H_2O) has a median diameter of -3.67ϕ and graphical standard deviation of 1.93ϕ. Sample 105 (92.32% OPS H_2O) has a median diameter of -3.44ϕ and graphical standard deviation of 1.81ϕ.

Frequency distribution and cumulative frequency distribution plots are shown in Figure 17. Samples 416, 417, and 104 have slightly right skewed frequency distributions. Although there is a difference of almost 15% OPS H_2O, their frequency distributions and cumulative frequency distribution curves of samples 104 (59.41% OPS H_2O) and 417 (45.85% OPS H_2O) are very similar. Samples 103 and 105 had the highest %OPS H_2O with 74.61% and 92.32%, respectively. These samples also have very different frequency distribution and cumulative frequency curves from the other samples. The large spike in the frequency distribution for these two samples in the -6 phi column represents a large piece of unfragmented rock sample that remained in the crucible.

The dramatic differences between the two groups of samples are also evident in the arithmetic probability plot (Figure 18). Here the curves for samples 103 and 105 do not extend below the 84 percentile due to the large percentage of the sample remaining unfragmented and unejected in the crucible. The other three samples (104, 416, and 417) did fragment completely. However, their arithmetic probability plots do not fit fragmentation patterns found in chapter one where a steel crucible was used.

In the previous chapter, control samples (no water added) had a median diameter of about -1.3 to -1.4 phi. Added water increased the degree of fragmentation as measured by a decrease in median diameter. This shift toward smaller particles peaked at around 30% OPS H_2O where the median diameter ranged from about -0.02 and -0.07 phi. Grain size increased with increased % OPS H_2O above about 30%. Experiments with about 80% OPS H_2O or more yielded a grain size distribution with more fines but with median diameters similar to control samples. These experiments also had blockier grain shape believed to result from water vaporization creating fractures perpendicular to the release wave front.

The differences in experimental results compared to the previous study indicate that the water did not vaporize during these experiments when a brass crucible was used. To confirm this, the temperature of the sample was measured for a steel and brass crucible. While the sample in the steel crucible reached the target temperature of 177 ºC, the samples in the brass crucible only reached 50 ºC. This means that the samples in the brass crucible did not cross the vaporization curve for water during shock decompression from 15MPa (Figure 16).

It was previously noted that no clear pattern could be observed between median grain size and % OPS H_2O. However, when the effect of the added water on the sample's open pore space (wet % open porosity) is considered, a pattern emerges (Table 3, Figures 17 and 18). Sample 103 (28.92% dry open porosity; 7.34% wet open porosity), with the highest %wet open porosity, has the smallest median diameter ejecta particles. Samples 104 (30.48% dry open porosity; 12.37% wet open porosity) and 417 Sample 417 (21.91% dry open porosity; 11.86% wet open porosity) have very different % OPS H_2O (59.31% for sample 104, 45.85% for sample 417), but very similar % wet open porosities (~12%). They also have similar frequency distributions, cumulative frequency distributions, median diameters (-1.33ϕ for sample 104, -1.32ϕ for sample 417), and graphical standard deviations (1.27ϕ for sample 104, 1.43ϕ for sample 417) (Table 4, Figures 17 and 18). Samples 103 and 105 with %wet open porosities of 7.34% and 2.27%, respectively, did not completely fragment.

Küppers et al. (2006) plotted rock fragmentation threshold as a function of open porosity (vol. %)(Figure 19). They found that open porosity is inversely proportional to fragmentation threshold. The average dry sample of the NEMSS sandstone used in this study has a %dry open porosity of about 28%. The average NEMSS sample is plotted on Figure 19 at the experimental pressure of 15 MPa that is well above the 5 MPa fragmentation threshold for this rock. When the %wet open porosities of the samples are plotted (Figure 19), samples 103 and 104 cross the range of data obtained by Küppers et al. (2006) indicating these samples are not reaching their fragmentation threshold at 15 MPa and may be the reason much of the sample was left in the crucible.

However, not all of samples 103 and 104 were left in the crucible. Portions of the sample did fragment and eject into the upper chamber. This may be because the addition of Ar gas at the top of the lower chamber is compressing the rock sample and water causing the water to concentrate at the bottom of the crucible, creating a gradient of % OPS H_2O, %wet open porosity, and fragmentation threshold (Figure 20).

Discussion

The goal of this work is to provide a model for fluidized ejecta formation about DLE craters. In chapter two, a model for the formation of SLE and MLE was presented. The original objective of the experiments in this chapter was to provide more trials and to fill in the range of %OPS water tested in chapter two. Fortuitous circumstances provided results that allowed the development of a model for DLE formation.

Grain size distribution results are very different from results obtained in the previous study (Chapter Two), indicating the vaporization curve for water was not crossed during decompression. Temperature measurements of the steel and brass crucibles confirmed this. Although the target temperature was not reached in these experiments, some interesting information was revealed about rock fragmentation of rock-water mixtures when the vaporization curve is not crossed. In this situation, the grain size distribution of ejecta is shifted toward larger sizes. This new information is the basis for new model for the formation of DLE in which the ejecta curtain has a more bimodal or uniform distribution that facilitates deposition of a thicker inner ejecta layer and a thinner outer ejecta layer composed of finer ejecta.

These experiments revealed that, when water remains in liquid form during shock decompression, increased amounts of water result in an overall increase in the median diameter of the ejecta particles when compared with the control samples in the previous chapter. In addition, when the vaporization curve for water is not crossed, water in open pore space increases the fragmentation threshold of the rock-water mixture. Because ejection angle is inversely proportional to target strength, the rock-water mixture may have lower than expected ejection angles.

In the previous chapter, a hybrid model of fluidized ejecta formation was presented for SLE and MLE. In that model, water vaporization during the excavation stage of impact cratering increases the degree of fragmentation of ejecta resulting in ejecta particles that are small enough to interact with the thin Martian atmosphere and be deposited in fluidized manner by a ring vortex trailing behind the advancing ejecta curtain (Schultz and Gault, 1979a and 1979b; Schultz, 1992a and 1992b; Barnouin-Jha and Schultz, 1996; Barnouin-Jha et al., 1999a and 1999b) (Figure 4).

This study revealed that, when the vaporization curve for water is not crossed, water within open pore space increases the fragmentation threshold of rocks, shifting the median grain size to larger sizes. If the amount of water within open pore space is sufficiently large and the vaporization curve is not crossed, the ejecta may contain very large blocks. These observations are the basis for a new model for the formation of DLE outlined below.

The inner layer of double-layered ejecta forms when there are very large blocks at the base of the ejecta curtain and much finer particles toward the top. Results from the experiments in this study and the previous chapter indicate that this type of grain size

distribution may be obtained with relatively high amounts of water within the open pore space (>~75% for a rock with 28% vol. open porosity), regardless of whether the vaporization curve is crossed. Larger blocks fall out first and produce the inner ejecta layer (Figure 21). A ring vortex is still formed where the ejecta curtain becomes permeable to the atmosphere. This vortex deposits finer grained material behind the advancing ballistic ejecta and deposits the outer layer. At discrete locations within the ejecta curtain, some of the larger blocks extend outside the average curtain width. At these points Raleigh-Taylor or Kelvin-Helmholtz instabilities (Chandrasekhar, 1981; Boyce et al., 2010) form, punching holes in the curtain and forming scouring jets below the ring vortex (Figure 21). These jets carve out the radial lines in the inner and outer ejecta blanket.

According to Barnouin-Jha and Schultz (1999a), when these large blocks of ejecta are located in regions of the curtain where their diameter exceeds the thickness of the curtain, the atmosphere impinging on the advancing curtain will deflect locally around these protruding rocks. This deflected atmosphere travels at a greater velocity relative to the impinging atmosphere and may punch holes through the curtain around the protruding rocks. Jets produced by this process most likely occur in the regions where the curtain is thinnest. However, these jets could form anywhere such protruding rocks exist. In the proposed model for DLE formation, large blocks are added to the ejecta during impact into a target containing relatively high amounts of water that does not vaporize during decompression. These larger blocks are concentrated at the base of the curtain. In some places, they may extend outside the average curtain width. Raleigh-Taylor or Kelvin-Helmholtz instabilities (Chandrasekhar, 1981; Boyce et al., 2010) develop at discrete

locations below the ring vortex forming jets that carve out radial grooves extending from the crater rim, across the inner ejecta layer to the end of the distal rampart of the outer ejecta layer.

Conclusions

This study deals with the effects of water within open pore space on rock fragmentation when the vaporization curve for water is not crossed. Results from these experiments indicate that, when the vaporization curve for water is not crossed, water within open pore space increases the fragmentation threshold of rocks, shifting the median grain size to larger sizes. This information is used to add a mechanism for the formation of DLE to the hybrid model presented in chapter two. In the expanded model, the inner layer of DLE is formed when there are very large ejecta blocks at the base of the curtain and much finer particles toward the top. In this situation, the larger blocks fall out first and produce the inner ejecta layer. A ring vortex is still formed where the ejecta curtain becomes permeable to the atmosphere. This vortex deposits finer grained material behind the advancing ballistic ejecta and deposits the outer layer. At discrete locations within the ejecta curtain, some of the larger blocks extend outside the average curtain width. At these points Raleigh-Taylor or Kelvin-Helmholtz instabilities (Chandrasekhar, 1981; Boyce et al., 2010) form, punching holes in the curtain and forming scouring jets below the ring vortex. These jets carve out the radial lines in the inner and outer ejecta blanket. The grain size distribution necessary to create this dynamic in the ejecta curtain is caused by impact into a water ice-bearing target where ice melts but does not vaporize during the excavation stage. In this model, the grain-size distribution necessary for DLE

is produced by impacts into water ice or rock-ice mixtures with high proportions of water ice. This is consistent with the presence of DLE on Ganymede and at high latitudes on Mars.

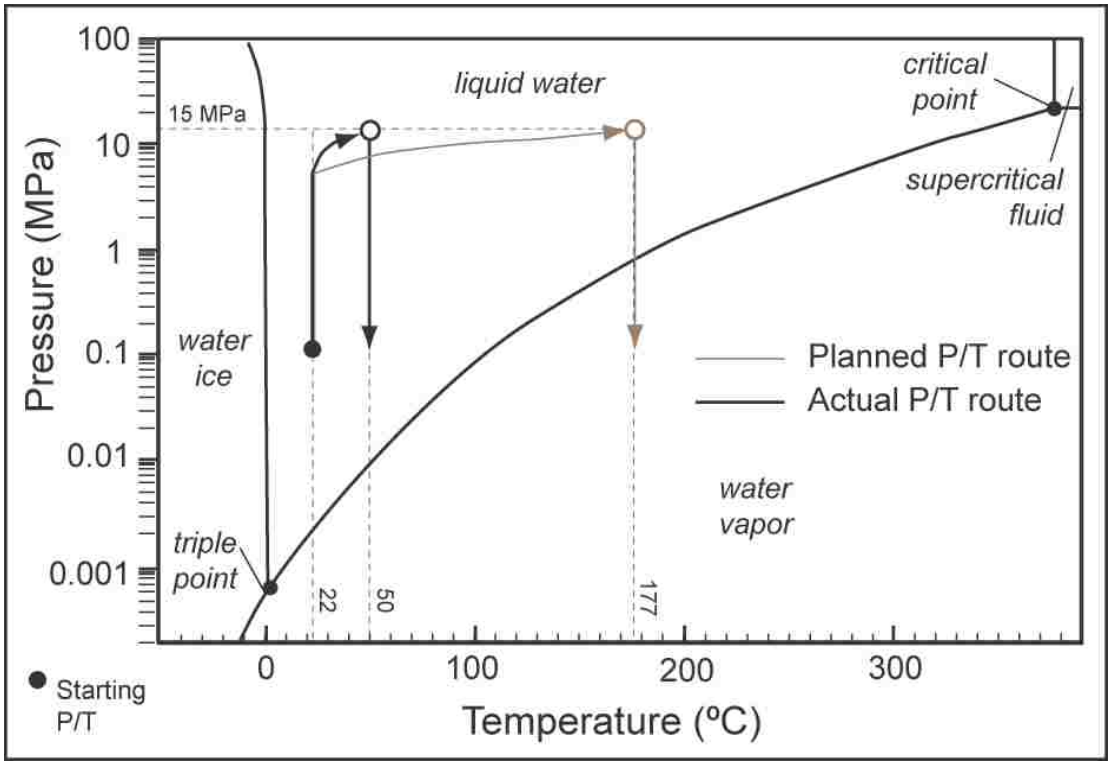

Figure 16. Planned and actual pressure/temperature path for decompression experiments using a brass crucible.

Table 3. Sample description and experimental conditions. Experiments were conducted using a brass crucible at ~50 ºC and 15 MPa.

Sample	Length (mm)	Diameter (mm)	Mass (g)	Calculated Volume (ml)	Measured Volume (ml)	Calculated Density (g/ml)	Measured Density (g/ml)	Open Porosity (ml)	%Open Porosity	Actual Water Added (ml)	%Open Porosity Water	Effective %open pore space with added water
103	37.90	24.84	33.9637	18.3594	13.0507	1.8499	2.6025	5.3087	28.9153	3.9609	74.61	7.34
104	38.60	24.84	34.0057	18.7060	13.0047	1.8126	2.6149	5.7013	30.4784	3.3870	59.41	12.37
105	37.28	24.83	33.0748	18.0517	12.7257	1.8324	2.5993	5.3260	29.5043	4.9170	92.32	2.27
416	38.32	24.79	36.4605	18.4583	13.8418	1.9753	2.6341	4.6165	25.0105	0.7061	15.30	21.19
417	38.47	24.76	38.1455	18.5231	14.4645	2.0593	2.6372	4.0586	21.9110	1.8610	45.85	11.86

Table 4. Grain-size distribution results. Experiments were conducted using a brass crucible at ~50 ºC and 15MPa.

Sample	Effective %open pore space with added water	Median Diameter (ϕ) ($Md\phi$)	Median Diameter (mm) (Md_{mm})	Mean Diameter (ϕ)	Mean Diameter (mm)	Standard Deviation (ϕ)	ϕ_{16}	ϕ_{84}	Graphical Standard Deviation (σ_ϕ)	Skewness	Kurtosis
103	7.34	-3.6678	12.709	-5.4836	44.7422	1.9354	-7.39	-3.54	1.925	22.860	6.983
104	12.37	-1.3312	2.5161	-0.6908	1.6142	1.6517	-2.25	0.28	1.265	1.535	5.124
105	2.27	-3.4439	10.8821	-5.6818	51.3339	1.8390	-7.51	-3.89	1.810	2.972	10.379
416	21.19	-0.4728	1.3878	0.0035	0.9976	1.5262	-1.70	1.12	1.410	0.765	3.216
417	11.86	-1.3226	2.5011	-0.6208	1.5377	1.6169	-2.25	0.59	1.429	1.348	4.254

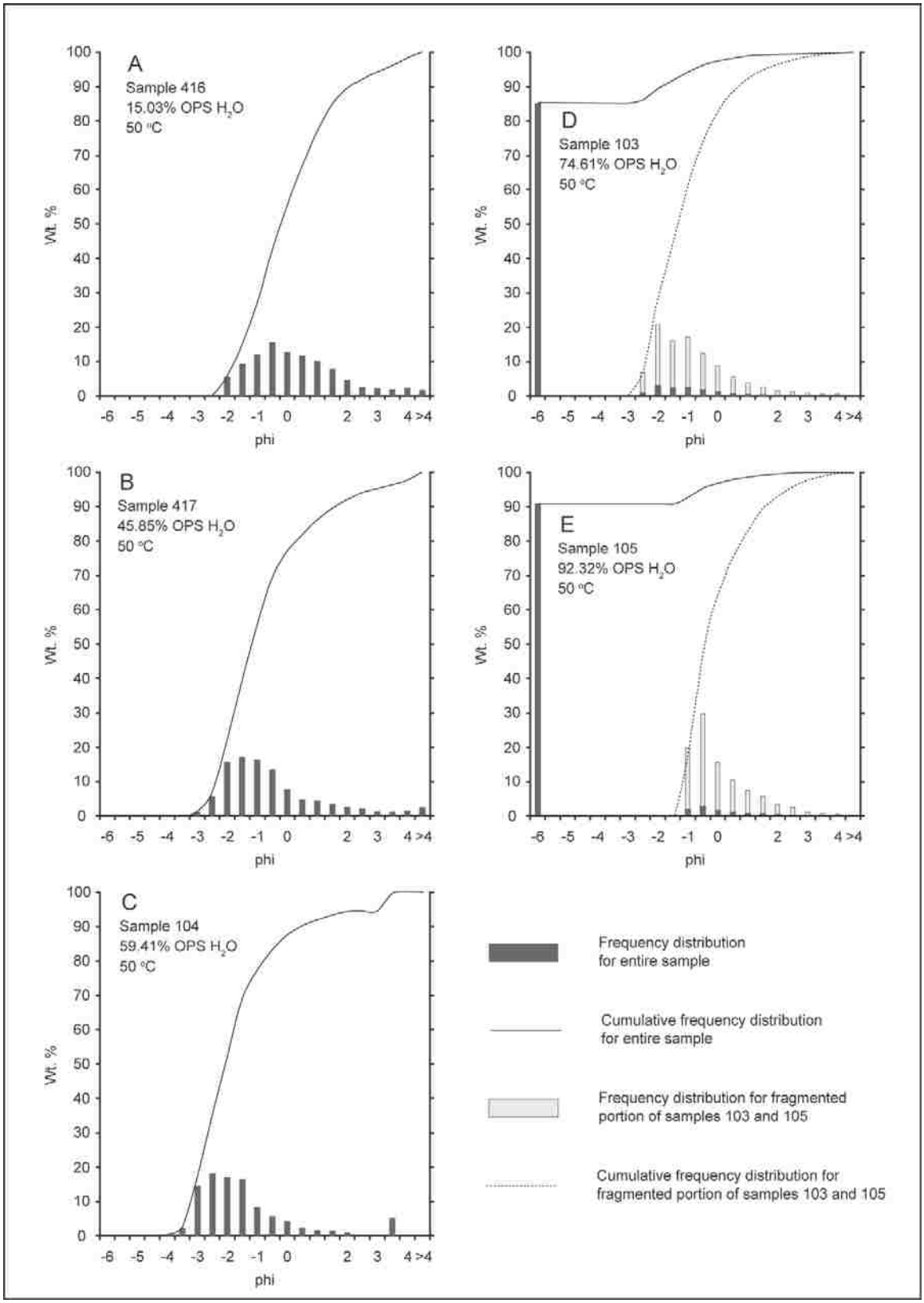

Figure 17. Frequency and cumulative frequency distribution curves for decompression experiments conducted with a brass crucible at ~50 ºC and 15MPa.

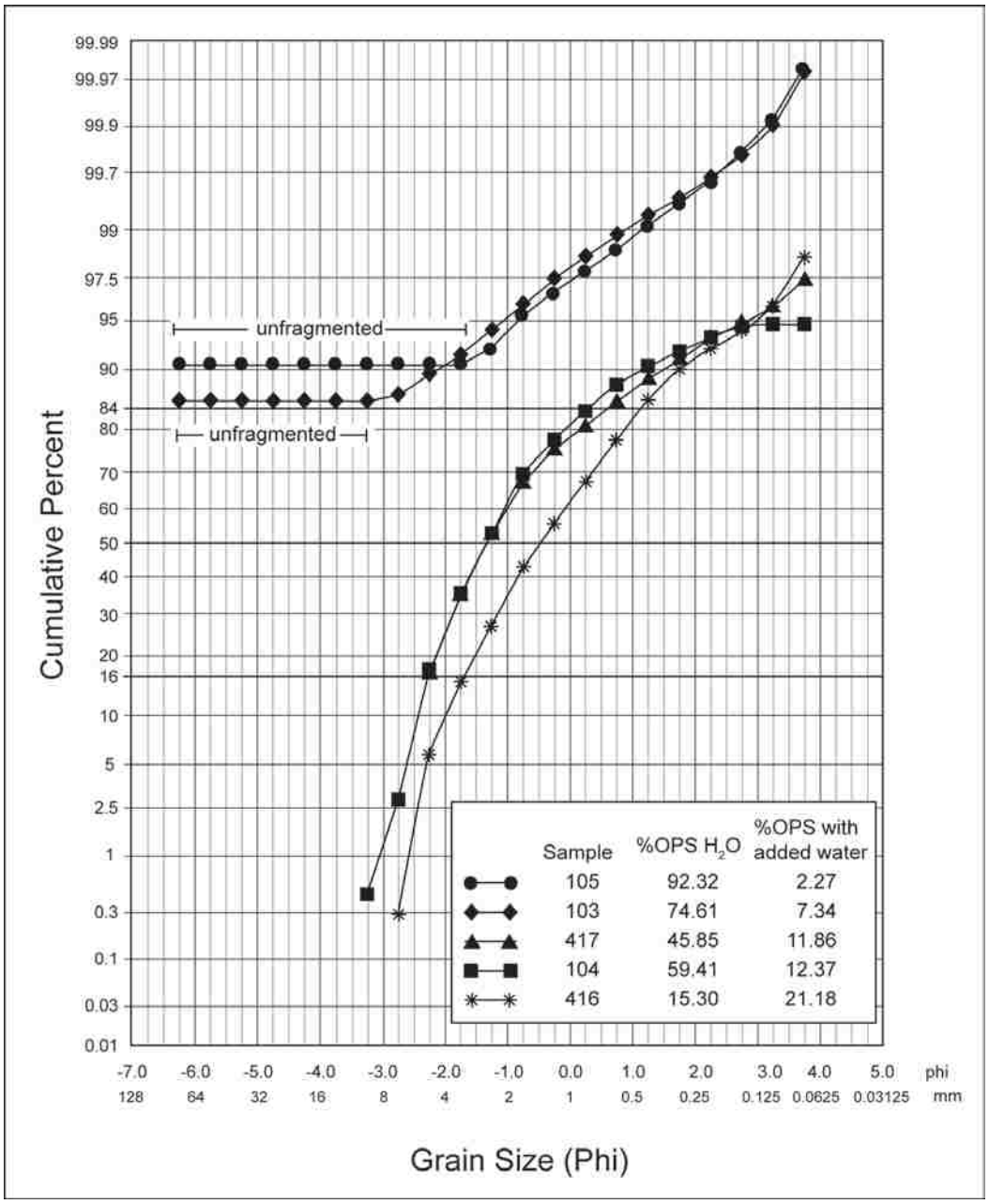

Figure 18. Cumulative frequency distribution for each sample plotted on arithmetic probability paper. Median diameter (Md_ϕ) is the phi-size at which the sample's curve crosses the 50% mark. Graphical standard deviation ($\sigma_\phi = [\phi_{84} - \phi_{16}]/2$) is calculated using the phi values at 16% (ϕ_{16}) and 84% (ϕ_{84}) cumulative percent value.

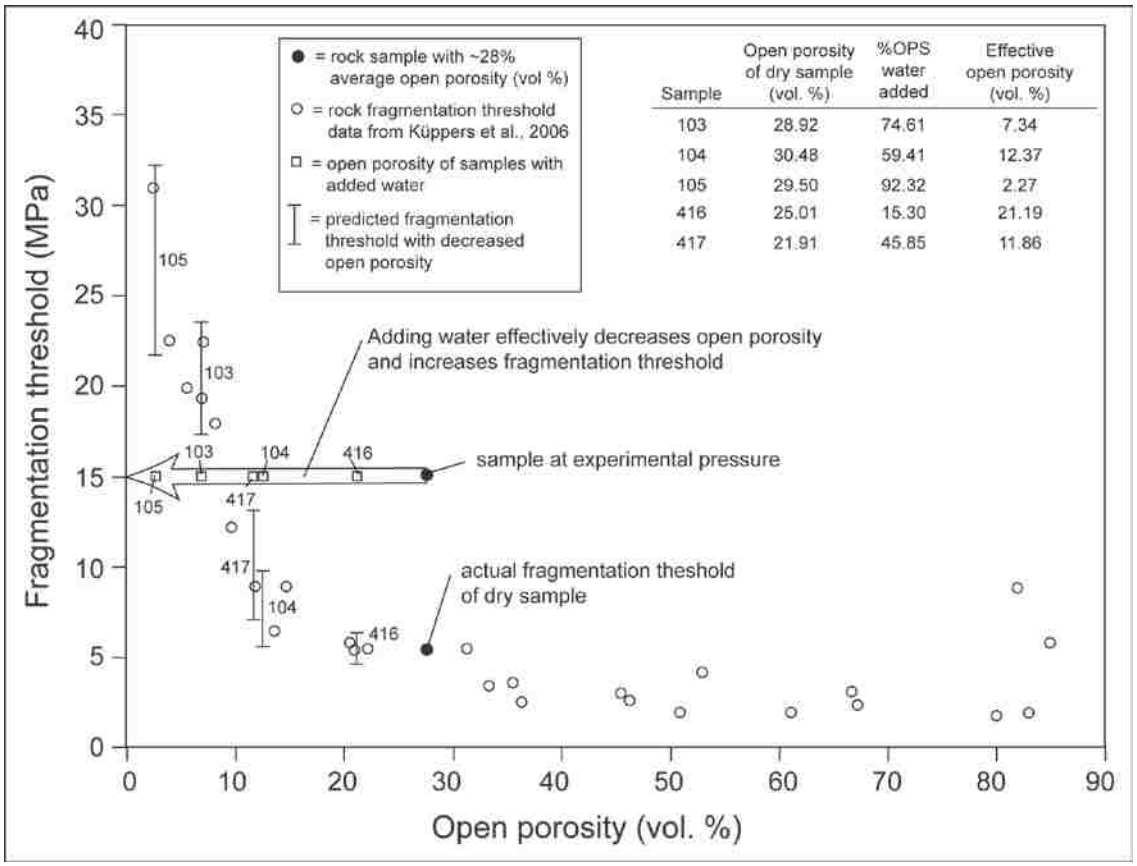

Figure 19. Adding water to open pore space of the rock samples reduces overall open porosity (vol. %) and increases fragmentation threshold. Base graph adapted from Küppers et al., 2006

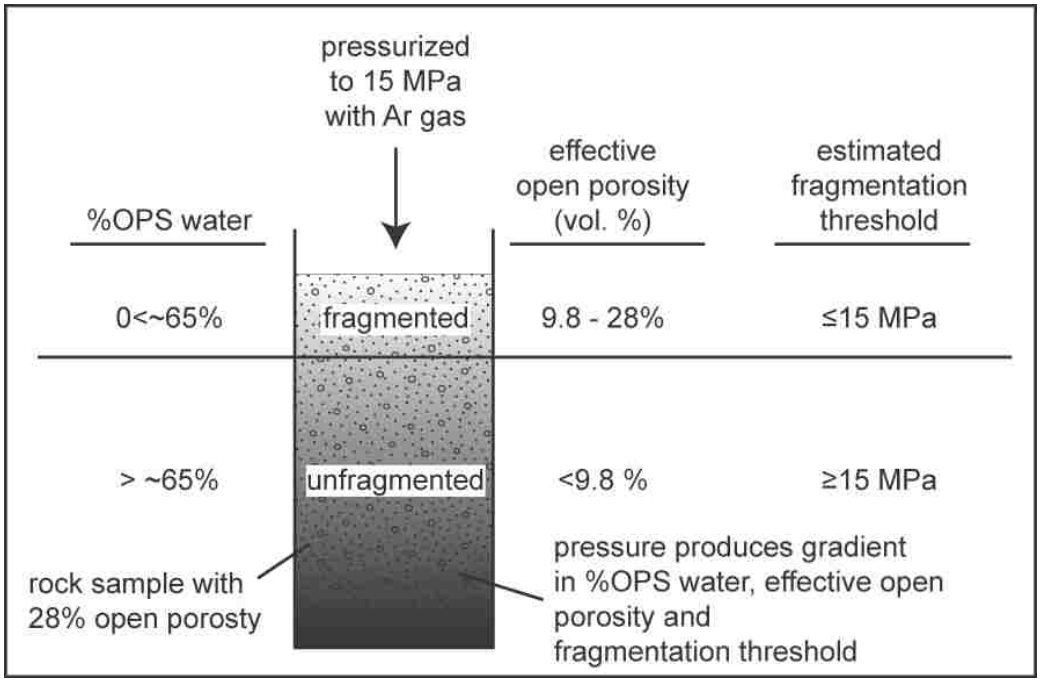

Figure 20. Pressurizing the samples pushes the water to the bottom of the sample creating a gradient of %OPS water, open porosity (vol. %), and fragmentation threshold.

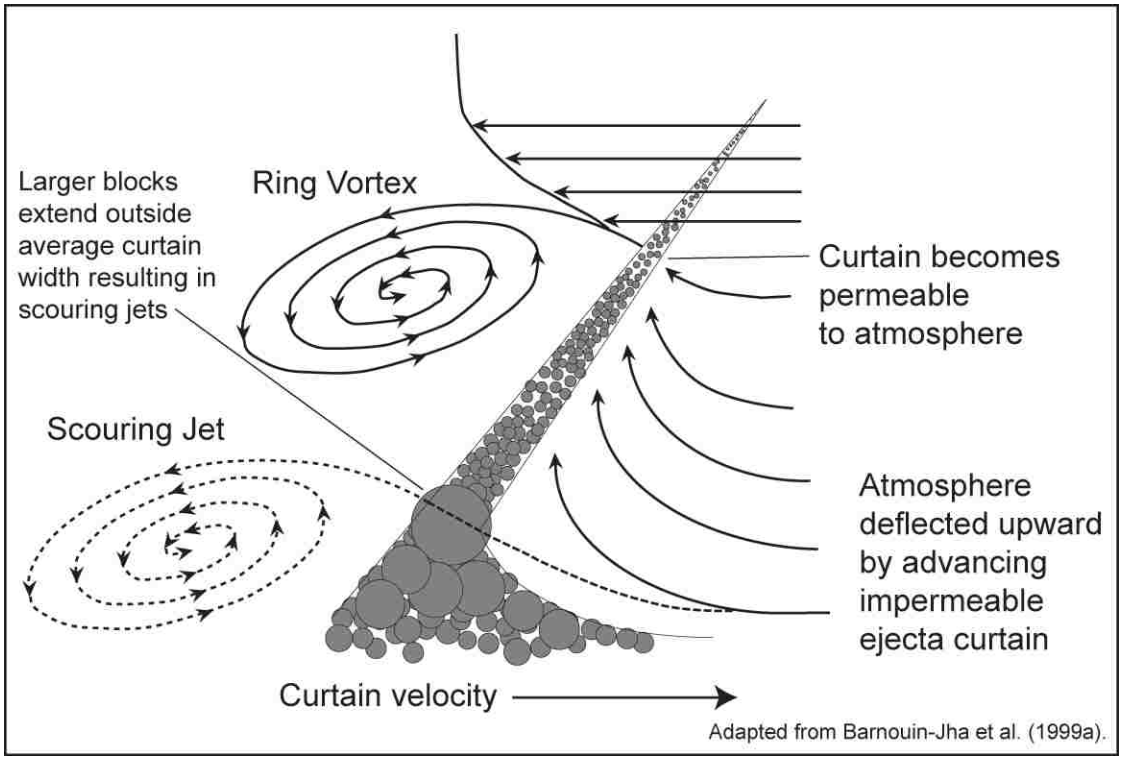

Figure 21. Proposed model for the formation of double-layered ejecta (DLE). In this model, the inner ejecta layer is formed when the larger blocks at the base of the ejecta curtain drop out of the curtain. A ring vortex, which forms where the ejecta curtain becomes permeable to the atmosphere, is responsible for the outer ejecta layer. At the base of the ejecta curtain, instabilities form at discrete locations where larger blocks extend outside the average width of the ejecta curtain. The instabilities result in scouring jets punching through the ejecta curtain forming scouring jets which extend from near the crater rim to the distal rampart of the outer ejecta layer.

CHAPTER FOUR

SUMMARY AND FUTURE RESEARCH

Introduction

This chapter presents a summary of the significant results from experiments conducted for this dissertation and how those results fit into the proposed hybrid model for fluidized ejecta formation. An outline of possible future research is also presented.

Summary

Results

This dissertation involved a study of the effects of water content on rock fragmentation during rapid decompression using the Shock Tube Laboratory at the University of Munich. Samples were decompressed from 15 MPa at starting temperatures that resulted in the sample either (1) crossing the vaporization curve for water (177 ºC and 300 ºC) or (2) remaining in liquid form upon decompression (50 ºC).

When the vaporization curve is crossed during decompression (15 MPa, 177 ºC or 300 ºC) the grain-size distribution shifts to smaller size with increased water. For the northern Eldorado Mountains sandstone samples, the degree of fragmentation peaked at around 30% OPS H_2O. With increased amounts of water (>~75%) (1) the grain size distribution is similar to control samples where no water is present in the open pore space but is more uniform with a higher proportion of fines and larger blocks and (2) grain shape is blockier, indicating that the expansion of water during vaporization may be creating fractures perpendicular to the release wave front.

When the vaporization curve is not crossed during decompression (15 MPa, 50 ºC) the fragmentation threshold is increased due to a decrease in open porosity. This is

probably true only in situations where the water is confined in open pore space in a rock that has relatively low permeability preventing the liquid water from moving through the rock easily. Because ejection angle is inversely proportional to material strength, this increase in strength may result in larger blocks of ejecta being ejected at lower angles in regions where the vaporization curve is not crossed.

Proposed Model

Barlow (2005) suggested that fluidized ejecta are produced by some combination of the atmospheric model and subsurface volatile model. This dissertation presents a hybrid model in which that atmospheric and subsurface volatile models are two end-members of fluidized ejecta emplacement. Fluidized ejecta on Venus are an example of the purely atmospheric end-member; Ganymede represents the subsurface volatile end-member.

Schultz (1992a and 1992b) found that fluidized ejecta were produced during his experiments when either the grain size of the target was lowered or the atmospheric pressure was increased. The high atmospheric pressure on Venus accounts for the emplacement of fluidized ejecta on that planet even though it lacks subsurface volatiles. The atmospheric pressure on Mars is much lower, however subsurface volatiles are present. Results from studies undertaken in this dissertation suggest that when water flashes from liquid or ice to vapor during the decompression stage of impact cratering this explosive expansion increases the degree of fragmentation of the ejecta. Furthermore, vaporization of water during the excavation stage of impact cratering is the mechanism that reduces the average grain-size of the ejecta, allowing it to interact with the thin Martian atmosphere and be deposited by a ring vortex (Schultz and Gault, 1979a and

1979b; Schultz, 1992a and 1992b; Barnouin-Jha and Schultz, 1996; Barnouin-Jha et al., 1999a and 1999b) (Figure 4). The overall decrease in average grain size in the ejecta curtain lowers the impermeable length of the ejecta curtain, allowing the formation of a vortex ring that entrains and winnows the smaller ejecta from the curtain, depositing it in a fluidized fashion.

Experiments indicate that moderate amounts of water (~30% OPS water for a rock with ~28% open porosity) result in the greatest degree of fragmentation shifting the grain size distribution of ejecta toward smaller sizes. This increase in the proportion of fines allows the formation of a vortex ring in which finer particles are entrained and winnowed from the curtain.

Recent studies suggest that MLE ejecta may not be emplaced in separate multiple layers (Boyce et al., 2010). Instead, the morphology is created due to Raleigh-Taylor or Kelvin-Helmholtz instabilities (Chandrasekhar, 1981; Boyce et al., 2010) in the ejecta. This dissertation proposes that SLE and MLE are formed by a similar mechanism and the difference in the morphologies is due to these instabilities (Chandrasekhar, 1981; Boyce et al., 2010) correlated with the larger size of MLE craters and, consequently, larger amounts of ejecta.

Experiments reported in this chapter show that DLE craters form in situations where the target contains a relatively large amount of water and most of the water does not cross the vaporization curve (Figures 17, 18, and 21). This situation results in ejecta consisting of more larger blocks and more fine-grained particles. The increase in larger blocks at the base of the ejecta curtain results in places in the curtain where some larger blocks extend outside the average ejecta curtain width (Figure 21) Raleigh-Taylor or

Kelvin-Helmholtz instabilities (Chandrasekhar, 1981; Boyce et al., 2010) may form at these locations, creating jets beneath the ring vortex (Figure 21). These jets do not form a vortex ring. They are closer to the ground than the vortex ring and travel behind it, and scour the surface. When the larger blocks fall out of the ejecta curtain, these jets persist behind the ring vortex and continue producing the scouring pattern to the end of the outer DLE layer.

Future Research

This dissertation has potentially opened up a new subdiscipline in impact crater experimental research. This research marks the first time the fragmentation of rock-water mixtures due to shock decompression has been studied. This is also the first research to consider how the variations of grain-size distributions resulting from various rock-water mixtures may affect the ejecta curtain and its interaction with the atmosphere. Because this is a new area of research, a lot of questions remain to be answered.

Planned future research includes conducting more experiments on various rock types, porosities, permeabilities, and water content. High-speed videography and/or pressure transducers will be used to measure the relationship between water content and the speed of fragmentation. This work may be applied to planetary surfaces to better understand distribution of subsurface volatiles and the physical conditions of impacts.

REFERENCES CITED

Alidibirov, M. A., and Dingwell, D. B., 1996a, An experimental facility for the investigation of magma fragmentation by rapid decompression: Bulletin of Volcanology, v. 58, no. 5, p. 411-416.

Alidibirov, M., and Dingwell, D. B., 1996b, Magma fragmentation by rapid decompression: Nature (London), v. 380, no. 6570, p. 146-148.

Anderson, R. E., 1971, Thin skin distension in Tertiary rocks of southeastern Nevada: Geological Society of America Bulletin, v. 82, no. 1, p. 43-58.

Balsillie, J. H., Donoghue, J. F., Butler, K. M., and Koch, J. L., 2002, Plotting equation for Gaussian percentiles and a spreadsheet program for generating probability plots: Journal of Sedimentary Research, v. 72, no. 6, p. 929-933.

Bandfield, J.L., Hamilton, V.E., and Christensen, P.R., 2000, A global view of Martian surface compositions from MGS-TES: Science, v. 287, no. 5458, p. 1626-1630

Baratoux, D., Delacourt, C., and Allemand, P., 2002a, An instability mechanism in the formation of the Martian lobate craters and the implications for the rheology of ejecta: Geophysical Research Letters, v. 29, no. 8: p. 51-1 – 51-4.

Baratoux, D., Mangold, N., Delacourt, C., and Allemand, P., 2002b, Evidence of liquid water in recent debris avalanche on Mars: Geophysical Research Letters, v. 29, no. 7, p.60-1 – 60-4.

Barlow, N.G., 2003a, Comparison of secondary crater production by Martian and lunar impact craters: Bulletin of the American Astronomical Society. v. 35, p. 924-925.

Barlow, N.G., 2003b, Revision of the "Catalog of Large Martian Impact Craters": 6th International Conference on Mars: Houston, Texas, Lunar and Planetary Institute, Abstract no. 3073.

Barlow, N.G., 2005, A review of Martian impact crater ejecta structures and their implications for target properties, *in* Kenkmann, T., Hörz, F., and Deutsch, A., eds., Large meteorite impacts III: Geological Society of America Special Paper 384, p. 433-442.

Barlow, 2008, Mars: An introduction to its interior, surface, and atmosphere: Cambridge, UK, Cambridge University Press, 264 pp.

Barlow, N.G., 2010, What we know about Mars from its impact craters: Geological Society of America Bulletin, v. 122, no. 5-6, p. 644-657.

Barlow, N.G., and Bradley, T.L., 1990, Martian impact craters; correlations of ejecta and interior morphologies with diameter, latitude, and terrain: Icarus, v. 87, no. 1, p. 156-179.

Barnouin-Jha, O.S., and Schultz, P.H., 1996, Ejecta entrainment by impact generated ring vortices: Theory and experiments: Journal of Geophysical Research, v. 101, p. 21,099-21,115.

Barnouin-Jha, O.S., and Schultz, P.H., 1998, Lobateness of impact ejecta deposits from atmospheric interactions: Journal of Geophysical Research, v. 103, p. 25739-25756.

Barnouin-Jha, O.S., Schultz, P.H., and Lever, J.H., 1999a, Investigating the interactions between an atmosphere and an ejecta curtain. 1. Wind tunnel tests: Journal of Geophysical Research, v. 104, p. 27105-27115.

Barnouin-Jha, O.S., Schultz, P.H., and Lever, J.H., 1999b, Investigating the interactions between an atmosphere and an ejecta curtain. 2. Numerical experiments: Journal of Geophysical Research, v. 104, p. 27117-27131.

Boyce, J.M., Barlow, N.G., Mouginis-Mark, P.J., and Stewart, S.T., 2008, Ganymede rampart craters: Their possible implications to the role of subsurface volatiles in emplacement of Martian layered ejecta: Lunar and Planetary Institute, Abstract 1402.

Boyce, J.M., Barlow, N.G., Mouginis-Mark, P.J., and Stewart, S.T., 2010, Rampart craters on Ganymede: Their implications for fluidized ejecta emplacement, Meteoritics and Planetary Science, v. 45, no. 4, p. 638 – 661.

Boyce, J. M., and Mouginis-Mark, P. J., 2006, Martian craters viewed by the Thermal Emission Imaging System instrument: Double-layered ejecta craters, Journal of Geophysical Research: Planets, v. 111. p. 1-21.

Carr, M.H., 1996, Water on Mars: New York, Oxford University Press, 229 p.

Carr, M.H., Crumpler, L.S., Cutts, J.A., Greeley, R., Guest, J.E., and Masursky, H., 1977, Martian impact craters and emplacement of ejecta by surface flow: Journal of Geophysical Research, v. 82, p. 4055-4065.

Chandrasekhar, S. 1981, Hydrodynamic and Hydromagnetic Stability, Oxford: Clarendon Press , 704 pp.

Costard, F.M., 1989, The spatial distribution of volatiles in the Martian hydrolithosphere: Earth, Moon, and Planets, v. 45, p. 265-290.

Costard, F.M., and Kargel, J.S., 1995, Outwash plains and thermokarst on Mars: Icarus, v. 114, p. 93-112.

de Pater, I., Lissauer, J. J., 2001, Planetary Sciences: New York, NY, Cambridge University Press, 528 pp.

French, B. M., 1998, Traces of catastrophe: A handbook of shock-metamorphic effects in terrestrial meteorite impact structures, Houston, TX, Lunar and Planetary Institute, 118 pp.

Garvin, J.B., Sakimoto, S.E.H., Frawley, J.J., and Schnetzler, C., 2000, North polar region crater forms on Mars: Geometric characteristics from the Mars Orbiter Laswer Altimeter: Icarus, V. 144, p. 329-352.

Garvin, J.G., Sakimoto, S.E.H., and Frawley, J.J., 2003, Craters on Mars: Global geometric properties from gridded MOLA topography: 6th International Conference on Mars: Houston, Texas, Lunar and Planetary Institute, Abstract no. 3277.

Gault, D.E., Shoemaker, E.M., and Moore, H.J., 1963, Spray ejected from the lunar surface by meteoroid impact: NASA Technical Note, 39 p.

Gault, D.E., 1974, Impact craters *in* Greeley, R., and Schultz, P., eds. A primer in lunar geology; comment editionNASA, Ames Research Center, Moffett Field, California, United States.

Gault, D.E., and Wedekind, J.A., 1978, Experimental studies of oblique impact, *in* Proceedings, Lunar and Planetary Science Conference, 9th, Houston, March 1978, v. 3, no. 9, p. 3843-3875.

Gault, D. D., and Wedekind, J. A., 1979, Experimental results for effects of gravity on impact crater morphology; Second international colloquium on Mars: NASA Conference Publication no. 2072, p. 29.

Greeley, R., Gault, D.E., Snyder, D.B., Sisson, V., Schultz, P.H., and Guest, P.H., 1979. Martian multilobed craters; impact cratering simulations: EOS, Transactions, American Geophysical Union, v. 60, no. 46, p. 873.

Greeley , R., Fink, J., Gault, D.E., Snyder, D.B., Guest, J.E., and Schultz, P.H., 1980, Impact cratering in viscous targets: Laboratory experiments: Proceedings of the 11th Lunar and Planetary Science Conference: New York, NY, Pergamon Press, p. 2075-2097.

Greeley, R., Fink, J.H., Gault, D.E., and Guest, J.E., 1982, Experimental simulation of impact cratering on icy satellites, *in* Morrison, D., *eds*., Satellites of Jupiter: Tucson, Arizona, University of Arizona Press, p. 340-378.

Grieve, R.A.F., Dence, M.R., and Robertson, P.B., 1976, Cratering processes as interpreted from the occurrence of impact melts, *in* Proceedings, Lunar Science Institute topical conference, Symposium on planetary cratering mechanics, Flagstaff, Ariz., United States, Sept. 13-17, 1976, p. 791- 814.

Grieve, R.A.F., and Cintala, M.J., 1981, A method for estimating the initial impact conditions of terrestrial cratering events, exemplified by its application to Brent Crater, Ontario, *in* Proceedings, Lunar and Planetary Science Conference, 12th, Houston, March 1981, no. 12, Part B, p. 1607-1621.

Grieve, R. A. F., 1991, Terrestrial impact; the record in the rocks: Meteoritics, v. 26, no. 3, p. 175-194.

Head, J. N., Melosh, H.J., and Ivanov, B.A., 2002, Martian meteorite launch: High speed ejecta from small craters: Science, v. 298, no. 5599, p. 1752-1756.

Housen, K.R., Schmidt, R.M., and Holsapple, K.A., 1983, Crater ejecta scaling laws: Fundamental forms based on dimensional analysis: Journal of Geophysical Research, v. 88, p. 2485-2499.

Idelchik, I.E., 1994, Handbook of Hydraulic Resistance, Boca Raton, Florida, CRC Press, 790 pp.

Inman, D. L., 1952, Measures for describing the size distribution of sediments: Journal of Sedimentary Petrology, v. 22, no. 3, p. 125-145.

Küppers, U., Scheu, B., Spieler, O., and Dingwell, D.B., 2006, Fragmentation efficiency of explosive volcanic eruptions; a study of experimentally generated pyroclasts; MULTIMO; Multi-parameter monitoring, modeling and forecasting of volcanic hazard results from a European project: Journal of Volcanology and Geothermal Research, v. 153 (1-2), p. 125-135.

Kuzmin, R.O., Bobina, N.N., Zabalueva, E.V., and Shashkina, V.P., 1988, Structural inhomogeneities of the Martian cryosphere: Solar System Research, v. 22, p. 121-133.

Longhi, J., 2006, Phase equilibrium in the system CO_2-H_2O Application to Mars: Journal of Geophysical Research, v. 111, no. E06011, p. 1-16.

Malin, M. C., and Edgett, K.S., 2000a, Evidence for recent groundwater seepage and surface runoff on Mars: Science. v. 288, no. 5475, p. 2330-2335.

Malin, M. C., and Edgett, K.S., 2000b, Sedimentary rocks of early Mars: Science, v. 290, no. 5498, p. 1927-1937.

Maxwell, D.E., 1977a, Simple Z-model of cratering, ejection and the overturned flap, *in* Impact and Explosion Cratering, Roddy, D.J., Pepin, R.O., and Merrill, R.B., Pergamon Press, Tarrytown, New York, p. 1003-1008.

Maxwell, D. E., 1977b, Simple Z model of cratering, ejection, and the overturned flap; Impact and explosion cratering; planetary and terrestrial implications; Proceedings of the Symposium on planetary cratering mechanics, *in* Lunar Science Institute topical conference; Symposium on planetary cratering mechanics, Flagstaff, Arizona, United States (USA).

Maxwell, D.E., 1977c, Simple Z model of cratering, ejection, and the overturned flap, *in* Roddy, D.J., Pepin, R.O., Merrill, R.B., eds., Impact and explosion cratering; planetary and terrestrial implications; Proceedings of the Symposium on planetary cratering mechanics, Lunar Science Institute topical conference ; Symposium on planetary cratering mechanics, Flagstaff, Ariz., United States, Sept. 13-17, 1976, p. 1003-1008.

McEwen, A., Turtle, E., Burr, D., Milazzo, M., Lanagan, P., Christensen, P., and Boyce, J., and the THEMIS science team, 2003, Discovery of a large rayed crater on Mars: Implications for recent volcanic and fluvial activity and the origin of Martian meteorites: Lunar and Planetary Science XXXIV: Houston, Texas, Lunar and Planetary Institute, Abstract no. 2040.

McGlaun, J.M., and Thomson, S.L., 1990, CTH: A three dimensional shock wave physics code: International Journal of Impact Engineering, v. 10, p. 360-361.

Melosh, H. J., 1989, Impact cratering: A geologic process: Oxford, UK, Oxford Monographs on Geology and Geophysics, v. 11, p. 245.

Melosh, H. J. 1984. Impact ejection, spallation, and the origin of meteorites: Icarus v. 59, no. 2, p. 234-260.

Moore, J.G., 1967, Base surge in recent volcanic eruptions: Bulletin of Volcanology, v. 30, p. 337 – 363.

Mouginis-Mark, P., 1979, Martian fluidized ejecta morphology: Variations with crater size, latitude, altitude, and target material: Journal of Geophysical Research, v. 84, p. 8011-8022.

Mouginis-Mark, P.J., 1987, Water or ice in the Martian regolith? Clues from rampart craters seen at very high resolution: Icarus, v. 71, p. 268-286.

O'Keefe, J.D., Stewart, S.T., Lainhart, M.E., and Ahrens, T., 2001, Damage and rock-volatile mixture effects on impact crater formation: International Journal of Impact Engineering, v. 26, p. 543-553.

Orphal, D.L., Borden, W.F., Larson, S.A., and Schultz, P.H., 1980, Impact melt generation and transport: Proceedings of the Lunar and Planetary Science Conference, XI, p. 2309-2323.

Schultz, P.H., and Gault, D.E., 1979a, Atmospheric effects on Martian ejecta emplacement: Journal of Geophysical Research, v. 84, p. 7669-7687.

Schultz, P. H., and Gault, D.E., 1979b, Martian impact crater ejecta emplacement: Second international colloquium on Mars. NASA Conference Publication no. 2072, p. 72.

Schultz, P.H, and Gault, D.E, 1982, Impact ejecta dynamics in an atmosphere: experimental results and extrapolations, *in* Silver, L.T., and Schultz, P.H., eds.,

Geological implications of impacts of large asteroids and comets on the Earth: Geological Society of America Special Paper 190, p. 153-174.

Schultz, P.H., 1992a, Atmospheric effects on ejecta emplacement: Journal of Geophysical Research, v. 97, p. 11623-11662.

Schultz, P.H., 1992b, Atmospheric effects on ejecta emplacement and crater formation on Venus from Magellan: Journal of Geophysical Research, v. 97, p. 16183-16248.

Senft, L.E., and Stewart, S.T., 2007, Diagnostic features from modeling impact cratering in icy layered terrains on Mars, *in* Proceedings, Seventh international conference on Mars, Pasadena, CA, United States, July 9-13, 2007, Abstract 3309.

Senft, L.E., and Stewart, S.T., 2008, Impact crater formation in icy layered terrains on Mars: Meteoritics & Planetary Science, v. 43, no. 12, p. 1993-2013.

Senft, L.E., and Stewart, S.T., 2009, The role of phase changes during impact cratering on icy satellites, *in* Lunar and Planetary Science XL: Houston, Texas, Lunar and Planetary Institute, Abstract 2130.

Sneed, E. D., and Folk, R.L, 1958, Pebbles in the lower Colorado River, Texas; a study in particle morphogenesis: Journal of Geology, v. 66, no. 2, p. 114-150.

Squyres, S. W., Knoll, A. H., Arvidson, R. E., Clark, B. C. Grotzinger, J. P., Jolliff, B. L., McLennan, S. M., Tosca, N., Bell III, J. F., Calvin, W. M., Farrand, W. H., Glotch, T. D., Golombek, M. P., Herkenhoff, K. E., Johnson, J. R., Klingelhofer, G., McSween, H. Y., Yen, A. S., 2006, Two years at Meridiani Planum: Results from the opportunity rover: Science, v. 313, no. 5792, p. 1403- 1407.

Stewart, S.T. and Ahrens, T.J., 2003, Shock Hugoniot of H_2O ice: Geophysical Research Letters, v. 30, no. 6, 1332.

Stewart, S. T., Ahrens, T. J., and O'Keefe, J. D, 2003, Impact-induced melting of near-surface water ice on Mars. *in* Shock Compression of Condensed Matter-2003, p. 1484-1487, Eds. M.D. Furnish, Y. M. Gupta, and J. W. Forbes, American Institute of Physics, 2004.

Stewart, S.T., and Ahrens, T.J., 2005, Shock properties of H_2O ice: Journal of Geophysical Research, v. 110, 23 p.

Stewart, S.T., O'Keefe, J.D., and Ahrens, T.J., 2001, The relationship between rampart crater morphologies and the amount of subsurface ice: Lunar and Planetary Science XXXII: Houston, Texas Lunar and Planetary Institute, Abstract no. 2092.

Waters, A.C., and Fisher, R.V., 1971, Base surges and their deposits: Capelinhos and Tall volcanoes: Journal of Geophysical Research, v. 76, p. 5596 – 5614.

Wohletz, K.H., and Sheridan, M.F., 1979, A model of pyroclastic surge: Geological Society of America Special Paper, 180, p. 177-193.

Wohletz, K.H., and Sheridan, M.F., 1983, Martian rampart crater ejecta: Experiments and analysis of melt-water interaction: Icarus, v. 56, p. 15-37.

APPENDIX 1

IMPACT CRATERING

Introduction

For the reader who is unfamiliar with the impact cratering process, this appendix provides an overview. Impact cratering stages, morphologies, and factors that affect both will be discussed.

Impact Cratering Stages

Contact/Compression Stage

The contact/compression stage (Figure 22) begins when the leading edge of a projectile traveling at hypervelocity speeds (typically 10-40 km s^{-1} for large meteoroids on Earth) impacts a target (de Pater and Lissauer 2001, French 1998, Melosh 1989). If the target is solid, the projectile is stopped in a fraction of a second and penetrates the target no more than 1 to 2 times its diameter. At this instant, kinetic energy is converted into two sets of shock waves. One set of shock waves is transmitted forward from the projectile/target interface into the target rocks while a complementary shock wave is reflected back into the projectile.

At the impact point, peak shock-wave pressures (Figure 23) may exceed 100 GPa for typical cosmic encounter velocities (French 1998). The shock waves transmitted into the target rocks lose energy rapidly as they travel away from the impact point such that the impact point as surrounded by a series of concentric, roughly hemispheric shock zones. Each shock zone is distinguished by a certain range of peak shock pressures and characterized by a unique suite of shock-metamorphic effects produced in the rocks.

Farther outward from the impact, pressures of 10 – 50 GPa may exist over distances of many kilometers from the impact point. Intense pressures near the point of impact produce total melting and/or vaporization of the projectile and surrounding rock.

At greater distances, peak shock wave pressures drop to 1 to 2 GPa (Figure 23). This is the approximate location of what will eventually become the crater rim. At this point, the shock waves become elastic waves or seismic waves. Velocity drops to that of the speed of sound in the target rocks (5 to 8 km/s). These are low pressure waves, similar to those generated by earthquakes and volcanic eruptions, which do not produce any permanent deformation to the rocks through which they pass. They can, however, produce fracturing, brecciation, faulting, and near-surface landslides which may be difficult to distinguish from normal geologic processes.

When the shockwave reaches the back of the projectile, it is reflected forward into the projectile as a rarefaction or tensional wave (also called a release wave). As the rarefaction wave passes through the projectile from back to front, it unloads the projectile from the high shock pressures it has experienced. This release results in the virtually complete melting and vaporization of the projectile.

At the instant the rarefaction wave reaches projectile-target interface, the whole projectile is unloaded and the release wave continues forward into the target and continuing to decompress the target as well. The point at which the rarefaction wave reaches the target marks the end of the contact/compression stage.

The duration of the contact compression stage is determined by the behavior of the shock wave that is reflected back into the projectile from the projectile/target interface. After the release wave has reached the projectile/target interface and has

unloaded the projectile, the projectile plays no further role in the formation of the impact crater. The excavation of the crater is carried out by the shock waves expanding through the target rocks. The vaporized portion of the projectile may expand out of the crater as part of a vapor plume (Melosh, 1989) and the remainder, virtually all melted, may be violently mixed into the melted and brecciated target rocks. The contact/compression stage lasts no more than a few seconds, even for very large projectiles. For most impact events, the contact compression stage takes less than one second.

Excavation Stage

During the excavation stage (Figure 22), the actual impact crater is opened up by complex interactions between the expanding shock waves and the original ground surface (Melosh 1989, Grieve 1991). At the beginning of the excavation stage, the projectile is surrounded by a roughly hemispherical envelope of shock waves that expand rapidly through the target rock. The center of this hemisphere actually lies within the original target rock at a point below the original ground surface.

Within this hemispherical envelope, the shock waves that travel upward and intersect the original ground surface are reflected downward as rarefactions (release waves). In a near surface region where the stresses in the rarefaction wave exceed the mechanical strength of the target rocks, the rarefaction wave is accompanied by fracturing and shattering of the target rock. The reflection of the shock waves converts the initial shock-wave energy to kinetic energy, and target material is accelerated outward, usually as individual fragments traveling at high velocities.

The complex processes of the excavation stage push the target materials outward from the impact point, producing a symmetric excavation flow around the center of the

developing crater. Exact flow directions vary with location within the target rocks. Most target material from the upper levels moves downward and outward, quickly producing a bowl-shaped depression (transient cavity or transient crater) in the target (Maxwell, 1977a,1977b, and 1977c; Grieve et al., 1976; Grieve and Cintala, 1981; and Melosh, 1989)

The growth of the transient crater ceases when the shock and release waves can no longer excavate or displace the target rock. At this point, the excavation stage ends and the modification stage begins (Melosh 1989).

Modification Stage

The excavation stage ends when the transient crater has grown to its maximum size, and the subsequent modification stage begins immediately (Figure 22). The expanding shock waves have now decayed to low-pressure elastic stress waves beyond the crater rim, and they play no further part in the crater development. Instead, the transient crater is immediately modified by more conventional geologic processes (e.g. erosion, faulting). The extent to which the transient crater is modified is a function of its size and (to a lesser extent) the properties of the target.

Modification of small bowl-shaped craters occurs mainly from collapse of their upper walls and the final crater is changed very little from the original transient crater. In larger craters, modification may involve major structural changes including uplift of the central part of the floor and major peripheral collapse around the rim. Depending on the extent to which the transient crater is modified, three distinct types of impact structures can be formed. These crater morphology types (including simple craters, complex craters, and multiring basins) occur in order of increasing crater size.

Crater Morphology

Simple Craters

Simple craters are small (generally less than a few kilometers in diameter) bowl-shaped craters formed by hypervelocity (speeds exceeding a few kilometers per second) impacts. The depth (rim to crater floor) of a simple crater is typically about one-fifth of its diameter. Rim height is about 4% of the crater's diameter. Variations in depth-to-diameter ratio occur due to variations in strength of the target and surface gravity (Gault, 1974; Gault and Wedekind, 1979; Greeley, 1979; Melosh, 1989).

In the case of simple craters, the transient crater is modified only by minor collapse of the steep upper crater wall and by redeposition of a small amount of ejected material back into the crater. This results in an increase in crater diameter by as much as 20% relative to the transient crater. During modification, the simple crater is immediately filled, to perhaps half its original depth, by a mixture of redeposited (fallback) ejecta and debris slumped in from the walls and rim. The material that falls back into the crater is called the breccia lens or crater-fill breccia. This breccia is a mixture of shocked and unshocked rock fragments and impact melt fragments (Melosh, 1989).

There is no lower limit to the size of simple craters. However, the upper size limit is inversely correlated with gravity. The transition from simple to complex crater morphology occurs at a smaller diameter on Mars than on the Moon. This transition from simple to complex morphology appears to reflect the onset of gravitational collapse. Because of their relatively small size, simple craters are quickly eroded or buried on planets with geologically active surfaces (Melosh, 1989).

Simple craters produced by hypervelocity impacts can be differentiated from craters produced by meteoroids moving at slower speeds on the basis of morphology (Melosh 1989). The latter tend to have irregular shapes in plan view and have broader, less well-defined rims than the former. These craters are termed secondary craters because they form by secondary ejecta thrown out during the excavation stage of large primary impacts. Secondary craters tend to form in chains or clusters due to their common, nearly simultaneous origin from a larger hypervelocity impact. There is no lower limit to the size of simple craters. The upper limit to the size of simple craters is inversely correlated with gravity (Gault, 1974; Gault and Wedekind, 1979; Greeley, 1979; Melosh, 1989), and thus varies among Solar System bodies.

Complex Craters

Large craters are more complex. They usually have a flat floor, a central peak, and a terraced inner rim. Complex craters generally have diameters of a few tens up to a few hundred km. The morphology of small craters is controlled by the strength of the material, while the morphology of complex craters is controlled by gravity. Thus the transition diameter between simple and complex craters varies on each Solar System body.

The transition size between small and larger craters is ~18 km on the Moon and scales inversely with the gravitational acceleration, g_p, although it also depends on the strength of the target's surface material. On the Moon, Mars, and Mercury, craters 100 to 300 km in diameter show a concentric ring of peaks, rather than a single central peak. This inner ring is usually half the crater diameter. The crater size at which the central peak is replaced by a peak-ring scales in the same way as the transition diameter between

small and complex craters (French 1998, Melosh 1989). There are no peak-ring craters on icy satellites (dePater and Lissauer 2001).

Multiring Basins

Multiring basins have been produced by the impact of projectiles tens to hundreds of kilometers in diameter, and they date mainly from an early period in the solar system (>3.9 Ga), when such large objects were more abundant and collisions were more frequent. Multiring basins are systems of concentric rings, which cover a much larger area than the complex craters. The inner rings often consist of hills in a rough circle, and the crater floor may be partly flooded by lava and impact melt. The outer rings more clearly resemble crater rims.

Multiring basins are typically observed on planets with well-preserved ancient surfaces, such as the Moon, Mercury, parts of Mars, and some of the moons of Jupiter. There are numerous large basins (e.g., Caloris Basin, Mercury; Argyre Basin, Mars) in the solar system that do not display a pronounced multiring structure, possibly because they have been deeply eroded since they formed.

Factors Affecting Crater Morphology

The size and morphology of impact craters are primarily controlled by: (1) the kinetic energy of the impact (a function of the size and velocity of the bolide); (2) various properties of the target such as rock strength, layering, and the presence or absence of volatiles; and (3) gravity of the target body. Other controls on crater and ejecta blanket morphology include the angle of the impact and interactions of the bolide and ejected material with the atmosphere.

Kinetic Energy of the Impact

The size of an impact crater is positively correlated with kinetic energy (KE) an impactor possesses. Kinetic energy is described as:

$KE = 1/2(mv^2)$

where m=mass of impactor(kilograms) and v = velocity of bolide (meters/second)

Structure and Composition of Target

Layers of different strength in the target produce concentric craters. Regional joint trends may result in square or polygonal craters (e.g., Meteor Crater, Arizona, U.S.A.). Preexisting topography of the target may produce extra-wide terraces in the walls of complex craters adjacent to topographic highs

Gravity of Target Body

Gravity affects the impact cratering process by influencing (Gault 1974): (a) the dimensions of the excavation bowl, (b) the extent of the ejecta, and (c) various post-impact crater modifications. All things being equal, fragmented blocks of ejecta are excavated more easily on low-gravity planets, resulting in larger craters relative to high-gravity environments. Under low-gravity conditions, ejecta is thrown farther producing a thinner ejecta layer extending a greater distance from the crater rim on lower gravity bodies (e.g., the Moon) compared to higher-gravity bodies (e.g., Mars or Mercury). During the modification stage, gravity governs the rate of isostatic adjustments, influencing the degree of slumping and perhaps the magnitude of potential central uplifts.

Angle of Impact

The shape of impact craters plan view is controlled by the entry angle of the incoming bolide. For most impacts, both the crater and the distribution of ejecta are concentrically symmetrical about the point of impact, because most impacts (>15º entry angle) involve essentially point-source transfers of energy.

Although common sense might suggest that a bolide contacting a target surface at any angle other than a right angle would cause elongate craters, experiments have shown that only for very low angles (<15º) do impact craters become noticeably asymmetrical (Gault and Wedekind, 1978). These very low angle impacts often produce a butterfly-shaped ejecta blanket.

Atmosphere

If the target body had a dense atmosphere (e.g., Earth, Venus) impacts may be modified extensively. Atmospheric drag can slow down a small meteoroid, so that it merely hits the surface at the terminal velocity producing a non-hypervelocity impact crater. Larger bodies can explode in the air, never creating an impact crater. Projectiles may be completely vaporized while plunging through the atmosphere, and never hit the ground. Or the projectile might break up into many pieces, producing a chain of smaller impact craters.

Ejecta may interact with a thick atmosphere and small particles may be suspended in the atmosphere. This may result in particles being deposited over a longer period of time, perhaps closer to the crater rim. Or the particles may be caught in the stratosphere and transported greater distances (e.g., Chicxulub).

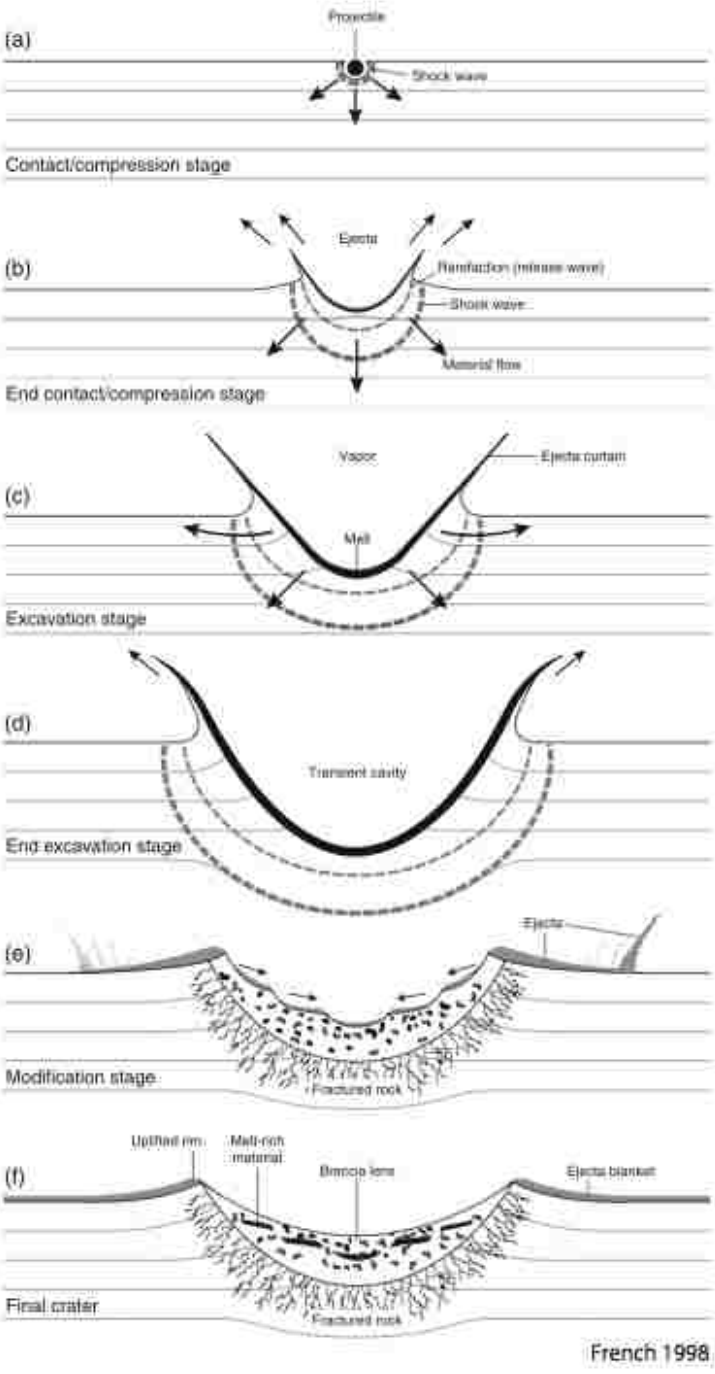

Figure 22. Stages of impact crater development (French 1998).

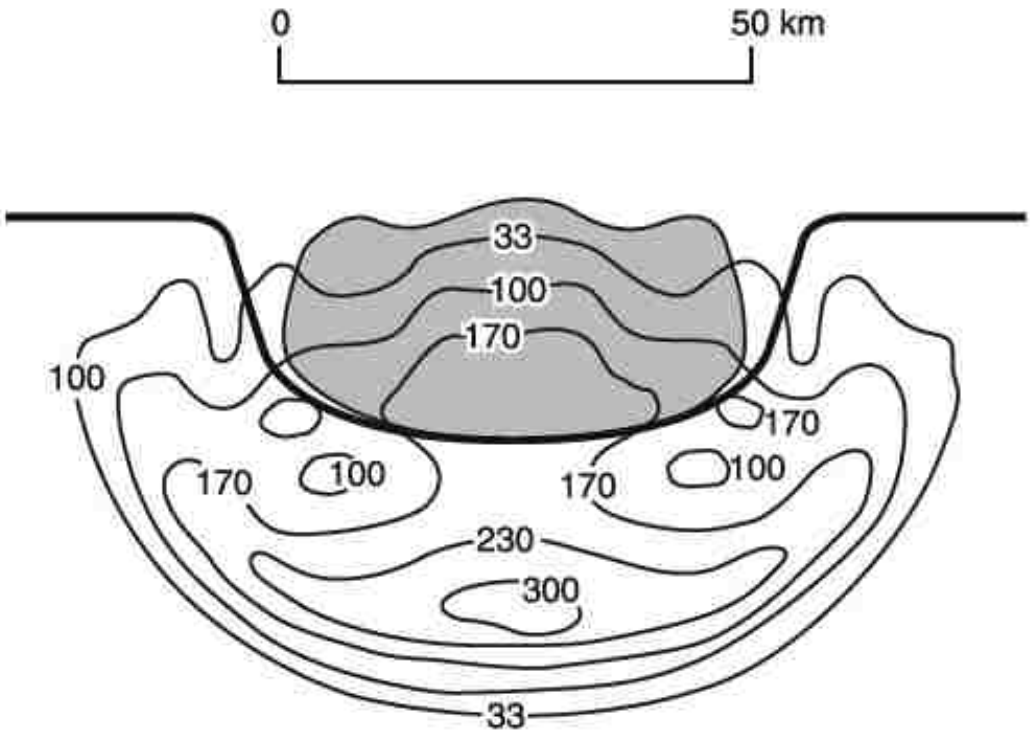

Figure 23. Shock wave propagation during the contact and compression stage (MPa). From Melosh 1989.

APPENDIX 2

MARTIAN RAMPART CRATERS: MORPHOLOGY, DISTRIBUTION, AND CURRENT FORMATION MODELS

Introduction

This appendix presents a description of Martian rampart crater and fluidized ejecta morphologies, the distribution of fluidized ejecta morphologies, and the two current models for fluidized ejecta formation. A more detailed description of some previous studies relating to the proposed hybrid model is also presented.

Martian Rampart Crater

Imagery from the Viking Orbiter cameras, Mars Global Surveyor (MGS), Mars Orbital Camera (MOC), Mars Odyssey Thermal Emission Imaging System (THEMIS), and Mars Reconnaissance Orbiter (MRO) revealed that Martian impact craters are very different from the radial ejecta on the Moon and Mercury (Carr et al, 1977; Barlow, 2005). Most Martian impact craters have fluidized ejecta (89% of 10, 651 cataloged craters ≥5 km diameter; Barlow, 2005) that hugs topography and terminates in a distal rampart about 1.5 to 2 crater radii from the rim (Barlow, 2005; Garvin et al., 2000 and 2003; Melosh, 1989). Barlow (2005) classified three types of fluidized ejecta (Figure 1): (1) single layer ejecta (SLE), (2) double layer ejecta (DLE), and (3) multiple layer ejecta (MLE). Secondary craters are rare within the fluidized ejecta (Barlow, 2003a and 2005) blanket. Beyond the rampart, secondary craters extend many crater radii further (Barlow, 2005). For example McEwen et al. (2003) identified a 10-km-diameter crater in the Cerberus region of Mars that had strings of secondary craters extending more than 800

km from the rim but had no secondary craters within the fluidized ejecta. These extensive secondary crater strings outside of the fluidized ejecta provide important constraints on the cohesiveness of the target material (Head et al., 2002) and any model of rampart crater formation must account for this distinctive feature.

Boyce and Mouginis-Mark (2006) used Thermal Emission Imaging System (THEMIS) visible (VIS) images to describe distinct features of DLE craters including (1) a widening of the rampart in the inner ejecta layer, (2) a radial texture within the ejecta, and (3) and absence of secondary craters. Although subsurface volatiles likely play a role in the formation of SLE, DLE, and MLE, these morphologic differences suggest that DLE formed in a slightly different way. Boyce and Mouginis-Mark (2006) suggest that the DLE inner layer formed in the same way as SLE ejecta, perhaps involving both ballistic and flow processes. But they believe the outer layer may have formed through a high-velocity outflow of ejecta caused either by vortex winds generated by the advancing ejecta curtain or by a base surge. According to Boyce and Mouginis-Mark (2006), the lack of secondary craters suggests large blocks have been entrained and/or crushed by the high-velocity outflow process or have been fragmented as a result of water in the target material.

Fluidized ejecta morphologies do not appear to correlate with elevation or terrain age and there is a weak correlation with terrain type (Mouginis-Mark, 1979; Costard, 1989; Barlow and Bradley, 1990, Barlow, 2005). However, layered ejecta morphologies do exhibit a strong relationship with crater diameter and geographic location (Barlow, 2005). In the Martian equatorial region (±30º latitude), SLE craters are generally ~5 to 20 km in diameter; however, at higher latitudes, SLE craters are 5-25 km in diameter

(Mouginis-Mark, 1979; Kuzmin et al., 1988; Costard, 1989; Barlow and Bradley, 1990; Barlow, 2005)

Models for Fluidized Ejecta Formation

There are two models for the formation of fluidized ejecta on Mars (Barlow, 2005): the atmospheric model and the subsurface volatile model.

The Atmospheric Model

The atmospheric model for fluidized ejecta formation argues that the thin Martian atmosphere is the medium in which ejecta are entrained (Schultz and Gault, 1979a and 1979b; Schultz, 1992a and 1992b; Barnouin-Jha and Schultz, 1998; Barnouin-Jha et al., 1999a, 1999b; Barlow, 2005). Laboratory and experimental studies (Schultz and Gault, 1979; Schultz, 1992a and 1992b; Barnouin-Jha and Schultz, 1998; Barnouin-Jha et al., 1999a, 1999b) show that atmospheric turbulence produces a vortex ring that entrains, transports, and deposits fine-grained ejecta in a layered pattern (Barlow, 2005). In this model, larger material is ballistically emplaced ahead of the vortex ring. As the vortex ring passes, it may remobilize these larger clasts and pile them up in the distal rampart. Ejecta composed of fine grain material can flow without an accompanying gas or liquid phase (Schultz, 1992a). However, for the ejecta to flow in this manner it is necessary that the target material be composed of fine grain materials or that the impact itself produces an enormous amount of fine grained material during impact excavation (Schultz, 1992a; Boyce and Mouginis-Mark, 2006).

The Subsurface Volatile Model

In the subsurface volatile model, impact into a volatile-bearing target results in a vapor cloud that deposits the entrained ejecta as a flow surrounding the crater (Baratoux

et al, 2002; Barlow, 2005; Carr et al., 1977; Greeley et al., 1980; Greeley et al., 1982; Mouginis-Mark, 1987; Stewart et al., 2001; Stewart and Ahrens, 2003; Wohletz and Sheridan, 1983). In this model, ejecta interact primarily with this vapor cloud rather than the atmosphere. Support for this model comes from (1) correlation of rampart craters with other geomorphic features associated with subsurface water (Costard and Kargel, 1995; Carr, 1996), (2) relationships between rampart crater diameter and morphology with latitude (Costard, 1989, Barlow and Bradley, 1990), (3) hydrocode simulations of impacts into mixtures of water and rock (Stewart et al., 2001; O'Keefe et al., 2001; Stewart et al., 2003; Stewart and Ahrens, 2003; Senft and Stewart, 2007, 2008, and 2009), and (4) experiments into ice-rich targets (Stewart and Ahrens, 2005).

Previous Studies

In chapter two, evidence that the vaporization of water increases the degree of fragmentation allowing smaller particles to interact with the atmosphere and produce fluidized ejecta found in SLE and MLE rampart craters and the outer ejecta layer of SLE is presented. In chapter three, it is argued that when the vaporization curve for water is not crossed, the ejecta will consist of larger blocks with a higher liquid water content that is deposited as the thicker, convex inner layer of DLE rampart craters. This section presents some previous studies supporting the atmospheric and sub-surface volatile models with an emphasis on those studies that are pertinent to the models presented in chapters two and three.

Atmospheric Model

Schultz (1992a) conducted laboratory experiments using the vertical gun at the NASA Ames Research Center to investigate the complex interactions between impact

ejecta and the atmosphere. These experiments involved hypervelocity impacts into targets of varying grain sizes with an aluminum sphere under various atmospheric pressure and density conditions. Atmospheric pressure and density conditions were simulated by using different gases in the experimental chamber.

Schultz (1992a) found that, under vacuum conditions, ballistic ejecta form the classic cone-shaped profile. However, as atmospheric density increases, the ejecta form at a higher angle (from horizontal), bulging at the base and pinching above. This change in the ejecta curtain results from the combined effects of deceleration of ejecta smaller than a critical size and entrainment of these ejecta within atmospheric vortices created as the ejecta curtain moves outward displacing the atmosphere. Schultz (1992a) found that the degree of ejecta entrainment depends on the ratio of drag to gravity forces acting on individual ejecta and the intensity of the winds created by the advancing ejecta curtain. The degree of ejecta entrainment is positively correlated with atmospheric density and ejection velocity, but negatively correlated with ejecta density and size. He found that a wide variety of nonballistic ejecta styles were produced by varying ejecta sizes even without water in the target. He also found that ejecta run-out distances scaled to crater size on Mars should increase as $R^{1/2}$ (where R is crater radius). Therefore, long run-out ejecta flows dependent on crater diameter do not necessarily reflect the depth to a reservoir of water.

According to Schultz (1992a), nonballistic ejecta emplacement results from a two-stage process. First, the ejecta are aerodynamically decelerated to near-terminal velocity. Next, the ejecta are entrained in atmospheric turbulence created by the outward expanding wall of ballistic ejecta. Conditions leading to nonballistic ejecta emplacement

depend on a critical ejecta size which depends on (1) crater size (i.e., ejection velocity), (2) ejecta size, and (3) atmospheric pressure (i.e., density).

Schultz (1992a) divided ejecta morphologies into four increasingly complex types: ballistic, rampart, flows, and radial. These ballistic facies represent gradually decreasing ejecta thickness with distance from rim, characteristic of vacuum conditions on Mercury and the Moon. Rampart ejecta facies indicate the formation of a contiguous ridge on top of ejecta. Long run-out flow lobes (flow style) are similar to the outermost sinuous flows on MLE craters that have the highest run-out distances of all the fluidized ejecta on Mars. Radial scouring (radial style) is frequently found in DLE craters. Schultz found that ejecta morphology becomes increasingly complex with increasing atmospheric pressure, but is relatively independent of atmospheric density for a given pressure. For given impactor conditions, aerodynamic drag force relative to gravity increases if either particle size or particle density (for given impactor conditions) is decreased (Schultz, 1992a).

Schultz (1992a) found that, at high atmospheric densities, the coarser size fraction retains the undistorted funnel-shaped ejecta curtain. However, the fine size component creates a separate curtain characteristic of an impact into a target consisting of fine-size particles alone under vacuum conditions. Schultz's (1992a) experiments showed that the two curtains merge at the base. According to Schultz (1992a), this indicates aerodynamic sorting during ballistic ejection and flight may not result in aerodynamic sorting during deposition, except for very late stage fallout.

Both particle size and atmospheric density affect the shape and evolution of the ejecta curtain after crater formation (Schultz, 1992a), indicating aerodynamic drag plays

a role in the formation of nonballistic ejecta. Schultz (1992a) also found that, under high atmospheric densities, a basal ejecta surge develops and advances outward at velocities that exceed the ballistic ejecta curtain under vacuum conditions.

Entrainment of fine ejecta plays an important role in the formation of nonballistic ejecta (Schultz, 1992a). Increasing levels of entrainment results in the onset of more complex ejecta morphologies; less entrainment suppresses the complex ejecta morphologies even at high atmospheric pressures. Schultz (1992a) concluded that rampart formation is a late-stage process and requires finer fractions and that ejecta exhibited fluid-like behavior even in the absence of water due to an increase in fine materials.

During hypervelocity planetary impacts, ejecta are excavated along ballistic trajectories in an inverted cone shape that displaces the atmosphere as it advances and creates a vortex ring. This vortex ring can entrain, transport, and deposit ejecta and fine-grained surface materials. Barnouin-Jha et al. (1999a) conducted wind-tunnel experiments on the interaction of an atmosphere with an ejecta curtain. They used the results from these experiments to refine numerical models of these interactions (Barnouin-Jha et al., 1999b). According to Barnouin-Jha et al. (1999a), ejecta curtain width and velocity, particle concentration, size distribution and motion parallel to the curtain, and the density, viscosity, and compressibility of the surrounding atmosphere all influence the vortex circulation strength. The circulation generated by the ejecta curtain (Figure 4) is a function of the length (L) and outward curtain velocity (U) of the curtain where it transitions from impermeable to permeable (Barnouin-Jha and Schultz, 1996). Permeability of the ejecta curtain to the surrounding atmosphere is the primary factor

controlling the circulation generated by the advancing ejecta curtain. Curtain porosity (ϕ), curtain width (w), most common curtain ejecta particle diameter (d), the velocity of the surrounding atmosphere impinging on the curtain (U), and the surrounding atmospheric density (ρ) and viscosity (μ) (Figure 4) are the most important factors controlling formation of the vortex ring.

Laboratory and theoretical work demonstrate the vortex entrains, transports, and deposits fine grained ejecta decelerated out of the curtain (Schultz and Gault, 1979a and 1979b; Schultz, 1992a; Barnouin-Jha and Schultz, 1996). Barnouin-Jha and Schultz (1998) also showed that flow instabilities (Chandrasekhar, 1981) in the vortex result in the sinuosity or lobateness of distal ejecta facies observed in laboratory studies. Laboratory results (Schultz and Gault, 1979 and 1982; Schultz, 1992a and 1992b) also indicate that the vortex winds can mobilize and saltate target and larger ejecta that were deposited ballistically ahead of the vortex.

Wind circulation (or flow strength) generated by an advancing ejecta curtain controls most aspects of the atmospheric ejecta deposition process. Wind circulation behind the ejecta curtain is a function of the velocity and length of the curtain (Figure 4) where it transitions from an impermeable to a permeable barrier to the atmosphere (Barnouin-Jha and Schultz, 1996a and 1996b).

Windtunnel experiments (Barnouin-Jha et al., 1999a) indicate that hydraulic resistance (a measure of energy losses for one-dimensional porous flow) determines where along an ejecta-like porous plate becomes effectively permeable. Barnouin-Jha et al., (1999b) point out that published data linking hydraulic resistance to the thickness, porosity, and dominant particle size comprising a porous boundary, and atmospheric

properties such as viscosity and density (Idelchik, 1994) and be combined with atmosphere and cratering models (Maxwell, 1977a,1977b, and 1977c; Schultz and Gault, 1979; Orphal et al., 1980; Housen et al., 1983) to determine the length of the impermeable portion of the curtain and the time when it transitions from impermeable to permeable.

Wind tunnel (Barnouin-Jha et al., 1999a) and numerical (Barnouin-Jha, 1999b) results show that first order circulation (Γ, m/s) is determined by flow separation. Barnouin-Jha and Schultz (1996) showed that circulation controls the velocity and the entrainment capacity of the vortex winds developed behind the advancing ejecta curtain. The entrainment capacity, in turn, controls the ejecta deposition by the vortex. The impermeable curtain length (L) can be estimated using the hydraulic resistance criteria ζ_{cr} =10 given ϕ, w, d, ρ, and μ along the length of the ejecta curtain based on ejecta scaling rules (Schultz and Gault, 1979; Housen et al., 1983), atmospheric conditions, and assumptions on the ejecta size distribution (Barnouin-Jha et al., 1999a).

Circulation of the curtain-derived vortex is what ultimately controls nonballistic ejecta deposition (Barnouin-Jha et al., 1999a). The circulation of the curtain-derived vortex is controlled by the permeability of the ejecta curtain. To estimate the initial circulation of the vortex, the time when the curtain becomes fully permeable must be known. Experiments conducted by Barnouin-Jha et al. (1999a), show that this transition depends upon the dominant grain size of the target present in the ejecta. For experimental impacts in coarse sand (Barnouin-Jha and Schultz, 1996 and 1998) this transition occurs slowly. However, the transition occurs quickly for fine-grained pumice. For experiments into fine-grained pumice, by the time crater growth ceases, significant sized holes are

observed through the curtain near the time when crater growth ceases (Barnouin-Jha and Schultz, 1998). This rapid transition from impermeable to permeable ejecta curtain suggests that two processes compete in determining when the curtain becomes permeable (Barnouin-Jha and Schultz, 1999a): (1) uniform winnowing of ejecta by through flow, (2) Raleigh-Taylor or Kelvin-Helmholtz instabilities (Chandrasekhar, 1981).

Barnouin-Jha and Schultz (1999a) concluded that, when the size of pore space in the curtain is large (as in the case of the coarse-grained ejecta), uniform winnowing dominates and slowly erodes the curtain from the top down. They found, however, that when the size of pore space is small (as in the case of fine-grained ejecta), more pressure is exerted on the interface where the atmosphere impinges on the advancing curtain surface, leading to the growth of Raleigh-Taylor or Kelvin-Helmholtz instabilities that would punch holes through the curtain.

According to Barnouin-Jha and Schultz (1999a), a third factor that could influence when and where an ejecta curtain becomes permeable is the presence and distribution of large rocks in the ejecta curtain. They explain that, when these large rocks are located in regions of the curtain where their diameter exceeds the thickness of the curtain, the atmosphere impinging on the advancing curtain will deflect locally around these protruding rocks. This deflected atmosphere travels at a greater velocity relative to the impinging atmosphere and may punch holes through the curtain around the protruding rocks. Jets produced by this process most likely occur in the regions where the curtain is thinnest. However, these jets could form anywhere such protruding rocks exist.

The continuous solid-like nature of the curtain could be broken up by protruding rocks, possibly disrupting flow separation and vortex formation (Barnouin-Jha et al.,

1999a and 1999b). However, according to Gault et al. (1963), the most commonly cited source for calculating ejecta block size (Barnouin-Jha et al., 1999b), block sizes formed during cratering are unlikely to exceed the curtain thickness of most large craters. The blocks located well within a curtain will not influence the flow generated by a curtain thickness of most large craters. Therefore, these blocks will not influence the flow generated by a curtain because the permeability of the curtain is primarily controlled by the hydraulic resistance, which is defined in terms of the curtain's most common particle diameter *d* (Barnouin-Jha et al., 1999a and1999b). The large blocks will only create jetting toward the top of the curtain where the curtain is thinner, or after enough time has passed that larger amounts of curtain material are eroded away and thinning the width of the curtain and exposing the large blocks. In the latter case (Barnouin-Jha et al., 1999b), the vortex flow should be well established by the time the large blocks are exposed, entraining the fine-grained material away from around the blocks that continue on ballistic paths (Schultz and Gault, 1979a, 1979b, and 1982; Schultz, 1992a).

Subsurface Volatile Model

Kieffer and Simonds (1980) noted that impacts into volatile-rich targets result in rapid volatile expansion which widely disperses impacts melts in thinner deposits when compared to targets with little or no volatiles. They found that impacts into crystalline rocks produce about a hundred times more impact melt than impacts into sedimentary rocks. They attributed this difference to the effects of vaporization of volatiles in sedimentary rocks causing subsequent acceleration of the ejecta by volatile expansion.

Wohletz and Sheridan (1983) suggested that target water explosively vaporizes during impact resulting in an alteration in initial ballistic trajectories that ultimately

produce fluidized ejecta. They conducted a series of controlled steam explosion experiments by combining water and thermite. These steam explosions are very similar to hydrovolcanic eruptions in which hot magma comes in contact with liquid water and produces tuff rings, tuff cones, and ground surge deposits (Moore, 1967; Waters and Fisher, 1971; Wohletz and Sheridan, 1979). Results of their experiments indicate that the degree of thermite melt fragmentation (i.e., ejecta particle size), energy of the explosion, and style of the explosion are controlled by the mass ratio of water to thermite melt and confining pressure. Wohletz and Sheridan (1979) found that larger fragments followed parabolic paths while smaller ejecta particles experience significant aerodynamic drag due to their interaction with the atmosphere and steam produced during the explosion. This resulted in separation fine particles flowing as a ground surge from a ballistic plume comprised of larger particles.

Wohletz and Sheridan (1983) concluded that small water-melt ratios (0 – 0.2) produced ballistic style eruptions with and average ejecta size of 10^0 cm. Water-melt ratios of 0.2 – 1.0 produced a fluidized superheated steam eruption with average ejecta size of 10^{-4} cm. Average ejecta size increased to 10^{-2} cm with a water-melt ratio of 1.0 – 10.0; This water-melt ratio produced a combination of fluidized steam and ballistic ejecta. Water-melt ratios above 10.0 produced 10^1 cm ejecta particles deposited in a fluid flow. They attributed the increased particle size and decrease in transport energy (as indicated by eruption style) with increased amounts of water (>1.0 water-melt ratio) to quenching caused by the high heat capacity of water.

Stewart et al. (2001) conducted experiments and modeling of impacts onto ice-rock mixtures to quantify the effects of subsurface H_2O on ejecta distribution, rampart

and pedestal formation, and crater floor morphologies. They propose that various ejecta morphologies (SLE, DLE, and MLE) are produced by increasing amounts of ice. They found that the high volatility of H_2O modifies the crater formation process producing more vapor, higher ejection angles, fluidized ejecta blankets, and larger crater rim uplift.

Ice is much more compressible than rock. Therefore, about 4 times more energy is deposited in ice than rock during typical shock pressures (Stewart et al., 2001). Ejection angle increases as strength decreases (Melosh, 1984). Through their experiments, Stewart et al, (2001) found that ice will melt completely upon release from shock pressures $\geq$2-3 GPa. These pressures correspond to about 7 projectile radii (R_p) for asteroidal impacts on Mars (Stewart et al., 2001).

Stewart et al., (2001) modeled impacts into rock-ice mixture using the Eulerian finite difference code, CTH (McGlaun and Thomson, 1990), and found that ejection angles at the point of impact are high (70˚) and nearly constant in the zone of melted ice and brecciated rock ($7R_p$) for a rock-ice mixture with 20% volume subsurface ice. In contrast, pure rock targets had a peak ejection angle of about 60˚. In all experiments, the ejection angles decrease to about 45˚ near the crater rim. Models with peak ejection angles of 70˚ (consistent with 10-20% volume water ice) produced ejecta layers of consistent thickness that were high in water content. Models with initial ejection angles of about 80˚ corresponding to increased amounts of water produced an ejecta blanket that was more pronounced with a large step in ejecta thickness about 0.6 crater radii (*Rc*) from the rim.

O'Keefe et al. (2001) produced geologic strength models using shock wave physics code CTH (McGlaun and Thomson, 1990). They found that since ice is more

compressible than rock, more work was done on the ice. Consequently, a larger volume of ice was subjected to shock-induced phase transformations compared to the rocks. In their numerical model, a small zone of rock (~1 impactor radius, *a*) was melted and very little was vaporized (<1 *a*). Rock that was excavated did not undergo any major phase transitions. However, ice was vaporized to about 1*a* and ice was melted within about 7*a*. From 1*a* to 7*a*, the excavated material is a mixture of rock and water. Ejection angles are also high (70°) within this region and decrease away from the impact point until they reach a 45° angle near the crater rim. O'Keefe et al., (2001) note that there is a clear separation in ejecta trajectories in their model at about 7*a*. They attribute this separation to differences in strength between rock and water in the excavation cavity. They conclude that the ejecta will contain a significant amount of water allowing for fluidized flow.

To understand the amount of liquid water that was present in Martian ejecta blankets, Stewart et al. (2003) conducted simulations of impact cratering onto ice-rock mixtures using the shock physics code CTH (McGlaun and Thomson, 1990). They used the results of these simulations to calculate the volume of ground ice subject to shock-induced melting and the amount of excavated liquid water. They assumed the ground ice was distributed within pore spaces and cracks in the Martian regolith at average Martian surface temperatures (200 K). The atmosphere was approximated at the present day mean of 7 millibar. The surface porosity was varied from 0-20%. Regolith pore space volume (ϕ) was modeled assuming a decrease in depth, *z*, as $\phi_o e^{-z/Kz}$, where ϕ_0 is the surface porosity and Kz is the decay constant (3 km). The dynamic strength of the Martian surface was constrained to ~10 Mpa. Projectile diameter was varied from 100 to 2000 m.

At temperatures between 150 and 273 K, ice in the Martian crust will begin to melt after experiencing shock pressures between 2.0 and 0.6 GPa, respectively (Stewart et al., 2003). The ice will melt completely after being released from shock pressures above 5.5 and 3.7 GPa.

Stewart et al. (2003) concluded that, in the present climate, about half the excavated ice is melted by impact shock. About 60% of ground ice will completely melt in equatorial zones while at the poles more that 20% will be melted. Their results indicate that ejecta fluidization does not require pre-existing water near the surface because shock-melting of ground ice will introduce large quantities of liquid water into the ejecta blanket.

Conclusion

According to Barlow (2010), the relative role of subsurface volatiles versus the atmosphere in the formation of layered ejecta blankets is one of the major questions remaining concerning the geology of Mars. Barlow (2005) suggests that fluidized ejecta are produced by some combination of the atmospheric and subsurface volatile models. Building upon Schultz's (1992a) idea that ejecta can flow without water if the particles are small enough, this dissertation tests the hypothesis that the vaporization of water during the excavation stage of impact cratering is the mechanism that decreases the size of ejecta particles and facilitates its fluidized emplacement. It is proposed that this interaction between water and rock during decompression may be the bridge between the atmospheric and subsurface volatile models.

APPENDIX 3

PHASE EQUILIBRIA OF WATER AND CARBON DIOXIDE ONE- AND TWO-COMPONENT SYSTEMS AND THEIR RELATION TO THE MARTIAN SURFACE CONDITIONS AND PROPOSED EXPERIMENTS

This appendix describes the one- and two-component phase diagrams for CO_2 and H_2O, and how each relates to (1) atmospheric and regolith conditions on Mars, (2) pressure and temperature conditions during impact cratering, and (3) experiments on the effects of shock decompression of water on the degree of rock fragmentation conducted using the University of Munich shock tube apparatus.

One-component Phase Diagram for H_2O

The phase diagram of water (Figure 24a) shows three phases of water (liquid, vapor, and solid ice) separated by equilibrium curves. Any phase changes with changing pressure and/or temperature are governed by the Gibb's Phase Rule:

$P + F = C + I$

Where

> P = the number of phases (solid, liquid, or gas) in the system
> C = the minimum number of components necessary to define the system
> I = the number of intensive variables in the system. Intensive variables are properties of the system that are not dependent on the amount of material in the system. In the phase diagrams discussed below, the intensive variables are pressure and temperature.
> F = degrees of freedom of the system

Each field (solid, liquid, gas) is a divariant field where there are two degrees of freedom ($F = C+I-P=1+2-1=2$). We can change temperature and/or pressure without any phase changes and still maintain equilibrium. The three curves on the phase diagram

represent conditions under which two phases exist in equilibrium. Along these univariant curves there is one degree of freedom (F=C+I-P=1+2-2=1). This means that, in order to maintain equilibrium between the two phases, we can change pressure or temperature independently, but not both. If we change pressure, temperature must change along the univariant curve. If we change temperature, pressure can only change along the univariant curve if the system is to maintain equilibrium between the two phases. The system can only move off of these curves and maintain equilibrium if one of the phases is consumed.

At the triple point, all three phases (solid, liquid, and vapor) exist in equilibrium. At this point there are zero degrees of freedom (F=C+I-P=1+2-3=0). The system will not move off this point until one or two phases are consumed.

The phase diagram for water shows that at low temperatures, ice (solid water) is the stable phase. At moderate temperatures and high pressures, water (liquid) is the stable phase, and at higher temperatures and lower pressures, water vapor (gas) is the stable phase. The sublimation curve separating solid and gas phases represents the vapor pressure of ice as a function of temperature. The vaporization curve separating the liquid and gas phases is a plot of (equilibrium) vapor pressure P as a function of temperature T. The triple point (273 K, 1kPa) represents the point at which vapor pressures for ice and water are the same and all three phases (ice, water, and vapor) coexist. The temperature and pressure are fixed at this point.

The critical point (674 K, ~8Pa) is a point beyond which water cannot be liquefied. Because this super-critical fluid shares the properties of gas, no vapor pressure

beyond this temperature is measured. The temperature of 647 K is called the critical temperature, and the vapor pressure at this temperature is called the critical pressure.

The melting curve or fusion curve separates the liquid and solid phases. Note that the slope of this curve is negative for water. This is due to the unique property that solid water is less dense than liquid water. Ice actually melts at lower temperature at higher pressure.

The slope of any phase change curve can be described by the Claussius-Clapeyron equation which relates the slope of a reaction line on a phase diagram to fundamental thermodynamic properties. The form of the Clapeyron equation most often used is:

$dP/dT = \Delta S/\Delta V$
where:
P = pressure
T = temperature
S = entropy
V = volume

This equations states that the slope (rise/run) of an univariant equilibrium curve plotted on a P-T diagram is equal to the entropy change (ΔS) of the reaction divided by the volume change (ΔV) of the reaction. So for a melting curve with a positive slope (e.g., carbon dioxide system), entropy (or disorder) increases as volume increases.

Carbon dioxide molecules are more disordered in liquid form than solid form. Liquid carbon dioxide is less dense than solid carbon dioxide and takes up more volume.

But water is unique in that ice, the more ordered (lower entropy) form, has a larger volume than less ordered (higher entropy) liquid water. Entropy decreases and volume increases and the melting curve between ice and water has a negative slope.

One-component Phase Diagram for CO_2

The phase diagrams for CO_2 has features in common with that of water: sublimation curve, vaporization curve, triple point, critical temperature and pressure. The triple point of carbon dioxide occurs at a pressure of 5.2 atm (3952 torr) and 216.6 K (-56.4 °C). At temperature of 197.5 K (-78.5 °C), the vapor pressure of solid carbon dioxide is 1 atm (760 torr). At this pressure, the liquid phase is not stable, the solid simply sublimates. Solid carbon dioxide is called dry ice, because it does not go through a liquid state in its phase transition at average surface pressures and temperatures on Earth. The critical temperature for carbon dioxide is 31.1 °C, and the critical pressure is 73 atm. Above the critical temperature, the carbon dioxide is a super-critical fluid. Figures 24a and 25a show the average surface conditions for Earth (E), Venus (V, Figure 24a only), and Mars (M). On Earth, water is most commonly found as a liquid while carbon dioxide is a gas. The surface of Venus is within the stability field for gaseous water and carbon dioxide. Water ice and carbon dioxide gas are most commonly found at average surface temperatures and pressures on Mars, although some solid carbon dioxide may be found at the poles.

Isobaric Heating Example: Water

Let's look at example of isobaric (holding pressure fixed) heating of water ice. Our sample of ice at point A (~180 K [~ -93.15 °C], 1 bar) is in the solid field with two degrees of freedom. As we add heat to the system while keeping pressure fixed, the system will evolve to the right toward the melting curve at point B (~280 K [~ 6.85 °C], 1 bar). Once it hits the melting curve, the system will have one degree of freedom and must stay along this curve until one of the phases disappears. Because we are holding

pressure fixed while adding heat, the system will stay at this point until all the ice is melted into water. Even though the ice is melting as heat is being added, temperature of the system will remain the same because the heat is being used to break the bonds of the crystalline ice structure. Once all the ice has melted, the system will continue to move to the right (increasing temperature while maintaining the same pressure) toward point C (~300 K [~ 26.85 °C], 1 bar). The rate at which the ice melts is controlled by the heating rate. Because we have lost a phase (ice) we are once again in a divarant field, this time for liquid water.

Isothermal Decompression Example: Carbon Dioxide

Now let's look at what happens when we hold temperature constant and change pressure. In this example we will consider isothermic decompression of solid carbon dioxide. We'll start with sample X (~210 K [~ -63.15 °C], 1 bar). This sample is in the divariant solid field for CO_2. As we reduce the pressure, the system evolves down toward the sublimation curve at point Y (~210 K [~ -63.15 °C], 0.3 bar). Along this curve solid and gas coexist in equilibrium and there is one degree of freedom. Any change in pressure must be followed by a change in temperature that is restricted to the sublimation curve if the system is to remain in equilibrium. However, we are holding temperature fixed. Therefore, the system sits at point Y while the change in pressure converts the solid CO_2 to gas. The rate at which the solid sublimates depends on the decompression rate. The more quickly the system is decompressed, the more explosive the transition from solid to gas will be. Once we have lost the solid phase, isobaric decompression will continue to push the sample down toward point Z (~210 K [~ -63.15 °C], 0.8 bar).

Two-component Phase Diagram for H_2O-CO_2

Figure 26, shows the phase diagram for the H_2O-CO_2 two-component system. This figure includes the stability fields for clathrate hydrate assembled by Longhi (2006) from experimental work and thermodynamic calculations. Clathrate hydrates are solids in which hydrogen-bonded water molecules form cage-like structures that enclose low-molecular-weight gases (i.e., O_2, N_2, CO_2, CH_4, H_2S, Ar, Kr, and Xe). In this example, clathrate hydrate encloses CO_2 molecules. Clathrate hydrates are stable under particular pressure and temperature conditions (depending on the gas molecule enclosed). If pressure and temperature conditions stray outside this range, the enclosed gas molecule will escape the cage and the cage will collapse into a conventional ice structure (Longhi 2006).

Martian Surface and Subsurface Conditions

The average surface pressure and temperature conditions are shown for Earth (blue dot) and Mars (red dot) in Figure 27. The Martian geothermal gradient for a closed regolith is shown as a red line (Longhi 2006). Under closed regolith conditions, near the surface, water ice and CO_2 gas can exist. With increased depth (pressure), clathrate hydrate forms. At even greater pressures, solid water ice may exist with solid and/or liquid CO_2. At depths between about 1 and 4 km, water ice exists with liquid CO_2. At depths of about 4 to 5 km, liquid CO_2 may exist with liquid water.

Longhi (2006) showed that the regolith gas thermal gradient is the intersection of isobars from the atmospheric gradient projected within the regolith with isotherms from the lithostatic gradient (Figure 27). Regolith pores are most likely to be open to the atmosphere closer to the poles because ice near the poles seals the regolith off from the atmosphere.

Pressure Temperature Conditions Reached During Impact

During the contact/compression stage of impact cratering, target materials can experience temperatures up to 10,000 °C near the impact point and from 500 to 3000 °C in the surrounding rock (de Pater and Lissauer 2001, French 1998, and Melosh 1989). Rocks near the point of impact are shocked to over 100 GPa of pressure (French 1998, Melosh 1989). Pressures decrease away from the point of impact to about 10 - 30 GPa about one-crater radii from impact (French 1998, Melosh 1989). These high pressures are rapidly released within less than a second. At this point, the excavation stage begins, during which rocks are fragmented and typically are ballistically emplaced as ejecta (French 1998, Melosh 1989).

Figure 26 shows the peak temperatures and pressures reached during the contact/compression stage of impact cratering plotted against a phase diagram for water. No matter what the starting phase of water is in the Martian regolith, water will be forced into a complex solid, liquid, or supercritical fluid phase. During the excavation stage, these high pressures will be released to essentially zero, and water will flash to a vapor.

Application of water and CO_2 Phase Diagrams to Rock Fragmentation Experiments

These phase diagrams have important implications for this research and are used to plan the temperature and pressure conditions of the experiments. In this section, I'll describe the experiments and how the phase diagrams were used to determine experimental conditions.

The University of Munich has an experimental facility for the investigation of rock fragmentation by rapid decompression (Figure 5, Alidibirov and Dingwell 1996a, Küppers et al. 2006). This facility was used to test effect of rapid decompression of water on the fragmentation of rock. The experimental apparatus consists of a high-pressure, high-temperature section separated by a diaphragm from a low-pressure, low-temperature section (Alidibirov and Dingwell 1996a, Küppers et al. 2006). The high-pressure section can reach pressures of 500 bars (50 MPa) and temperatures of 950 °C (Spieler 2007, pers. comm.). When the diaphragm separating the two sections is broken, the pressure in the lower chamber rapidly drops to ~1 atm. A release wave propagates through the sample at the speed of sound (Figures 5, Alidibirov and Dingwell 1996b, Küppers et al. 2006), generating dynamic tensile stresses in the sample. If the dynamic tensile strength of the sample is exceeded by the release wave, fracturing and fragmentation will occur. Compressed gas contained in the pore spaces of the sample will expand and accelerate the fragments. Temperatures and pressures experienced by rocks during impact far exceed those of the experimental facility. However, this study is not intended to simulate the exact conditions during impacts. Rather, the purpose of this

study is to investigate whether the rapid decompression of water increases the degree of rock fragmentation.

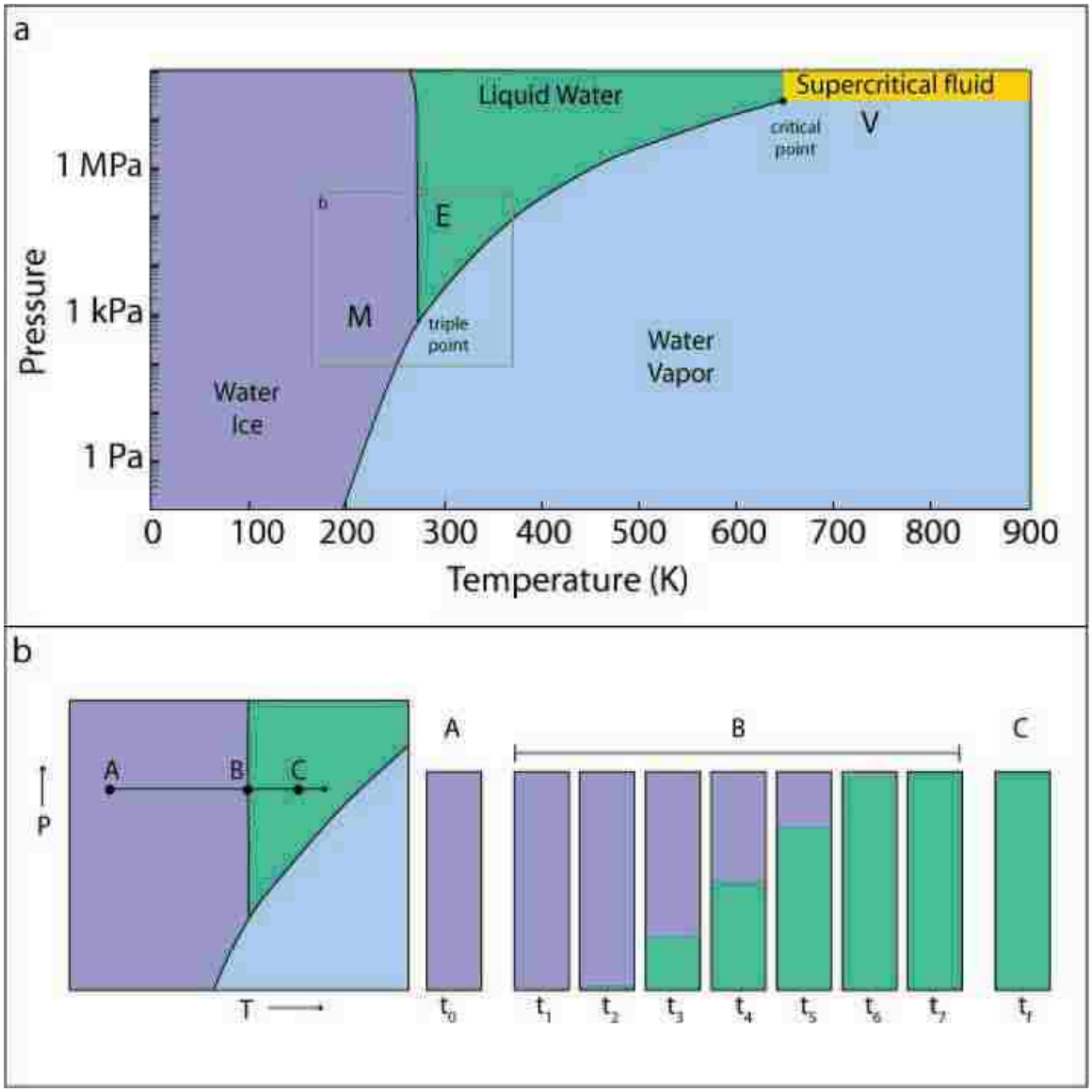

Figure 24. Isobaric heating of water ice. The average surface pressure and temperature conditions for Earth (E) and Mars (M) are shown.

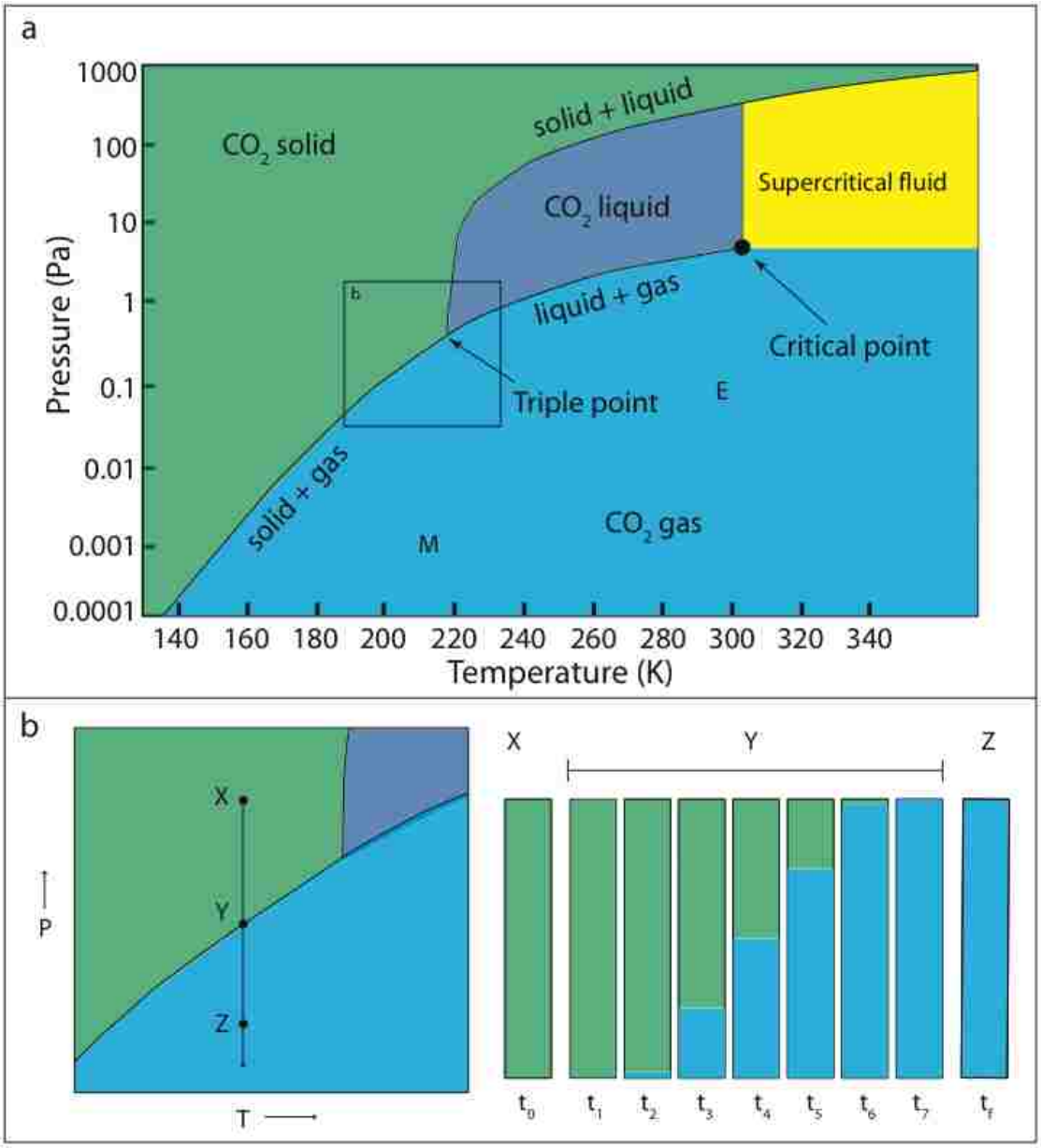

Figure 25. Isothermal decompression of CO_2.The average surface pressure and temperature conditions for Earth (E) and Mars (M) are shown.

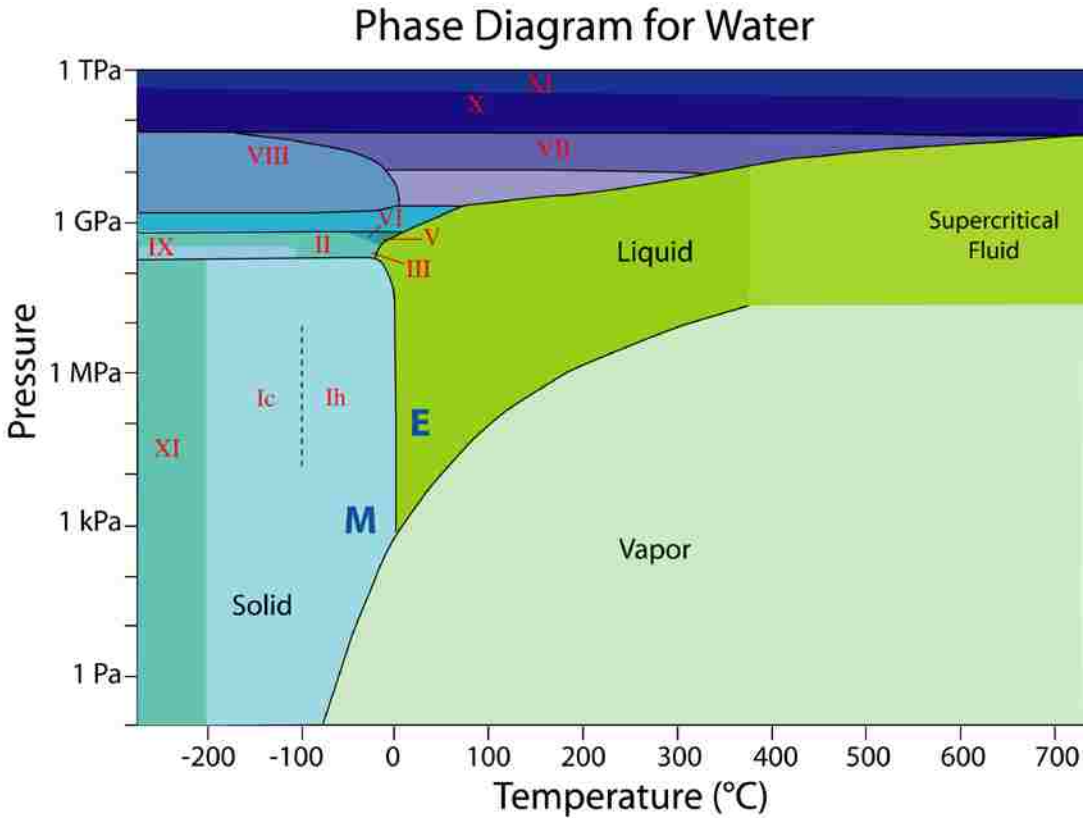

Figure 26. Phase diagram for water.

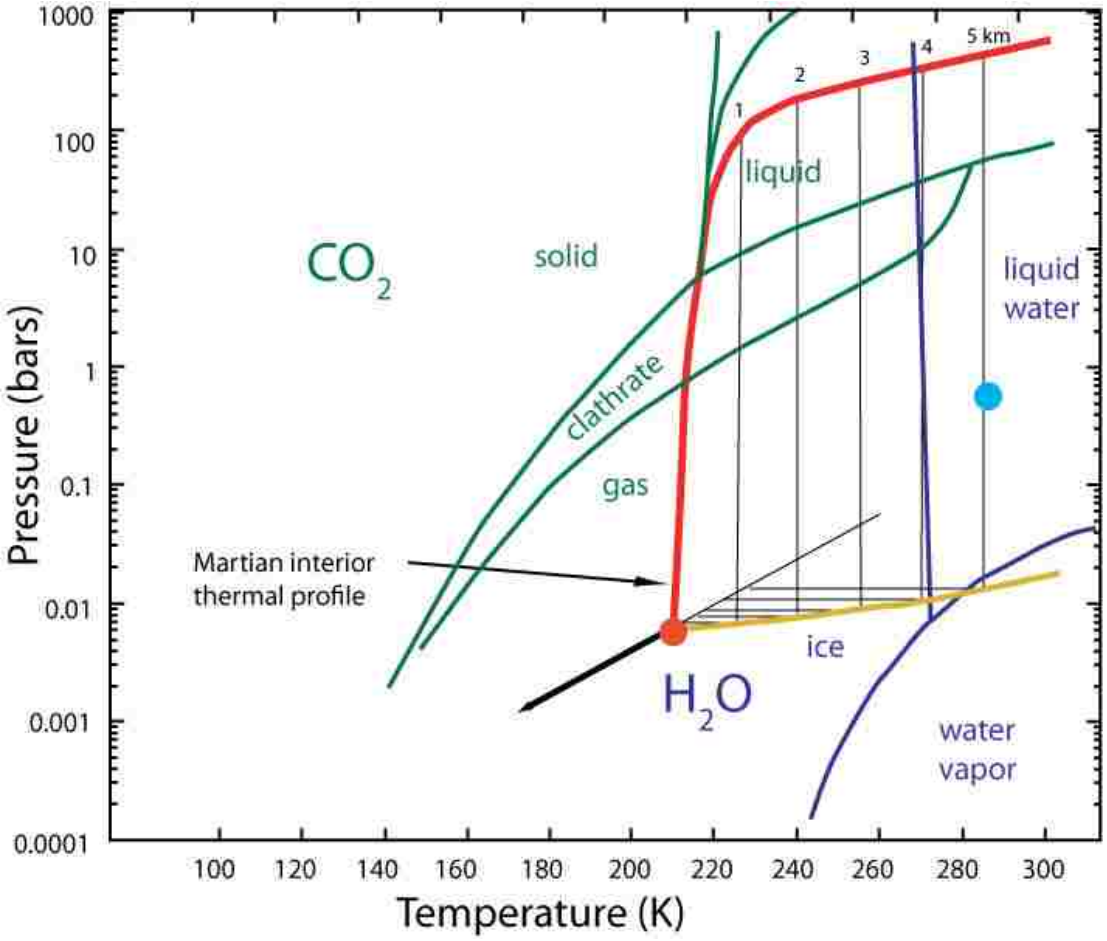

Figure 27. Two component phase diagram for H_2O and CO_2. Average surface temperature and pressure conditions are shown for Earth (blue dot) and Mars (red dot). Geothermal gradients for a closed (red line) and open (yellow line) Martian regolith are also shown (Adapted from Longhi 2006).

APPENDIX 4

SIEVING RESULTS

Table 5. Sieving results for sample 102.

Sample No.	Sieve size ϕ	Sieve midpoint ϕ	Weight g	Frequency Wt. %	Cumulative Wt. %
102	-6.00	-6.25	0.0000	0.0000	0.0000
	-5.50	-5.75	0.0000	0.0000	0.0000
	-5.00	-5.25	0.0000	0.0000	0.0000
	-4.50	-4.75	0.0000	0.0000	0.0000
	-4	-4.25	0.0000	0.0000	0.0000
	-3.5	-3.75	0.0000	0.0000	0.0000
	-3	-3.25	0.4254	1.1247	1.1247
	-2.5	-2.75	2.1397	5.6569	6.7815
	-2	-2.25	5.8815	15.5493	22.3309
	-1.5	-1.75	6.4723	17.1113	39.4421
	-1	-1.25	6.1721	16.3176	55.7597
	-0.5	-0.75	5.1205	13.5374	69.2971
	0	-0.25	2.8885	7.6365	76.9337
	0.5	0.25	1.8171	4.8040	81.7376
	1	0.75	1.6621	4.3942	86.1319
	1.5	1.25	1.2735	3.3668	89.4987
	2	1.75	0.9298	2.4582	91.9569
	2.5	2.25	0.7823	2.0682	94.0251
	3	2.75	0.4398	1.1627	95.1878
	3.5	3.25	0.4238	1.1204	96.3082
	4	3.75	0.505	1.3351	97.6433
	4.5	4.25	0.8914	2.3567	100.0000

Table 6. Sieving results for sample 103.

Sample No.	Sieve size ϕ	Sieve midpoint ϕ	Weight g	Frequency Wt. %	Cumulative Wt. %
103	-6.00	-6.25	28.671	85.2013	85.2013
	-5.50	-5.75	0.000	0.0000	85.2013
	-5.00	-5.25	0.000	0.0000	85.2013
	-4.50	-4.75	0.000	0.0000	85.2013
	-4.00	-4.25	0.000	0.0000	85.2013
	-3.50	-3.75	0.000	0.0000	85.2013
	-3.00	-3.25	0.000	0.0000	85.2013
	-2.50	-2.75	0.349	1.0368	86.2382
	-2.00	-2.25	1.041	3.0920	89.3302
	-1.50	-1.75	0.806	2.3946	91.7248
	-1.00	-1.25	0.857	2.5479	94.2727
	-0.50	-0.75	0.626	1.8612	96.1339
	0.00	-0.25	0.442	1.3120	97.4459
	0.50	0.25	0.279	0.8294	98.2753
	1.00	0.75	0.194	0.5756	98.8508
	1.50	1.25	0.128	0.3804	99.2312
	2.00	1.75	0.078	0.2330	99.4642
	2.50	2.25	0.066	0.1967	99.6609
	3.00	2.75	0.047	0.1391	99.8000
	3.50	3.25	0.034	0.1007	99.9007
	4.00	3.75	0.025	0.0740	99.9747
	4.50	4.25	0.008	0.0253	100.0000

Table 7. Sieving results for sample 104.

Sample No.	Sieve size ϕ	Sieve midpoint ϕ	Weight g	Frequency Wt. %	Cumulative Wt. %
104	-6.00	-6.25	0.000	0.0000	0.0000
	-5.50	-5.75	0.000	0.0000	0.0000
	-5.00	-5.25	0.000	0.0000	0.0000
	-4.50	-4.75	0.000	0.0000	0.0000
	-4.00	-4.25	0.000	0.0000	0.0000
	-3.50	-3.75	0.000	0.0000	0.0000
	-3.00	-3.25	0.156	0.4618	0.4618
	-2.50	-2.75	0.815	2.4167	2.8785
	-2.00	-2.25	4.935	14.6363	17.5148
	-1.50	-1.75	6.118	18.1472	35.6620
	-1.00	-1.25	5.772	17.1185	52.7805
	-0.50	-0.75	5.592	16.5861	69.3667
	0.00	-0.25	2.792	8.2797	77.6464
	0.50	0.25	1.966	5.8301	83.4764
	1.00	0.75	1.499	4.4470	87.9234
	1.50	1.25	0.870	2.5814	90.5048
	2.00	1.75	0.572	1.6954	92.2002
	2.50	2.25	0.485	1.4373	93.6375
	3.00	2.75	0.328	0.9732	94.6107
	3.50	3.25	0.039	0.1169	94.7276
	4.00	3.75	0.015	0.0436	94.7712
	4.50	4.25	1.763	5.2288	100.0000

Table 8. Sieving results for sample 105.

Sample No.	Sieve size ϕ	Sieve midpoint ϕ	Weight g	Frequency Wt. %	Cumulative Wt. %
105	-6.00	-6.25	30.008	90.7406	90.7406
	-5.50	-5.75	0.000	0.0000	90.7406
	-5.00	-5.25	0.000	0.0000	90.7406
	-4.50	-4.75	0.000	0.0000	90.7406
	-4.00	-4.25	0.000	0.0000	90.7406
	-3.50	-3.75	0.000	0.0000	90.7406
	-3.00	-3.25	0.000	0.0000	90.7406
	-2.50	-2.75	0.000	0.0000	90.7406
	-2.00	-2.25	0.000	0.0000	90.7406
	-1.50	-1.75	0.000	0.0000	90.7406
	-1.00	-1.25	0.618	1.8676	92.6081
	-0.50	-0.75	0.913	2.7611	95.3692
	0.00	-0.25	0.482	1.4578	96.8270
	0.50	0.25	0.326	0.9861	97.8131
	1.00	0.75	0.233	0.7031	98.5162
	1.50	1.25	0.183	0.5543	99.0705
	2.00	1.75	0.108	0.3251	99.3955
	2.50	2.25	0.084	0.2544	99.6499
	3.00	2.75	0.056	0.1689	99.8188
	3.50	3.25	0.032	0.0963	99.9150
	4.00	3.75	0.021	0.0634	99.9785
	4.50	4.25	0.007	0.0215	100.0000

Table 9. Sieving results for sample 108.

Sample No.	Sieve size ϕ	Sieve midpoint ϕ	Weight g	Frequency Wt. %	Cumulative Wt. %
108	-6.00	-6.25	0.0000	0.0000	0.0000
	-5.50	-5.75	0.0000	0.0000	0.0000
	-5.00	-5.25	0.0000	0.0000	0.0000
	-4.50	-4.75	0.0000	0.0000	0.0000
	-4.00	-4.25	0.0000	0.0000	0.0000
	-3.50	-3.75	0.0000	0.0000	0.0000
	-3.00	-3.25	0.0000	0.0000	0.0000
	-2.50	-2.75	0.0000	0.0000	0.0000
	-2.00	-2.25	0.2259	0.7534	0.7534
	-1.50	-1.75	1.0407	3.4708	4.2242
	-1.00	-1.25	2.3172	7.7281	11.9523
	-0.50	-0.75	3.2206	10.7410	22.6933
	0.00	-0.25	5.0315	16.7805	39.4738
	0.50	0.25	4.4922	14.9819	54.4557
	1.00	0.75	3.5939	11.9860	66.4417
	1.50	1.25	1.8495	6.1682	72.6099
	2.00	1.75	1.7438	5.8157	78.4256
	2.50	2.25	1.1703	3.9031	82.3287
	3.00	2.75	1.1631	3.8790	86.2077
	3.50	3.25	0.5666	1.8897	88.0974
	4.00	3.75	1.3423	4.4767	92.5741
	4.50	4.25	2.2266	7.4259	100.0000

Table 10. Sieving results for sample 109.

Sample No.	Sieve size ϕ	Sieve midpoint ϕ	Weight g	Frequency Wt. %	Cumulative Wt. %
109	-6.00	-6.25	0.000	0.0000	0.0000
	-5.50	-5.75	0.000	0.0000	0.0000
	-5.00	-5.25	0.000	0.0000	0.0000
	-4.50	-4.75	0.000	0.0000	0.0000
	-4.00	-4.25	0.000	0.0000	0.0000
	-3.50	-3.75	0.000	0.0000	0.0000
	-3.00	-3.25	0.000	0.0000	0.0000
	-2.50	-2.75	0.000	0.0000	0.0000
	-2.00	-2.25	0.344	1.0394	1.0394
	-1.50	-1.75	1.521	4.5959	5.6353
	-1.00	-1.25	3.106	9.3852	15.0205
	-0.50	-0.75	5.880	17.7678	32.7883
	0.00	-0.25	5.679	17.1601	49.9485
	0.50	0.25	4.322	13.0604	63.0089
	1.00	0.75	3.438	10.3884	73.3973
	1.50	1.25	1.914	5.7828	79.1800
	2.00	1.75	1.186	3.5849	82.7649
	2.50	2.25	0.928	2.8032	85.5681
	3.00	2.75	0.704	2.1263	87.6944
	3.50	3.25	0.504	1.5235	89.2179
	4.00	3.75	0.489	1.4776	90.6955
	4.50	4.25	3.079	9.3045	100.0000

Table 11. Sieving results for sample 110.

Sample No.	Sieve size ϕ	Sieve midpoint ϕ	Weight g	Frequency Wt. %	Cumulative Wt. %
110	-6.00	-6.25	0.000	0.0000	0.0000
	-5.50	-5.75	0.000	0.0000	0.0000
	-5.00	-5.25	0.000	0.0000	0.0000
	-4.50	-4.75	0.000	0.0000	0.0000
	-4.00	-4.25	0.000	0.0000	0.0000
	-3.50	-3.75	0.000	0.0000	0.0000
	-3.00	-3.25	0.000	0.0000	0.0000
	-2.50	-2.75	0.1878	0.5714	0.5714
	-2.00	-2.25	1.9723	6.0009	6.5722
	-1.50	-1.75	3.5268	10.7305	17.3028
	-1.00	-1.25	4.0713	12.3872	29.6900
	-0.50	-0.75	4.574	13.9167	43.6067
	0.00	-0.25	4.3756	13.3130	56.9197
	0.50	0.25	3.5637	10.8428	67.7625
	1.00	0.75	2.8431	8.6503	76.4128
	1.50	1.25	1.5787	4.8033	81.2161
	2.00	1.75	0.9699	2.9510	84.1671
	2.50	2.25	0.7652	2.3282	86.4953
	3.00	2.75	0.5792	1.7623	88.2575
	3.50	3.25	0.3971	1.2082	89.4657
	4.00	3.75	0.3424	1.0418	90.5075
	4.50	4.25	3.1199	9.4925	100.0000

Table 12. Sieving results for sample 112.

Sample No.	Sieve size ϕ	Sieve midpoint ϕ	Weight g	Frequency Wt. %	Cumulative Wt. %
112	-6.00	-6.25	0.000	0.0000	0.0000
	-5.50	-5.75	0.000	0.0000	0.0000
	-5.00	-5.25	0.000	0.0000	0.0000
	-4.50	-4.75	0.000	0.0000	0.0000
	-4.00	-4.25	0.000	0.0000	0.0000
	-3.50	-3.75	1.6882	5.3182	5.3182
	-3.00	-3.25	3.5903	11.3102	16.6283
	-2.50	-2.75	2.863	9.0190	25.6474
	-2.00	-2.25	1.9044	5.9992	31.6466
	-1.50	-1.75	2.7549	8.6785	40.3251
	-1.00	-1.25	2.6557	8.3660	48.6911
	-0.50	-0.75	2.5988	8.1867	56.8778
	0.00	-0.25	3.1926	10.0573	66.9352
	0.50	0.25	2.1219	6.6844	73.6196
	1.00	0.75	1.8324	5.7724	79.3920
	1.50	1.25	0.9765	3.0762	82.4682
	2.00	1.75	0.9509	2.9955	85.4637
	2.50	2.25	1.0823	3.4095	88.8732
	3.00	2.75	0.7259	2.2867	91.1599
	3.50	3.25	0.6468	2.0376	93.1975
	4.00	3.75	0.9441	2.9741	96.1716
	4.50	4.25	1.2153	3.8284	100.0000

Table 13. Sieving results for sample 113.

Sample No.	Sieve size ϕ	Sieve midpoint ϕ	Weight g	Frequency Wt. %	Cumulative Wt. %
113	-6.00	-6.25	0.000	0.0000	0.0000
	-5.50	-5.75	0.000	0.0000	0.0000
	-5.00	-5.25	0.000	0.0000	0.0000
	-4.50	-4.75	0.000	0.0000	0.0000
	-4.00	-4.25	0.000	0.0000	0.0000
	-3.50	-3.75	4.2342	13.2430	13.2430
	-3.00	-3.25	2.8611	8.9485	22.1915
	-2.50	-2.75	5.7943	18.1224	40.3139
	-2.00	-2.25	3.7942	11.8669	52.1807
	-1.50	-1.75	3.8768	12.1252	64.3059
	-1.00	-1.25	2.7372	8.5609	72.8669
	-0.50	-0.75	2.0717	6.4795	79.3464
	0.00	-0.25	1.7566	5.4940	84.8404
	0.50	0.25	1.0515	3.2887	88.1291
	1.00	0.75	0.921	2.8805	91.0096
	1.50	1.25	0.4435	1.3871	92.3967
	2.00	1.75	0.3564	1.1147	93.5114
	2.50	2.25	0.1565	0.4895	94.0009
	3.00	2.75	0.3877	1.2126	95.2135
	3.50	3.25	0.2133	0.6671	95.8806
	4.00	3.75	0.589	1.8422	97.7228
	4.50	4.25	0.7281	2.2772	100.0000

Table 14. Sieving results for sample 114.

Sample No.	Sieve size ϕ	Sieve midpoint ϕ	Weigh g	Frequency Wt. %	Cumulative Wt. %
114	-6.00	-6.25	0.000	0.0000	0.0000
	-5.50	-5.75	0.000	0.0000	0.0000
	-5.00	-5.25	0.000	0.0000	0.0000
	-4.50	-4.75	0.000	0.0000	0.0000
	-4.00	-4.25	0.000	0.0000	0.0000
	-3.50	-3.75	0.000	0.0000	0.0000
	-3.00	-3.25	0.000	0.0000	0.0000
	-2.50	-2.75	2.0651	6.2291	6.2291
	-2.00	-2.25	3.9906	12.0371	18.2661
	-1.50	-1.75	3.9709	11.9776	30.2438
	-1.00	-1.25	4.9134	14.8206	45.0643
	-0.50	-0.75	5.2679	15.8899	60.9542
	0.00	-0.25	3.5846	10.8124	71.7666
	0.50	0.25	2.5497	7.6908	79.4574
	1.00	0.75	1.9481	5.8762	85.3336
	1.50	1.25	1.1116	3.3530	88.6866
	2.00	1.75	0.7095	2.1401	90.8267
	2.50	2.25	0.5698	1.7187	92.5454
	3.00	2.75	0.4499	1.3571	93.9024
	3.50	3.25	0.2957	0.8919	94.7944
	4.00	3.75	0.2905	0.8763	95.6706
	4.50	4.25	1.4353	4.3294	100.0000

Table 15. Sieving results for sample 416.

Sample No.	Sieve size ϕ	Sieve midpoint ϕ	Weight g	Frequency Wt. %	Cumulative Wt. %
416	-6.00	-6.25	0.000	0.0000	0.0000
	-5.50	-5.75	0.000	0.0000	0.0000
	-5.00	-5.25	0.000	0.0000	0.0000
	-4.50	-4.75	0.000	0.0000	0.0000
	-4.00	-4.25	0.000	0.0000	0.0000
	-3.50	-3.75	0.000	0.0000	0.0000
	-3.00	-3.25	0.000	0.0000	0.0000
	-2.50	-2.75	0.102	0.2905	0.2905
	-2.00	-2.25	1.964	5.5716	5.8621
	-1.50	-1.75	3.298	9.3573	15.2194
	-1.00	-1.25	4.243	12.0365	27.2559
	-0.50	-0.75	5.498	15.5973	42.8532
	0.00	-0.25	4.544	12.8919	55.7451
	0.50	0.25	4.125	11.7038	67.4488
	1.00	0.75	3.591	10.1880	77.6368
	1.50	1.25	2.781	7.8891	85.5259
	2.00	1.75	1.641	4.6558	90.1817
	2.50	2.25	0.867	2.4597	92.6414
	3.00	2.75	0.563	1.5967	94.2381
	3.50	3.25	0.650	1.8435	96.0815
	4.00	3.75	0.787	2.2339	98.3154
	4.50	4.25	0.594	1.6846	100.0000

Table 16. Sieving results for sample 417.

Sample No.	Sieve size ϕ	Sieve midpoint ϕ	Weight g	Frequency Wt. %	Cumulative Wt. %
417	-6.00	-6.25	0.0000	0.0000	0.0000
	-5.50	-5.75	0.0000	0.0000	0.0000
	-5.00	-5.25	0.0000	0.0000	0.0000
	-4.50	-4.75	0.0000	0.0000	0.0000
	-4.00	-4.25	0.0000	0.0000	0.0000
	-3.50	-3.75	0.0000	0.0000	0.0000
	-3.00	-3.25	0.0000	0.0000	0.0000
	-2.50	-2.75	0.0000	0.0000	0.0000
	-2.00	-2.25	5.8815	16.6805	16.6805
	-1.50	-1.75	6.4723	18.3561	35.0366
	-1.00	-1.25	6.1721	17.5047	52.5413
	-0.50	-0.75	5.1205	14.5222	67.0635
	0.00	-0.25	2.8885	8.1921	75.2556
	0.50	0.25	1.8171	5.1535	80.4091
	1.00	0.75	1.6621	4.7139	85.1230
	1.50	1.25	1.2735	3.6118	88.7347
	2.00	1.75	0.9298	2.6370	91.3717
	2.50	2.25	0.7823	2.2187	93.5904
	3.00	2.75	0.4398	1.2473	94.8377
	3.50	3.25	0.4238	1.2019	96.0397
	4.00	3.75	0.5050	1.4322	97.4719
	4.50	4.25	0.8914	2.5281	100.0000

Table 17. Sieving results for sample 422.

Sample No.	Sieve size ϕ	Sieve midpoint ϕ	Weight g	Frequency Wt. %	Cumulative Wt. %
422	-6.00	-6.25	0.0000	0.0000	0.0000
	-5.50	-5.75	0.0000	0.0000	0.0000
	-5.00	-5.25	0.0000	0.0000	0.0000
	-4.50	-4.75	0.0000	0.0000	0.0000
	-4.00	-4.25	0.0000	0.0000	0.0000
	-3.50	-3.75	0.0000	0.0000	0.0000
	-3.00	-3.25	0.0000	0.0000	0.0000
	-2.50	-2.75	1.8991	5.6873	5.6873
	-2.00	-2.25	4.5516	13.6309	19.3182
	-1.50	-1.75	5.2949	15.8568	35.1750
	-1.00	-1.25	5.5972	16.7621	51.9371
	-0.50	-0.75	3.667	10.9817	62.9189
	0.00	-0.25	3.3759	10.1099	73.0288
	0.50	0.25	2.1837	6.5396	79.5684
	1.00	0.75	2.4821	7.4332	87.0016
	1.50	1.25	1.3443	4.0258	91.0275
	2.00	1.75	0.9061	2.7135	93.7410
	2.50	2.25	0.6628	1.9849	95.7259
	3.00	2.75	0.3638	1.0895	96.8154
	3.50	3.25	0.16	0.4792	97.2946
	4.00	3.75	0.211	0.6319	97.9264
	4.50	4.25	0.6924	2.0736	100.0000

Table 18. Sieving results for sample 426.

Sample No.	Sieve size ϕ	Sieve midpoint ϕ	Weight g	Frequency Wt. %	Cumulative Wt. %
426	-6.00	-6.25	0.0000	0.0000	0.0000
	-5.50	-5.75	0.0000	0.0000	0.0000
	-5.00	-5.25	0.0000	0.0000	0.0000
	-4.50	-4.75	0.0000	0.0000	0.0000
	-4.00	-4.25	0.0000	0.0000	0.0000
	-3.50	-3.75	1.1069	3.8522	3.8522
	-3.00	-3.25	0.0000	0.0000	3.8522
	-2.50	-2.75	0.0000	0.0000	3.8522
	-2.00	-2.25	0.0000	0.0000	3.8522
	-1.50	-1.75	0.5306	1.8466	5.6988
	-1.00	-1.25	1.5478	5.3866	11.0854
	-0.50	-0.75	2.5809	8.9819	20.0673
	0.00	-0.25	4.7969	16.6940	36.7613
	0.50	0.25	4.1411	14.4117	51.1730
	1.00	0.75	3.6764	12.7945	63.9675
	1.50	1.25	1.6135	5.6152	69.5827
	2.00	1.75	1.4736	5.1284	74.7111
	2.50	2.25	1.6187	5.6333	80.3444
	3.00	2.75	0.8858	3.0827	83.4271
	3.50	3.25	0.9685	3.3705	86.7977
	4.00	3.75	2.4307	8.4592	95.2569
	4.50	4.25	1.3629	4.7431	100.0000

VITA

Graduate College
University of Nevada, Las Vegas

Audrey Hughes Rager

Degrees

Bachelor of Arts, Anthropology, 1989
University of Colorado, Boulder

Master of Science, Earth Science, 2003
Emporia State University

Special Honors and Awards

Nevada Space Grant Fellowship
Fall 2004, Spring 2005, Fall 2005, Spring 2006, Spring 2007, Fall 2008
Bernarda E. French Scholarship
Barton Family Scholarship
UNLV Graduate and Professional Student Association Grant
Desert Space Grant
JPL/NASA Planetary Science Summer School, 2005

Publications

Rager, A. H., Scheu, B.E., Smith, E.I., and Dingwell, D.B, (Submitted), The effects of water vaporization on rock fragmentation during rapid decompression: Implications for the formation of fluidized ejecta on Mars, *Submitted to GSA Bulletin, December 2010.

Rager, A. H., Scheu, B.E., Smith, E.I., and Dingwell, D.B, (Submitted), How water in open pore space affects the fragmentation threshold of rocks: Implications for double layer ejecta formation, *Submitted to Journal of Geophysical Research Planets (E), December 2010.

Rager, A. H., Scheu, B.E., Smith, E.I., and Dingwell, D.B., 2009, The effect of water content on rock fragmentation during rapid decompression: Preliminary results and possible implications for the formation of fluidized ejecta, *in* Geological Society of America, Portland, OR.

Rager, A., and Smith, E., 2009, The effect of rapid decompression of volatiles on grain-size distribution: Implications for the morphology of Martian impact craters and water content of the target *in* UNLV Graduate and Professional Student Research Forum, March 28, 2009.

Rager, A., Smith, E., and Scheu, B., 2009, The effect of water content on rock fragmentation during rapid decompression: Implications for subsurface water content and fluidized ejecta on Mars *in* Fourth Annual Geosymposium, UNLV

Department of Geoscience, April 17, 2009.

Rager, A., 2008, Grain-size distribution studies on Martian blueberries: A reinterpretation of the geology of Meridiani Planum *in* UNLV Graduate and Professional Student Research Forum, March 29, 2008.

Rager, A., 2008, Grain-size distribution studies on Martian blueberries: A reinterpretation of the geology of Meridiani Planum and a model for the formation of fluidized ejecta *in* Third Annual Geosymposium, UNLV Department of Geoscience, April 18, 2008.

Rager, A. H., 2008, Proposed experiments on the effect of rapid decompression on the fragmentation of basalt with implications for the formation of Martian rampart craters *in* 11th Mars Craters Consortium, October 2008, Flagstaff, Arizona, U.S.A.

Rager, A., Hanley, T.R., Calvin, C., Balint, T., Santiago, D., Anderson, J., Cassidy, T., Chavez-Clemente, D., Corbett, B.M., Hammerstein, H., Letcher, A., McGowan, E.M., McMenamin, D.S., Murphy, N., Obland, M.D., Parker, J.S., Perron, T., Petro, N., Pulupa, M., Schofield, R., and Sizemore, H.G., 2006, Endurance: The rewards and challenges of landing a spacecraft on Europa, 4th International Planetary Probe Workshop, Pasadena, California.

Calvin, C., **Rager, A**., Balint, T., Santiago, D., Anderson, J., Cassidy, T., Chavez-Clemente, D., Corbett, B., Hanley, T., Letcher, A., McGowan, E., McMenamin, D., Murphy, N., Obland, M., Parker, J., Perron, T., Petro, N., Pulupa, M., Schofield, R., and Sizemore, H., 2005, Endurance: The rewards and challenges of landing a spacecraft on Europa, *in* Eos Trans. AGU,, San Francisco, CA, p. Abstract P11B-0113.

Mehaffey, M. H., Nash, M. S., Wade, T. G., Ebert, D. W., Jones, K. B., and **Rager, A**., 2005, Linking Land Cover and Water Quality in New York City's Water Supply Watersheds: Environmental Monitoring and Assessment, v. 107, p. 29-44.

Drushke, P., Honn, D., McKelvey, M., Nastanski, N., **Rager, A**., Smith, E. I., and Belliveau, R., 2004, Volcanology of the Northern Eldorado Mountains, Nevada: New evidence for the source of the Tuff of Bridge Spring?, *in* Geologic Society of America, Denver, CO.

Rager, A. H., 2003, Thin section analysis of temper in Patayan ceramics from Willow Beach, Arizona [M.S. thesis]: Emporia, KS, Emporia State University, 87 p.

Mehaffey, M. H., Nash, M. S., Wade, T. G., Edmonds, C. M., Ebert, D. W., Jones, K. B., and **Rager, A**., 2002, A landscape assessment of the Catskill/Delaware Watersheds 1975-1998: New York City's Water Supply Watersheds: U.S. Environmental Protection Agency, EPA/600/R-01/075.

Rager, A. H., Rager, H. B., and Seymour, G. R., 2002, Using Remote Sensing and GIS to identify potential clay sources for Topoc Buff Ware, Willow Beach, Arizona, *in* Geologic Society of America, Denver, CO.

Rager, A. H., Tinney, L., and Bice, L., 2001, Some considerations for operational remote sensing programs, *in* Above and Beyond 2001: EPA Remote Sensing Conference, Las Vegas, NV.

Pitchford, A. M., **Rager, A. H**., and Van Remortel, R., 2000, Using NEXRAD precipitation data in GIS for environmental modeling, *in* ESRI User's Conference, San Diego, CA.

Rager, A. H., 2000, Geologic and Natural Resources Applications in Remote Sensing, *in* Nevada Geologic Society, Southern Nevada Chapter Meeting, Las Vegas, NV.

Rautenstrauch, K. R**., Rager, A. L. H**., and Rakestraw, D., 1998, Winter Behavior of Desert Tortoises in Southcentral, Nevada: Journal of Wildlife Management, v. 62, no. 1, p. 98-104.

Dissertation Title:

The Interaction of Rock and Water during Shock Decompression:
A Hybrid Model for Fluidized Ejecta Formation

Dissertation Examination Committee:

Chairperson, Eugene Smith, Ph.D.
Committee Member, Elisabeth Hausrath, Ph.D.
Committee Member, Rosaly Lopes, Ph.D.
Committee Member, Adam Simon, Ph.D.
Graduate Faculty Representative, Stephen Lepp, Ph.D.